

國立交通大學
光電工程研究所
博士論文

微波光電與光電封裝於
多功能光擷取網路的研究

Enabling Technologies of Microwave Photonics
and Optoelectronics Package in Optical
Multi-Service Access Network

The logo of Tsinghua University is a circular seal. It features a blue outer ring with the university's name in Chinese and English. The center contains a stylized building and the year '1896'.

研究生：林俊廷

指導教授：祁 甦 教授

邱碧秀 教授

中華民國 九十六 年 六 月

微波光電與光電封裝於多功能光擷取網路的研究

Enabling Technologies of Microwave Photonics
and Optoelectronics Package in Optical
Multi-Service Access Network

研 究 生：林俊廷
指 導 教 授：祁 蛙
邱碧秀

Student: Chun-Ting Lin
Advisor: Sien Chi
Bi-Shiou Chiou



國立交通大學 電機學院
光電工程研究所
博士論文

A Dissertation
Submitted in Partial Fulfillment of the Requirements
for the Degree of Doctor of Philosophy in
Department of Photonics and
Institute of Electro-Optical Engineering
College of Electrical Engineering and Computer Science
National Chiao-Tung University
Hsinchu, Taiwan, R.O.C.

中華民國九十六年六月

Acknowledgments

(誌 謝)

歲月匆匆，博士生涯一晃眼就要結束了，回想起當初憑藉著一股對光通訊充滿興趣的傻勁，放棄工作選擇念光電博士班，我很慶幸當初的選擇是對的，因為在學校的四年中是人生收穫最多的一個階段。

首先，非常感謝祁姓老師的諄諄教誨與提供良好的研究環境，祁老師對研究、實驗與學問理論所表現出來的熱忱與執著，深深的影響學生的求學態度，以及祁老師嚴謹認真的研究態度、條理分明的思考模式及廣博的知識的帶領下，令學生受益匪淺，研究期間不甚順遂時，祁老師時時給予鼓勵與建議，方能讓學生之研究順利進行。再來要感謝邱碧秀老師在學生論文上給予的建議與指導，還有陳智弘老師的帶領，在每次的研究討論過程中總能給我很好的解答與新的思考方向，也非常感謝彭松村老師、李清庭老師、劉容生老師、許根玉老師、賴映杰老師撥空擔任口試委員，提出許多寶貴的建議。

其次要感謝交通大學卓越發展計畫實驗室，逢源科技股份有限公司，及台耀科技股份有限公司提供優良的研究設備，讓實驗得以順利的進行，感謝彭朋群博士不吝分享所學，讓我快速進入狀況，還有實驗室的成員們嘉建、煒仁、晟峰、盛鵬、鐘响、明芳、南光等，在實驗中提供了寶貴的意見與熱心的幫助，感謝你們和我一起努力。這段時光將是我人生中美好的一段回憶，也祝福他們順利畢業。

最後，我要感謝我親愛的父母、姊姊還有我的女友，謝謝你們無怨無悔的付出與全心全力的支持，你們的愛是我的重要支柱，使我能順利的完成研究與博士生涯。此論文得以完成，再次衷心感謝大家。

微波光電與光電封裝 於多功能光擷取網路的研究

研 究 生：林俊廷

指導教授：祁 姓
邱碧秀

國立交通大學 電機學院
光電工程研究所



本論文的主旨在微波光學與光電封裝於能同時提供影像、聲音、及訊號的多功能光擷取網路之研究。在微波光學於光擷取網路的應用研究部分，我們理論分析 Mach-Zehnder 光調變器非線性對微波訊號失真的影響，以及分析因製造誤差產生非理想 Mach-Zehnder 光調變器造成微波訊號的損害，並求出最佳化 Mach-Zehnder 光調變器的調變條件，利用此理論結果應用在多功能光擷取網路中，提出同時傳輸及產生微波與基頻訊號的微波光電系統，與整合無線通訊及有線通訊的多功能光擷取網路系統。在光電封裝於光擷取網路的應用研究部分，我們研究粉末冶金在光訊號傳輸與接收模組之封裝技術，粉末冶金的雷射焊接缺陷機制、焊後位移、追縱誤差、及可靠度測試將於此研究一併討論。這些應用的原理與架構已詳盡的分析與實驗驗證，上述的成果預期將有助於多功能光擷取網路的發展。

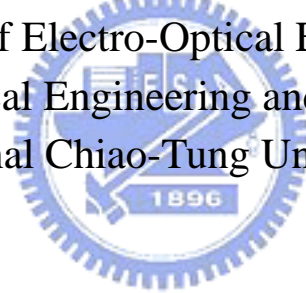
Enabling Technologies of Microwave Photonics and Optoelectronics Package in Optical Multi-Service Access Network

Student: Chun-Ting Lin

Advisor: Sien Chi

Bi-Shiou Chiou

Department of Photonics and
Institute of Electro-Optical Engineering
College of Electrical Engineering and Computer Science
National Chiao-Tung University



ABSTRACT

This dissertation investigates the applications of microwave photonics and optoelectronics package in last-mile multi-service access networks offering video, voice, and data to customers simultaneously. For the content about microwave photonics applications, the impact of both the Mach-Zehnder modulator (MZM) nonlinearity and the imperfect MZM with finite extinction ratios on millimeter-wave signals (mm-wave) will be theoretically analyzed and experimentally investigated. Optimal conditions for RF signal generations using imperfect MZMs based on double-sideband with optical carrier suppression (DSBCS) modulation are also discussed. Based on the optimal

condition, the optical-wireless network offering both wireless and wired-line access approaches and the hybrid access network integrating radio over fiber (RoF) and fiber-to-the-home (FTTH) systems are proposed and investigated. For the content related to applications of optoelectronics packages for bidirectional or triple-directional FTTH systems providing triple-play services, power metallurgy (PM) is proposed as a cost-effective method of fabricating metal parts for optoelectronic modules. The weldability of PM stainless steel is investigated, including welding defect mechanism, post-welding-shift, tracking error, and reliability test. These investigations and demonstrations will be useful in the future optical multi-service access networks.



Contents

Acknowledgements	I
Chinese Abstract	II
English Abstract	III
Contents	V
List of Figures	VIII
List of Tables	XIII
List of Acronyms	XIV

Chapter 1

Introduction

1.1 Last-Mile Optical Access Network	1
1.2 Motivation of Radio over Fiber Systems	2
1.2.1 The Impact of MZM Nonlinearity on RF Signals	2
1.2.1 Optical Convergence Access Network	3
1.3 Motivation of Optoelectronics Package for Bidirectional FTTH Systems ...	4
1.4 Organization of the Dissertation	5
References	6

Chapter 2

Theoretical Analysis of Millimeter-Wave Generation Using Double Sideband with Carrier Suppression

2.1 Mm-Wave Generation Using Perfect MZM	10
2.2 Mm-Wave Generation Using Imperfect MZM with Imperfect Power Splitting Ratio	15
2.3 Carrier-to-Distortion Ratio of MM-Wave Signal Using Perfect and	

Imperfect MZMs	21
References	25

Chapter 3

Optical Convergence Access Network Providing Wired-line and Wireless Signals

3.1 Dual-Service Optical-Wireless Access Network	37
3.1.1 Experimental Setup	38
3.1.2 Experimental Results and Discussion	39
3.2 Hybrid Optical Access Network	41
3.2.1 Hybrid Optical Access Network Architecture	42
3.2.2 Experimental Setup	42
3.2.3 Experimental Results and Discussion	44
References	46



Chapter 4

Cost-Effective Optoelectronics Package Using Powder Metallurgy for FTTH Systems

4.1 Introduction to Powder Metallurgy	65
4.1.1 Shaping Method	65
4.1.2 Material Selection	66
4.2 Laser Welding System and Experimental Setup	68
4.2.1 Laser Welding System	68
4.2.2 Laser Package Construction	69
4.3 Laser Weldability	70
4.3.1 Microstructures of DCP and MIM Steel	70
4.3.2 Defect Formation of Laser Welding Spots in MIM SS316L and DCP SS316L	71
4.3.3 Defect Formation of MIM SS316L and DCP SS316L	

Jointed with SS304	73
4.3.4 Selection of Optimum Welding Conditions	74
4.3.5 Post-Welding-Shift	75
4.3.6 Tracking Error	77
4.4 Reliability Test	79
References	80

Chapter 5

Conclusions

5.1 Summary for the Dissertation	103
5.1.1 Theoretically Analysis of Mm-wave Generation Using DSBCS modulation	103
5.1.2 Dual-Service Optical-Wireless Access Network	104
5.1.3 Hybrid Access Network Integrating RoF and FTTH Systems	105
5.1.4 Optoelectronics Package Using Powder Metallurgy for Triple-Directional FTTH Systems	106

List of Figures

- Fig.2.1** The principle diagram of the optical mm-wave generation using perfect MZM based on DSBCS modulation.
- Fig.2.2** Illustration of the optical spectrum at the output of the perfect MZM.
- Fig.2.3** Illustration of the electrical spectrum of mm-wave signals using perfect MZM after square-law PD detection.
- Fig.2.4** The principle diagram of the optical mm-wave generation using imperfect MZM based on DSBCS modulation.
- Fig.2.5** Illustration of the optical spectrum at the output of the imperfect MZM.
- Fig.2.6** Illustration of the electrical spectrum of generated mm-wave signals using imperfect MZM after square-law PD detection. (A) BTB mm-wave signals. (b) Mm-wave signals after transmission over dispersion fiber.
- Fig.2.7** Amplitude of the Bessel function varied with MI.
- Fig.2.8** E_{AM} and E_{PM} varied with r_1 .
- Fig.2.9** MZM ER varied with r_1 .
- Fig.2.10** OSNDR of the optical mm-wave signals varied with MI. A: Analytic stimulation, N: Numeric stimulation.
- Fig.2.11** Optimal MI for maximum OSNDR of the optical mm-wave signals. The solid spot indicates the optimal MI for each MZM ER. The range of optimal MI comes from 1-dB tolerance of the maximum OSNDR.
- Fig.2.12** Desired electrical mm-wave signals varied with MI after PD

detection.

Fig.2.13 Optimal MI for the electrical mm-wave signal generation. The solid spot indicates the optimal MI for each MZM ER. The range of optimal MI comes from 1-dB tolerance of the maximum power of the electrical mm-wave signal.

Fig.3.1 Experimental setup for the generation and transmission of optical RF and BB signals based on DSBCS modulation scheme using one MZM.

Fig.3.2 BER curves (a) and power penalties at BER of 10^{-9} (b) of DC signals for different MI-RF.

Fig.3.3 BER curves (a) and power penalties at BER of 10^{-9} (b) of BB signals for different MI-RF.

Fig.3.4 Duty cycles of optical microwaves based on DSBCS modulation. The optical microwave power is 1dBm. The optical power scale is 0.8 mW/div and the time scale is 20 ps/div. The MI-RF is set at (a) 1 (b) 0.66 (c) 0.43 (d) 0.28 (e) 0.18.

Fig.3.5 The OCSR of optical microwaves based on DSBCS modulation. The resolution is 0.01nm. The MI-RF is set at (a) 1 (b) 0.66 (c) 0.43 (d) 0.28 (e) 0.18

Fig.3.6 BER curves (a) and power penalties at BER of 10^{-9} (b) using one DD-MZM with MI-RF of 0.43 after transmission over 25 km, 50 km and 75 km SSMF.

Fig.3.7 BER curves (a) and power penalties at BER of 10^{-9} (b) using one SD-MZM with MI-RF of 0.43 after transmitted over 25 km, 50 km, and 75 km SSMF.

- Fig.3.8** Fiber nonlinearity impairment of the receiver sensitivity. The MI-RF for SD-MZM is 0.43. The optical power scale is 0.8 mW/div and the time scale is 20 ps/div. (i)10 dBm, BTB (ii)10 dBm, 25 km (iii)10 dBm, 50 km (iv)10 dBm, 75 km (v)10 dBm, 100 km
- Fig.3.9** Schematic diagram of the hybrid optical access network.
- Fig.3.10** Experimental setup for RF and BB signal generation and transmission using one external integrated modulator.
- Fig.3.11** BER curves (a) and power penalties at BER of 10^{-9} (b) of RF signals using DSBCS modulation for MI-RF from 0.6 to 0.1.
- Fig.3.12** BER curves (a) and power penalties at BER of 10^{-9} (b) of RF signals using DSB modulation for MI-RF from 1 to 0.16.
- Fig.3.13** Eye diagrams of RF signals using DSB modulation for MI-RF from 1 to 0.16. (a) MI-RF=1 (b) MI-RF=0.8 (c) MI-RF=0.65 (d) MI-RF=0.52 (e) MI-RF=0.42 (f) MI-RF=0.25 (g) MI-RF=0.16. (Power scale: 270 μ W/div, Time scale: 20ps/div)
- Fig.3.14** BER curves of BB and RF signals for MI-BB from 1 to 0.18. MI-RF is fixed at 0.48.
- Fig.3.15** Experimental setup to study the interference between BB and RF Signals.
- Fig.3.16** BER curves (a) and power penalties at BER of 10^{-9} (b) of the RF signals using DSBCS modulation with optimal MI-RF and varied MI-BB.
- Fig.3.17** BER curves (a) and power penalties at BER of 10^{-9} (b) of both BB

and RF signals using DSBCS modulation following transmission over 25 km and 50 km SSMF. The optimal MI-RF and MI-BB for driving MZ-a and MZ-b are 0.48 and 0.27, respectively.

Fig.4.1 (a) Illustration of bidirectional optoelectronic package. (b) Illustration of triple-directional optoelectronic package. (c) The components of bidirectional optoelectronic package.

Fig.4.2 (a),(b) Schematic diagram of the laser welding system. (c) Configuration of the cylindrical-type laser module. Arrows indicate the welding spots.

Fig.4.3 Microstructures of MIM 316L, DCP SS316L, and MIM Invar. (a) MIM SS316L with 97% of full density (b) MIM Invar with 96% of full density (c) DCP SS316L with 85% of full density

Fig.4.4 Cross sections of the welding spots in the MIM SS316L with various welding conditions. Data in parentheses are pulse duration (millisecond), power (kilowatt), and laser energy (joule).

Fig.4.5 Cross sections of the welding spots with two pulses of laser in the MIM SS316L. Data in parentheses are pulse duration (millisecond), power (kilowatt), and laser energy (joule).

Fig.4.6 Cross sections of the welding spots in the DCP SS316L with various welding conditions. Data in parentheses are pulse duration (millisecond), power (kilowatt), and laser energy (joule).

Fig.4.7 Penetration depth of welding spots as a function of laser power with various pulse durations T. (a) MIM SS316L (b) Full density SS316L, MIM SS316, and DCP SS316L

Fig.4.8 Welding joints of MIM SS316L (bottom) and SS304L (top). Data

in parentheses are pulse duration (millisecond), power (kilowatt), and laser energy (joule).

Fig.4.9 Welding joints of DCP SS316L (bottom) and SS304L (top). Data in the bracket () are pulse duration (ms), power (kW), and laser energy (J).

Fig.4.10 Schematic joint geometries for laser welding (a) Lap-fillet joint, (b) Lap joint, and (c) Fillet joint. Arrow indicates the welding spot.

Fig.4.11 Strengths of 316L/304L, MIM316L/304L, and MIMInvar/304L joints as a function of laser power with various pulse durations T.

Fig.4.12 Coupling power as a function of x , y , and z orientations.

Fig.4.13 Distribution of the coupling power loss due to PWS.

Fig.4.14 Optical power deviation after mechanical shock test. The laser modules are subject to 5 shock pulses for each of orientations x , y , and z . The peak acceleration of the pulse is 1500g and pulse duration is 0.5ms. The pass/fail criterion is 0.5dB maximum change in optical coupling power. (a) MIM SS316L. (b) MIM Invar

Fig.4.15 Optical power deviation after vibration test. The frequency ranges from 20 to 2000Hz and return to 20Hz, and the cycle time is not less than 4min. This cycle is performed 4 times for each of orientations x , y , and z . The pass/fail criterion is 0.5dB maximum change in optical coupling power. (a) MIM SS316L. (b) MIM Invar.

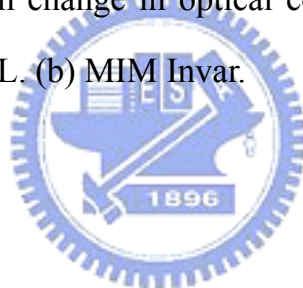
Fig.4.16 Optical power deviation with numbers of temperature cycling test. The temperature changes from -40°C to 85°C . The ramp rate is

more than 10 °C/min and the dwell time is 10 min at 85°C and -40°C. The cycle time is within 40min. The pass/fail criterion is 0.5dB maximum change in optical coupling power after 500 cycles.

(a) MIM SS316L. (b) MIM Invar

Fig.4.17 Optical power deviation with time of high temperature storage test. The laser modules are tested at 85°C. The pass/fail criterion is 0.5dB maximum change in optical coupling power after 2000hrs. (a) MIM SS316L. (b) MIM Invar

Fig.4.18 Optical power deviation with time of low temperature storage test. The laser modules are tested at -40°C. The pass/fail criterion is 0.5dB maximum change in optical coupling power after 2000hrs. (a) MIM SS316L. (b) MIM Invar.



List of Tables

Table I Joint strengths (kg) of lap joint, fillet joint, and lap-fillet joint with various welding parameters. The deviation of joint strength is less than 10%.

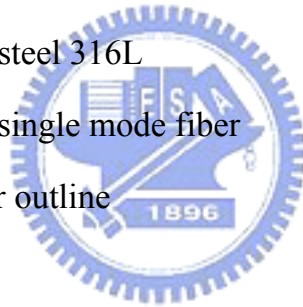
Table II Tracking error (dB) of the laser modules with MIM SS316L material as the laser housing

Table III Tracking error (dB) of the laser modules with MIM Invar material as the laser housing

List of Acronyms

BTB	Back-to-back
BB	Baseband
BER	Bit-error-ratio
CCD	Charge-coupled device
CTE	Coefficient of thermal expansion
CW	Continuous wave
DCP	Die compaction
DSB	Double-sideband
DSBCS	Double-sideband with optical carrier suppression
DC	Down-converted
DD-MZM	Dual-electrode MZM
EDFA	Erbium-doped fiber amplifier
ER	Extinction ratio
FTTH	Fiber-to-the-home
V_{π}	Half-wave voltage
MZM	Mach-Zehnder modulator
MIM	Metal injection molding
Mm-wave	millimeter-wave
MI	Modulation index
OCSR	Optical carrier suppression ratio
OMI	Optical modulation index
V_{p-p}	Peak-to-peak voltage
PD	Photodiode

PWS	Post-welding-shift
PM	Powder metallurgy
PRBS	Pseudo random bit sequence
MIM	Metal injection molding
RF	Radio frequency
RoF	Radio over fiber
MI-BB	BB modulation index
MI-RF	RF modulation index
SD-MZM	Single-electrode MZM
SSB	Single-sideband
SS304L	Stainless steel 304L
SS316L	Stainless steel 316L
SSMF	Standard single mode fiber
TO	Transistor outline



Chapter 1

Introduction

1.1 Last-Mile Optical Access Network

Over the past decade, the core optical network has been widely investigated, leaving the last-mile access as the bottleneck in the provision of high bandwidth services to the end users. However, recently, the demand for broadband access to the customer's home has been driven by applications such as fast internet access, video on demand, online video game, time shifted broadcast, etc. Therefore, the last-mile access network providing broadband services has attracted a lot of attention in recent years. However, the drawback of the conventional access networks using twisted-pair copper cable is the limited bandwidth-distance product. To overcome this issue, optical fiber has been demonstrated to be the best choice as the transmission media in the future access network [1-3].

The choice technology of the optical access networks depends heavily on geographical consideration, population densities, and economic factors. Hence, the last-mile optical access networks include wired-line and wireless approaches. Radio over fiber (RoF) and fiber-to-the-home (FTTH) systems are promising candidates in wireless and wired-line access networks [1-2], respectively. FTTH systems can provide the ultimate high bandwidth services

and highly reliable connection, and RoF systems can provide mobility and point-to-multi-points access technology. However, the key factor of these two systems is economic issue. Low-cost last-mile access networks can accelerate the initial deployment of optical broadband communication to the end users.

1.2 Motivation of Radio over Fiber Systems

1.2.1 The Impact of MZM Nonlinearity on RF Signals

The key of the RoF systems is to reduce the cost of base stations and to centralize the shared optical and millimeter-wave (mm-wave) components in the central stations [4]. The optical mm-wave generation and transport are key techniques in RoF wireless access systems. The optical mm-waves using external Mach-Zehnder modulator (MZM) based on double-sideband (DSB), single-sideband (SSB), and double-sideband with optical carrier suppression (DSBCS) modulation schemes have been demonstrated [5-7]. Generated by setting the bias voltage of MZM at the quadrature point, the DSB signal experiences performance fading problems due to fiber dispersion, resulting in degradation of the receiver sensitivity. The SSB signal is generated when a phase difference of $\pi/2$ is applied between the two electrodes of the dual-electrode MZM (DD-MZM) biased at the quadrature point. Although the SSB modulation can reduce the impairment of fiber dispersion, it suffers worse receiver sensitivity than DSB modulation [7]. In [6], the DSBCS modulation signal is demonstrated at the mm-wave range with the best receiver sensitivity, the lowest spectral occupancy, the lowest bandwidth requirement for RF signal, electrical amplifier, and optical modulator, and the smallest power penalty of

receiver sensitivity after long transmitted distance. In the conventional DSBCS modulation scheme, the baseband (BB) signal is generated using a single-electrode MZM (SD-MZM) biased at the quadrature point and then up-converted using a DD-MZM biased at the minimum transmission point [6]. In order to get high optical carrier suppression ratio (OCSR), the electrical radio frequency (RF) signal with full swing ($2V_{\pi}$) for MZM is necessary so that DD-MZM is needed to generate the mm-wave. However, the MZM is biased at the nonlinear region and the MZM nonlinearity will affect the performance of mm-wave signals. Despite numerous studies on mm-wave signal generation using DSBCS modulation, no information is available to investigate the MZM nonlinearity effect on the performance of mm-wave signals.

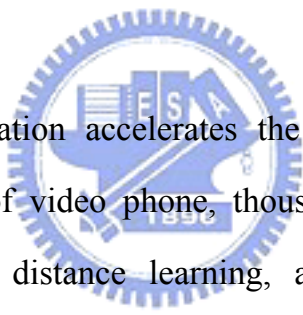


1.2.2 Optical Convergence Access Network

Recently, the convergence of the broadband wired-line and wireless access network has attracted a lot of attention. This hybrid network can provide the stable broadband services and mobility to the end users. In addition, the high cost of separated wireless and wired-line access networks necessitates integration of the two distributed networks into a single shared infrastructure. Of priority concern is to transmit both RF and BB signals on a single wavelength over a single fiber in a cost effective way with acceptable performance. Recently, the simultaneous modulation and transmission of a RF signal and a BB signal has been demonstrated [5-6][8-9]. However, [8-9] the generated hybrid BB and RF signals suffer from performance fading problem caused by fiber dispersion. Therefore, a dispersion-shifting fiber is employed to transmit the hybrid signals. This negative effect limits implementation to green

field application only, rather than the most common application with already installed standard single mode fiber (SSMF). Furthermore, [5-6] only one signal is modulated on the optical subcarrier such that the BB and RF signals are identical after square-law photodiode (PD) detection. Hence, a simple and cost-effective modulation and transmission of the independent BB and RF signals without periodical performance fading due to fiber dispersion are required.

1.3 Motivation of Optoelectronics Package for Bidirectional FTTH Systems



Broadband communication accelerates the demand of FTTH systems taking us into the future of video phone, thousands of television channels, movies on demand, long distance learning, and 3D on-line game. The successful introduction of low-cost optoelectronic module is the key to FTTH systems, and the primary contribution of the cost arises from packaging the laser. Submicronmeter-accuracy alignments and strong joints for laser packages are essential to achieve high coupling efficiency and long-term stability. The laser welding technique is the best candidate to satisfy such criteria and offers lots of advantages, such as good long-term stability, high joint strength to welding size ratio, high volume and high speed production, submicronmeter-accuracy fixing, no contact process, and good repeatability [10]-[15].

The laser packaging bodies are typically categorized into two styles: box-type and cylindrical-type [10]. The box-type and cylindrical-type

optoelectronic packages dominate high performance lightwave communication systems and low-cost markets, respectively. The box-type package allows more space for a thermoelectric cooler and multiple components to achieve high speed, high power output, high reliability, and operation at constant temperature. The cylindrical-type package based on transistor outline (TO)-Can is used where the fabrication cost is important and the performance requirement is not so high. Recently, FTTH systems provide triple-play services delivering video, voice, and data to consumers on one fiber where 1310nm transmission is in one direction and 1490 and/or 1550 nm are in the other [1][10]. These bidirectional and triple-directional data transmissions of FTTH systems require the transformation of cylindrical-type packages into box-type packages because more room is needed to accommodate more WDM filters and lenses. This transformation results in an increased number and cost of metal parts, which is contradictory to the low-cost market. In addition, machining accuracy of metal parts is very critical to the yield of the laser welding process. Although the conventional machining method of fabricating metal parts can make metal parts with box shape and accurate dimension, the cost is still too high. Although numerous studies on improving the performance of the box-type optoelectronic packages have been conducted recently [16-20], only limited information is available on how to design and fabricate high-yield, high-performance, and low-cost bidirectional or triple-directional optoelectronics packages.

1.4 Organization of the Dissertation

This dissertation consists of three related parts. In Chapter 2, the impact of the MZM nonlinearity and the imperfect MZM on the optical mm-wave signal performance will be theoretically analyzed. Optimum conditions for the mm-wave generation using DSBCS modulation based on imperfect MZMs will be theoretically discussed. In chapter 3, the optical-wireless network offering both broadband wireless and wired services and the hybrid access network integrating RoF and FTTH systems will be proposed and investigated. In addition, the impact of the MZM nonlinearity on the mm-wave signal using DSBCS modulation will be experimentally studied.

In chapter 4, powder metallurgy (PM) is proposed as a cost-effective method of fabricating metal parts for optoelectronic modules in bidirectional or triple-directional FTTH systems. The weldability of PM stainless steel is investigated, including the welding defect mechanisms, optimum welding parameter, post-welding-shift (PWS), and tracking error. Moreover, the reliability data are also presented. Finally, a brief summary and conclusions will be given in Chapter 5.

References

- [1] C. H. Lee, W. V. Sorin, and B. Y. Kim, "Fiber to the Home Using a PON Infrastructure," *J. Lightwave Technol.*, vol. 24, no. 12, pp. 4568-4583, Dec. 2006.
- [2] A. J. Seeds, and K. J. Williams, "Microwave Photonics," *J. Lightwave Technol.*, vol. 24, no. 12, pp. 4428-4641, Dec. 2006.
- [3] R. E. Wagner, J. R. Igel, R. Whitman, M. D. Vaughn, A. B. Ruffin, and S. Bickham, "Fiber-Based Broadband-Access Deployment in the United

- States,” *J. Lightwave Technol.*, vol. 24, no. 12, pp. 4526-4540, Dec. 2006.
- [4] Ken-Ichi Kitayama, “Architectural Considerations of Fiber-Radio Millimeter-Wave Wireless Access Systems”, *Fiber and Integrated Optics*, 19:167-186, 2000.
- [5] A. Martinez, V. Polo, and J. Marti, “Simultaneous baseband and RF optical modulation scheme for feeding wireless and wireline heterogeneous access network,” *IEEE Trans. Microwave theory and Technol.*, vol. 49, pp. 2018-2024, 2001.
- [6] J. Yu, Z. Jia, L. Yi, G. K. Chang, and T. Wang, “Optical millimeter-wave generation or up-conversion using external modulator,” *IEEE Photon. Technol. Lett.*, vol. 18, pp. 265-267, 2006.
- [7] C. Lim, C. Lin, M. Attygalle, A. Nirmalathas, D. Novak, and R. Waterhouse, “Analysis of Optical Carrier-to-Sideband Ratio for Improving Transmission Performance in Fiber-Radio Links,” *IEEE J. Lightwave Technol.*, vol. 54, no. 5, pp. 2181-2187, 2006.
- [8] T. Kamisaka, T. Kuri, K. Kitayama, “Simultaneous modulation and fiber-optic transmission of 10Gb/s baseband and 60GHz band radio signals on a single wavelength,” *IEEE Trans. Microwave theory and Technol.*, vol. 49, pp. 2013-2017, 2001.
- [9] K. Ikeda, T. Kuri, and K. Kitayama, “Simultaneous three band modulation and fiber-optic transmission of 2.5Gb/s baseband, microwave-, and 60GHz band signals on a single wavelength,” *IEEE J. Lightwave Technol.*, vol. 21, pp. 3194-3202, 2003.
- [10] D. S. Alles, “Trends in laser packaging,” in *Proc. 40th Electron. Comp. Technol. Conf.*, pp. 185–192, 1990.
- [11] M. R. Matthews, B. M. Macdonald, and K. R. Preston, “Optical

- components-the new challenge in packaging,” *IEEE Trans. Comp., Hybrids, Manufac t. Technol.*, vol. 13, no. 4, pp. 798–806, Dec. 1990.
- [12] Aaron A. Hollander and Keith J. Watkins, “The Art and Science of Optoelectronic Joining,” *Photonics Spectra*, pp. 110-114, Oct. 1993.
- [13] B. Valk, R. Battig, and O. Anthamatren, “Laser Welding for Fiber Pigtailling with Long-term Stability and Submicron Accuracy,” *Opt. Eng.*, vol. 34, no. 9, pp. 2675–2682, 1995.
- [14] M. K. Song, S. G. Kang, N. Hwang, H. T. Lee, S. S. Park, and K. E. Pyun, “Laser Weldability Analysis of High-speed Optical Transmission Device Packaging,” *IEEE Tran. Comp., Packag., Manufact. Technol. A*, vol. 19, no. 4, pp. 758-763, Nov. 1996.
- [15] W. H. Cheng, W. H. Wang, and J. C. Chen, “Defect Formation Mechanisms in Laser Welding Techniques for Semiconductor Laser Packaging,” *IEEE Tran. Comp., Hybrids, Manufact. Technol. B*, vol. 20, no. 4, pp. 396-402, Nov. 1997.
- [16] Y. C. Hsu, Y. C. Tsai, Y. L. Ho, M. T. Sheen, J. H. Kuang, and W. H. Cheng, “A Novel Alignment Shift Measurement and Correction Technique in Laser-Welded Laser Module Packaging,” *J. Lightwave Technol.*, vol. 23, no. 2, pp. 486-494, Feb. 2005.
- [17] W. H. Cheng, M. T. Sheen, C. M. Cheng, and Y. T. Tseng, “An Optimum Approach for Reduction of Fiber Alignment Shift of Fiber-Solder-Ferrule Joints in Laser Module Packaging,” *J. Lightwave Technol.*, vol. 22, no. 2, pp. 589-594, Feb. 2004.
- [18] W. S. Chang and S. J. Na, “Thermomechanical Analyses of Laser Precision Joint for Optoelectronic Components,” *J. Trans. Adv. Packag.*, vol. 26, no. 2, pp. 349-358, Jun. 2003.

- [19] Y. Lin, W. Liu, and F. G. Shi, "Laser Welding Induced Alignment Distortion in Butterfly Laser Module Packages: Effect of Welding Sequence," *J. Trans. Adv. Packag.*, vol. 25, no. 1, pp. 73-78, Feb. 2002.
- [20] J. H. Kuang, M. T. Sheen, S. C. Wang, G. L. Wang, and W. H. Cheng, "Post-Weld-Shift in Dual-in-Line Laser Package," *J. Trans. Adv. Packag.*, vol. 24, no. 1, pp. 81-85, Feb. 2001.



Chapter 2

Theoretical Analysis of Millimeter-Wave Generation Using Double Sideband with Carrier Suppression

Since the MZM based on DSBCS modulation scheme is biased at the minimum transmission and operated at the nonlinear region, the MZM nonlinearity have a great influence on the performance of the mm-wave signal [1-2]. In addition, for a real MZM, a perfect 50/50 splitting ratio of the Y-splitter cannot be achieved, due to fabrication tolerances. Therefore, imperfect MZMs will have a finite extinction ratio (ER) and the mm-wave signals using DSBCS modulation will have finite OCSR. This will result in degrading the mm-wave signals. In this section, the impact of both the MZM nonlinearity and the imperfect MZM on the mm-wave signal performance will be theoretically analyzed. Optimum conditions for the mm-wave generation using DSBCS modulation will be discussed.

2.1 Mm-Wave Generation Using Perfect MZM

The principle diagram of the optical mm-wave generation using DSBCS modulation scheme is illustrated in Fig. 2.1. For the perfect MZM, the power splitting ratio of two arms of the MZM is 0.5. The electrical field at the output of the single-arm MZM can be expressed as

$$E_{out}(t) = E_0 \cos \left[\frac{\Phi[V(t)]}{2} \right] \cos(\omega_c t) \quad (1)$$

where E_0 and ω_c are the electric amplitude and angular frequency of the input optical carrier, $V(t)$ is the applied driving voltage, and $\Phi[V(t)]$ is the optical carrier phase difference induced by $V(t)$ between the two arms of the MZM. $V(t)$ consisting of an electrical sinusoidal signal and a dc biased voltage can be written as

$$V(t) = V_{bias} + V_m \cos(\omega_{RF} t) \quad (2)$$

where V_{bias} is the dc biased voltage, V_m and ω_{RF} are the amplitude and the angular frequency of the electrical driving signal, respectively. The optical carrier phase difference induced by $V(t)$ can be expressed as

$$\Phi[V(t)] = \pi \left[\frac{V_{bias}}{V_\pi} + \frac{V_m}{V_\pi} \cos(\omega_{RF} t) \right] \quad (3)$$

where V_π is the half-wave voltage of the MZM. Therefore, the output electrical field can be rewritten as

$$\begin{aligned} E_{out}(t) &= E_0 \cos \left(\frac{\pi}{2} \left[\frac{V_{bias}}{V_\pi} + \frac{V_m}{V_\pi} \cos(\omega_{RF} t) \right] \right) \cos(\omega_c t) \\ &\stackrel{\text{def}}{=} E_0 \cos([b + m \cos(\omega_{RF} t)]) \cos(\omega_c t) \\ &= E_0 \{ \cos b \cdot \cos[m \cos(\omega_{RF} t)] \\ &\quad - \sin b \cdot \sin[m \cos(\omega_{RF} t)] \} \cos(\omega_c t) \end{aligned} \quad (4)$$

where $b \stackrel{\text{def}}{=} \frac{V_{bias}}{2V_\pi} \pi$ is a constant phase shift determined by the dc biased voltage, and $m \stackrel{\text{def}}{=} \frac{V_m}{2V_\pi} \pi$ is the phase modulation index. Expanding (4) with

Bessel function leads to an expression for the electrical field as

$$\begin{aligned}
E_{out}(t) &= E_0 \cos \mathfrak{b} \left\{ J_0(\mathfrak{m}) + 2 \sum_{n=\text{even}}^{\infty} i^n J_n(\mathfrak{m}) \cos(n\omega_{RF}t) \right\} \cos(\omega_c t) \\
&\quad - E_0 \sin \mathfrak{b} \left\{ 2 \sum_{n=\text{odd}}^{\infty} i^{n-1} J_n(\mathfrak{m}) \cos(n\omega_{RF}t) \right\} \cos(\omega_c t) \quad (5) \\
&= E_0 \cos \mathfrak{b} \left\{ J_0(\mathfrak{m}) \cos(\omega_c t) \right. \\
&\quad \left. + \sum_{n=1}^{\infty} [J_{2n}(\mathfrak{m}) \cos(\omega_c t + 2n\omega_{RF}t - n\pi) \right. \\
&\quad \left. + J_{2n}(\mathfrak{m}) \cos(\omega_c t - 2n\omega_{RF}t + n\pi)] \right\} \\
&\quad + E_0 \sin \mathfrak{b} \left\{ \sum_{n=1}^{\infty} [J_{2n-1}(\mathfrak{m}) \cos(\omega_c t + (2n-1)\omega_{RF}t - n\pi) \right. \\
&\quad \left. + J_{2n-1}(\mathfrak{m}) \cos(\omega_c t - (2n-1)\omega_{RF}t + n\pi)] \right\} \quad (6)
\end{aligned}$$

where J_n is the Bessel function of the first kind of order n , and i is equal to $\sqrt{-1}$. For DSBCS modulation, the bias voltage is set at $V_{bias} = V_{\pi}$, and we have $\cos \mathfrak{b} = 0$ and $\sin \mathfrak{b} = 1$. Hence, the electrical field of the mm-wave signal using DSBCS modulation can be written as

$$\begin{aligned}
E_{out}(t) &= E_0 \cdot \sum_{n=1}^{\infty} \{ J_{2n-1}(\mathfrak{m}) \cos[\omega_c t + (2n-1)\omega_{RF}t - n\pi] \\
&\quad + J_{2n-1}(\mathfrak{m}) \cos[\omega_c t - (2n-1)\omega_{RF}t + n\pi] \} \quad (7)
\end{aligned}$$

All the even-order sidebands associated with the term $\sin \mathfrak{b}$ are eliminated, and only the odd-order sidebands associated with the term $\cos \mathfrak{b}$ are kept, as shown in Fig. 2.2. The amplitudes of the generated optical sidebands are proportional to those of the Bessel function associated with the phase

modulation index m . With the amplitude of the electrical driving signal V_m equal to V_π , the maximum m is $\frac{\pi}{2}$. As m ranges from 0 to $\frac{\pi}{2}$, the Bessel function J_{2n-1} for $n \geq 1$ decreases and increases with the order of Bessel function and m , respectively. $J_1\left(\frac{\pi}{2}\right)$, $J_3\left(\frac{\pi}{2}\right)$, $J_5\left(\frac{\pi}{2}\right)$, and $J_7\left(\frac{\pi}{2}\right)$ are 0.5668, 0.0690, 0.0022, and 0.00003581, respectively. Therefore, the optical sidebands with the Bessel function higher than $J_5(m)$ can be ignored, and (7) can be further simplified to

$$\begin{aligned} E_{out}(t) = E_0 \{ & -J_1(m) \cos[(\omega_c + \omega_{RF})t] - J_1(m) \cos[(\omega_c - \omega_{RF})t] \\ & + J_3(m) \cos[(\omega_c + 3\omega_{RF})t] + J_3(m) \cos[(\omega_c - 3\omega_{RF})t] \\ & - J_5(m) \cos[(\omega_c + 5\omega_{RF})t] - J_5(m) \cos[(\omega_c - 5\omega_{RF})t] \} \quad (8) \end{aligned}$$

When optical DSBCS signals are transmitted over a single-mode fiber with dispersion, a phase shift to each optical sideband relative to optical carrier is induced [3]. The propagation constant of the dispersion fiber $\beta(\omega)$ can be expressed as

$$\beta(\omega) = n(\omega) \frac{\omega}{c} = \beta_0 + \beta_1(\omega - \omega_c) + \frac{1}{2}\beta_2(\omega - \omega_c)^2 + \dots \quad (9)$$

where $\beta_m = \frac{d^m \beta}{d\omega^m}$ is the derivative of the propagation constant. The effect of high order fiber dispersion at 1550nm band is neglected. For carrier tones with central frequency at $\omega = \omega_c \pm n\omega_{RF}$, we have

$$\beta(\omega_c \pm n\omega_{RF}) \cong \beta_0 \pm n\beta_1(\omega_c)\omega_{RF} + \frac{1}{2}n^2\beta_2(\omega_c)\omega_{RF}^2 \quad (10)$$

and

$$\beta_2(\omega_c) = -\frac{c}{2\pi f_o^2} D \quad (11)$$

where c is the speed in free space, D is the chromatic dispersion parameter

and f_o is the frequency of the optical carrier. For a standard single-mode fiber, D is 17 ps/(nm.km). Therefore, after transmission over a single-mode fiber of length z , the electrical field can be written as

$$\begin{aligned}
E(t) = E_0 \Big\{ & -J_1(m) \cos \left[(\omega_c + \omega_{RF})t - \beta_0 z - \beta_1 \omega_{RF} z - \frac{1}{2} \beta_2 \omega_{RF}^2 z \right] \\
& - J_1(m) \cos \left[(\omega_c - \omega_{RF})t - \beta_0 z + \beta_1 \omega_{RF} z - \frac{1}{2} \beta_2 \omega_{RF}^2 z \right] \\
& + J_3(m) \cos \left[(\omega_c + 3\omega_{RF})t - \beta_0 z - 3\beta_1 \omega_{RF} z - \frac{9}{2} \beta_2 \omega_{RF}^2 z \right] \\
& + J_3(m) \cos \left[(\omega_c - 3\omega_{RF})t - \beta_0 z + 3\beta_1 \omega_{RF} z - \frac{9}{2} \beta_2 \omega_{RF}^2 z \right] \\
& - J_5(m) \cos \left[(\omega_c + 5\omega_{RF})t - \beta_0 z - 5\beta_1 \omega_{RF} z - \frac{25}{2} \beta_2 \omega_{RF}^2 z \right] \\
& - J_5(m) \cos \left[(\omega_c - 5\omega_{RF})t - \beta_0 z + 5\beta_1 \omega_{RF} z - \frac{25}{2} \beta_2 \omega_{RF}^2 z \right] \Big\} \quad (12)
\end{aligned}$$

After square-law detection using an ideal PD with responsivity R , the photocurrent can be expressed as

$$I(t) = R \cdot |E(t)|^2 \quad (13)$$

The individual square term of (12) in (13) will generate the baseband signal, and the cross terms of (12) in (13) will generate the desired mm-wave signal and its harmonics distortion signals. These desired mm-wave terms are

$$\begin{aligned}
i_{2\omega_{RF}} = R \cdot E_o^2 [& J_1^2(m) - 2J_1(m)J_3(m) \cos(4\beta_2 \omega_{RF}^2 z) \\
& - 2J_3(m)J_5(m) \cos(8\beta_2 \omega_{RF}^2 z) + \dots] \\
& \cdot \cos(2\omega_{RF} t - 2\beta_1 \omega_{RF} z) \quad (14a)
\end{aligned}$$

$$\begin{aligned}
= R \cdot E_o^2 \Big[& J_1^2(m) - 2 \sum_{n=1}^{\infty} J_{2n-1}(m) J_{2n+1}(m) \cos(4n\beta_2 \omega_{RF}^2 z) \Big] \\
& \cdot \cos(2\omega_{RF} t - 2\beta_1 \omega_{RF} z) \quad (14b)
\end{aligned}$$

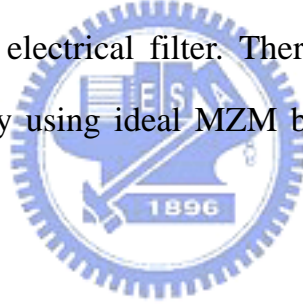
$$\begin{aligned}
i_{4\omega_{RF}} &= R \cdot E_o^2 [-2J_1(m)J_3(m) \cos(4\beta_2\omega_{RF}^2 Z) + 2J_1(m)J_5(m) \cos(12\beta_2\omega_{RF}^2 Z)] \\
&\quad \cdot \cos(4\omega_{RF}t - 4\beta_1\omega_{RF}Z) \tag{15}
\end{aligned}$$

$$\begin{aligned}
i_{6\omega_{RF}} &= R \cdot E_o^2 [J_3^2(m) + 2J_1(m)J_5(m) \cos(12\beta_2\omega_{RF}^2 Z)] \\
&\quad \cdot \cos(6\omega_{RF}t - 6\beta_1\omega_{RF}Z) \tag{16}
\end{aligned}$$

$$i_{8\omega_{RF}} = R \cdot E_o^2 [-2J_3(m)J_5(m) \cos(8\beta_2\omega_{RF}^2 Z)] \cdot \cos(8\omega_{RF}t - 8\beta_1\omega_{RF}Z) \tag{17}$$

$$i_{10\omega_{RF}} = R \cdot E_o^2 \cdot J_5^2(m) \cdot \cos(10\omega_{RF}t - 10\beta_1\omega_{RF}Z) \tag{18}$$

The corresponding electrical spectrum of generated mm-wave signals is shown in Fig. 2.3. The original driving signal (ω_{RF}) and the odd terms of its harmonics distortion signals (ω_{RF} , $3\omega_{RF}$, $5\omega_{RF}$) are not observed, and the even terms of its harmonics distortion signals ($4\omega_{RF}$, $6\omega_{RF}$, $8\omega_{RF}$) can be easily eliminated by using electrical filter. Therefore, the desired mm-wave signal ($2\omega_{RF}$) is attained by using ideal MZM based on DSBCS modulation schemes.



2.2 Mm-Wave Generation Using Imperfect MZM with Imperfect Power Splitting Ratio

For MZM with imperfect power splitting ratio, as shown in Fig.2.4, the electrical field at the output of the MZM can be written as:

$$E_{out}(t) = \Re\{E_o[\sqrt{r_1} \cdot \sqrt{1-r_2} \cdot \exp(j\phi_1) + \sqrt{1-r_1} \cdot \sqrt{r_2} \cdot \exp(j\phi_2)] \cdot \exp(j\omega_c t)\} \tag{19}$$

where r_1 and r_2 are the power splitting ratios of the first and second Y-splitters in MZM, respectively, and ϕ_1 and ϕ_2 are optical carrier phase shifts induced by the applied driving voltages in the upper and lower arms of

MZM, respectively. Therefore, this imperfect structure allows the MZM to have a finite ER. The intrinsic MZM ER due to fabrication tolerances can be expressed as

$$ER = \frac{\sqrt{r_1} \cdot \sqrt{1-r_2} + \sqrt{1-r_1} \cdot \sqrt{r_2}}{\sqrt{r_1} \cdot \sqrt{1-r_2} - \sqrt{1-r_1} \cdot \sqrt{r_2}} \quad (20)$$

If $\sqrt{r_1} \cdot \sqrt{1-r_2} < \sqrt{1-r_1} \cdot \sqrt{r_2}$, we can rewrite the equation (19) as

$$\begin{aligned} E_{out}(t) = & \Re\{E_0 \sqrt{r_1} \cdot \sqrt{1-r_2} \cdot [\exp(j\phi_1) + \exp(j\phi_2)] \cdot \exp(j\omega_c t) \\ & + E_0 [\sqrt{1-r_1} \cdot \sqrt{r_2} - \sqrt{r_1} \cdot \sqrt{1-r_2}] \cdot \exp(j\phi_2) \\ & \cdot \exp(j\omega_c t)\} \end{aligned} \quad (21)$$

Hence, the modulation of the MZM with imperfect power splitting ratios can be viewed as the sum of a perfect MZM modulation and a phase modulator (PM) modulation which are represented in the first and second terms of equation (21), respectively. It is observed that the PM modulation can be eliminated if $r_1 = r_2 = 0.5$, perfect MZMs, or $r_1 = 1 - r_2$. However, due to fabrication tolerances, both conditions cannot be achieved. Thus, the PM modulation caused by the unbalanced power ratios of the impact MZM cannot be avoided. The electrical fields of the MZM and PM modulations can be rewritten as:

$$E_{out_AM}(t) = \Re\left\{E_{AM} \cdot \cos\left(\frac{\phi_1 - \phi_2}{2}\right) \cdot \exp^{j\left(\frac{\phi_1 + \phi_2}{2}\right)} \exp(j\omega_c t)\right\} \quad (22)$$

and

$$E_{out_PM}(t) = \Re\{E_{PM} \cdot \exp(j\phi_2) \cdot \exp(j\omega_c t)\} \quad (23)$$

where E_{AM} and E_{PM} are $2E_0\sqrt{r_1} \cdot \sqrt{1-r_2}$ and $E_0(\sqrt{1-r_1} \cdot \sqrt{r_2} - \sqrt{r_1} \cdot \sqrt{1-r_2})$, respectively. Under the single-arm MZM condition, we have

$\phi_1 = -\phi_2 = -\frac{\theta}{2}$, and $\frac{\theta}{2}$ can be expressed as

$$\frac{\theta}{2} = \frac{V_{bias}}{2V_\pi} \pi + \frac{V_m \cos(\omega_{RF} t)}{2V_\pi} \pi \stackrel{\text{def}}{=} b + m \cos(\omega_{RF} t) \quad (24)$$

where b and m are $\frac{V_{bias}}{2V_\pi} \pi$ and $\frac{V_m}{2V_\pi} \pi$, respectively. The output electrical field of the amplitude modulation can be rewritten as:

$$\begin{aligned} E_{out_AM}(t) &= E_{AM} \cdot \cos\left(\frac{\theta}{2}\right) \cdot \cos(\omega_c t) \\ &= E_{AM} \cdot \cos([b + m \cos(\omega_{RF} t)]) \cos(\omega_c t) \\ &= E_{AM} \{ \cos b \cdot \cos[m \cos(\omega_{RF} t)] \\ &\quad - \sin b \cdot \sin[m \cos(\omega_{RF} t)] \} \cos(\omega_c t) \\ &= E_{AM} \left\{ \cos b \cdot \left[J_0(m) + 2 \sum_{n=\text{even}}^{\infty} i^n J_n(m) \cos(n \omega_{RF} t) \right] \right. \\ &\quad \left. - \sin b \left[2 \sum_{n=\text{odd}}^{\infty} i^{n-1} J_n(m) \cos(n \omega_{RF} t) \right] \right\} \cos(\omega_c t) \\ &= E_{AM} \left\{ \cos b \left[J_0(m) \cdot \cos(\omega_c t) \right. \right. \\ &\quad \left. \left. + \sum_{n=1}^{\infty} [J_{2n}(m) \cos(\omega_c t + 2n \omega_{RF} t - n\pi) \right. \right. \\ &\quad \left. \left. + J_{2n}(m) \cos(\omega_c t - 2n \omega_{RF} t + n\pi)] \right] \right. \\ &\quad \left. + \sin b \left[\sum_{n=1}^{\infty} [J_{2n-1}(m) \cos(\omega_c t + (2n-1) \omega_{RF} t - n\pi) \right. \right. \\ &\quad \left. \left. + J_{2n-1}(m) \cos(\omega_c t - (2n-1) \omega_{RF} t + n\pi)] \right] \right\} \quad (25) \end{aligned}$$

For the phase modulation, the output electrical field can be written as:

$$\begin{aligned}
E_{out_PM}(t) &= \Re \left\{ E_{PM} \cdot \exp \left(j \frac{\theta}{2} \right) \cdot \exp(j\omega_c t) \right\} \\
&= E_{PM} \cdot \Re \{ \exp j[\omega_c t + b + m \cos(\omega_{RF} t)] \} \\
&= E_{PM} \cdot \Re \{ e^{j(\omega_c t + b)} \cdot e^{j m \cos(\omega_{RF} t)} \} \\
&= E_{PM} \cdot \Re \left\{ e^{j(\omega_c t + b)} \cdot e^{j m \cdot \sin(\omega_{RF} t + \frac{\pi}{2})} \right\} \\
&= E_{PM} \cdot \Re \left\{ e^{j(\omega_c t + b)} \cdot \sum_{n=-\infty}^{\infty} J_n(m) \cdot e^{j n (\omega_{RF} t + \frac{\pi}{2})} \right\} \\
&= E_{PM} \cdot \Re \left\{ \sum_{n=-\infty}^{\infty} J_n(m) \cdot e^{j \{ (\omega_c t + b) + n (\omega_{RF} t + \frac{\pi}{2}) \}} \right\} \\
&= E_{PM} \cdot \sum_{n=-\infty}^{\infty} J_n(m) \cdot \cos \left\{ (\omega_c + n\omega_{RF})t + \left(b + \frac{n\pi}{2} \right) \right\} \tag{26}
\end{aligned}$$

For mm-wave signals based on DSBCS modulation with the bias voltage set at $V_{bias} = V_{\pi}$, we have $b = \frac{\pi}{2}$, $\cos b = 0$, and $\sin b = 1$. The output electrical field of the amplitude and phase modulations can be rewritten as

$$\begin{aligned}
E_{out_AM}(t) &= E_{AM} \sum_{n=1}^{\infty} \{ J_{2n-1}(m) \cos[\omega_c t + (2n-1)\omega_{RF} t - n\pi] \\
&\quad + J_{2n-1}(m) \cos[\omega_c t - (2n-1)\omega_{RF} t + n\pi] \} \tag{27}
\end{aligned}$$

and

$$E_{out_PM}(t) = E_{PM} \cdot \sum_{n=-\infty}^{\infty} J_n(m) \cdot \cos \left[(\omega_c + n\omega_{RF})t + \left(\frac{n+1}{2} \right) \pi \right] \tag{28}$$

It is reasonable that optical sidebands with the Bessel functions with the order higher than 5 can be ignored, and the electrical field at the output of the MZM with imperfect power splitting ratios can be simplified to

$$\begin{aligned}
E_{out}(t) &= E_{out_AM}(t) + E_{out_PM}(t) \\
&= -E_{PM}J_0(m) \sin(\omega_c t) \\
&\quad - (E_{AM} + E_{PM})J_1(m) \cos(\omega_c t + \omega_{RF} t) \\
&\quad - (E_{AM} + E_{PM})J_1(m) \cos(\omega_c t - \omega_{RF} t) \\
&\quad + E_{PM}J_2(m) \sin(\omega_c t + 2\omega_{RF} t) + E_{PM}J_2(m) \sin(\omega_c t - 2\omega_{RF} t) \\
&\quad + (E_{AM} + E_{PM})J_3(m) \cos(\omega_c t + 3\omega_{RF} t) \\
&\quad + (E_{AM} + E_{PM})J_3(m) \cos(\omega_c t - 3\omega_{RF} t) \\
&\quad - E_{PM}J_4(m) \sin(\omega_c t + 4\omega_{RF} t) - E_{PM}J_4(m) \sin(\omega_c t - 4\omega_{RF} t) \\
&\quad - (E_{AM} + E_{PM})J_5(m) \cos(\omega_c t + 5\omega_{RF} t) \\
&\quad - (E_{AM} + E_{PM})J_5(m) \cos(\omega_c t - 5\omega_{RF} t) \tag{29}
\end{aligned}$$

Figure 2.5 shows the optical spectrum of the mm-wave signals. The PM modulation due to imperfect MZMs not only affects the desired sideband $(\omega_c t \pm \omega_{RF} t)$ and odd-order sidebands $(\omega_c t \pm 3\omega_{RF} t, \omega_c t \pm 5\omega_{RF} t)$ but also attributes to the carrier $(\omega_c t)$ and even-order sidebands $(\omega_c t \pm 2\omega_{RF} t, \omega_c t \pm 4\omega_{RF} t)$. After transmission over dispersive fiber with $\beta(\omega_c \pm n\omega_{RF}) \cong \beta_0 \pm n\beta_1(\omega_c)\omega_{RF} + \frac{1}{2}n^2\beta_2(\omega_c)\omega_{RF}^2$, the electric field can be written as

$$\begin{aligned}
E(t) &= -E_{PM}J_0(m) \sin(\omega_c t) \\
&\quad - (E_{AM} + E_{PM})J_1(m) \cos(\omega_c t + \omega_{RF} t - \beta_0 z - \beta_1 \omega_{RF} z - 1/2 \beta_2 \omega_{RF}^2 z) \\
&\quad - (E_{AM} + E_{PM})J_1(m) \cos(\omega_c t - \omega_{RF} t - \beta_0 z + \beta_1 \omega_{RF} z - 1/2 \beta_2 \omega_{RF}^2 z) \\
&\quad + E_{PM}J_2(m) \sin(\omega_c t + 2\omega_{RF} t - \beta_0 z - 2\beta_1 \omega_{RF} z - 2\beta_2 \omega_{RF}^2 z) \\
&\quad + E_{PM}J_2(m) \sin(\omega_c t - 2\omega_{RF} t - \beta_0 z + 2\beta_1 \omega_{RF} z - 2\beta_2 \omega_{RF}^2 z) \\
&\quad + (E_{AM} + E_{PM})J_3(m) \cos(\omega_c t + 3\omega_{RF} t - \beta_0 z - 3\beta_1 \omega_{RF} z - 9/2 \beta_2 \omega_{RF}^2 z) \\
&\quad + (E_{AM} + E_{PM})J_3(m) \cos(\omega_c t - 3\omega_{RF} t - \beta_0 z + 3\beta_1 \omega_{RF} z - 9/2 \beta_2 \omega_{RF}^2 z) \\
&\quad - E_{PM}J_4(m) \sin(\omega_c t + 4\omega_{RF} t - \beta_0 z - 4\beta_1 \omega_{RF} z - 8\beta_2 \omega_{RF}^2 z) \\
&\quad - E_{PM}J_4(m) \sin(\omega_c t - 4\omega_{RF} t - \beta_0 z + 4\beta_1 \omega_{RF} z - 8\beta_2 \omega_{RF}^2 z) \\
&\quad - (E_{AM} + E_{PM})J_5(m) \cos(\omega_c t + 5\omega_{RF} t - \beta_0 z - 5\beta_1 \omega_{RF} z - 25/2 \beta_2 \omega_{RF}^2 z) \\
&\quad - (E_{AM} + E_{PM})J_5(m) \cos(\omega_c t - 5\omega_{RF} t - \beta_0 z + 5\beta_1 \omega_{RF} z - 25/2 \beta_2 \omega_{RF}^2 z) \tag{30}
\end{aligned}$$

After square-law detection using an ideal PD with responsivity R , the

photocurrents of the desired mm-wave signal and its harmonics distortion signals can be expressed as

$$\begin{aligned}
 i_{\omega_{RF}} = R \cdot E_o^2 \Big\{ & 2(E_{AM}E_{PM} + E_{PM}^2) \Big[J_0(m)J_1(m) \sin\left(\frac{1}{2}\beta_2\omega_{RF}^2Z\right) \\
 & + J_1(m)J_2(m) \sin\left(\frac{3}{2}\beta_2\omega_{RF}^2Z\right) \\
 & + J_2(m)J_3(m) \sin\left(\frac{5}{2}\beta_2\omega_{RF}^2Z\right) \\
 & + J_3(m)J_4(m) \sin\left(\frac{7}{2}\beta_2\omega_{RF}^2Z\right) + J_4(m)J_5(m) \sin\left(\frac{9}{2}\beta_2\omega_{RF}^2Z\right) \Big] \Big\} \\
 & \cdot \cos(\omega_{RF}t - \beta_1\omega_{RF}Z) \quad (31)
 \end{aligned}$$

$$\begin{aligned}
 i_{2\omega_{RF}} = R \cdot E_o^2 \Big\{ & (E_{AM} + E_{PM})^2 J_1^2(m) \\
 & - 2E_{PM}^2 [J_0(m)J_2(m) \cos(2\beta_2\omega_{RF}^2Z) \\
 & + J_2(m)J_4(m) \cos(6\beta_2\omega_{RF}^2Z)] \\
 & - 2(E_{AM} + E_{PM})^2 [J_1(m)J_3(m) \cos(4\beta_2\omega_{RF}^2Z) \\
 & + J_3(m)J_5(m) \cos(8\beta_2\omega_{RF}^2Z)] \Big\} \cdot \cos(2\omega_{RF}t - 2\beta_1\omega_{RF}Z) \quad (32)
 \end{aligned}$$

$$\begin{aligned}
 i_{3\omega_{RF}} = R \cdot E_o^2 \Big\{ & 2(E_{AM}E_{PM} + E_{PM}^2) \Big[-J_0(m)J_3(m) \sin\left(\frac{9}{2}\beta_2\omega_{RF}^2Z\right) \\
 & - J_1(m)J_4(m) \sin\left(\frac{15}{2}\beta_2\omega_{RF}^2Z\right) \\
 & - J_2(m)J_5(m) \sin\left(\frac{21}{2}\beta_2\omega_{RF}^2Z\right) + J_1(m)J_2(m) \sin\left(\frac{3}{2}\beta_2\omega_{RF}^2Z\right) \Big] \Big\} \\
 & \cdot \cos(3\omega_{RF}t - 3\beta_1\omega_{RF}Z) \quad (33)
 \end{aligned}$$

$$\begin{aligned}
 i_{4\omega_{RF}} = R \cdot E_o^2 \Big\{ & 2E_{PM}^2 J_0(m)J_4(m) \cos(8\beta_2\omega_{RF}^2Z) \\
 & + 2(E_{AM} + E_{PM})^2 [J_1(m)J_5(m) \cos(12\beta_2\omega_{RF}^2Z) \\
 & - J_1(m)J_3(m) \cos(4\beta_2\omega_{RF}^2Z)] + E_{PM}^2 J_2(m)J_2(m) \Big\} \\
 & \cdot \cos(4\omega_{RF}t - 4\beta_1\omega_{RF}Z) \quad (34)
 \end{aligned}$$

$$\begin{aligned}
 i_{5\omega_{RF}} = R \cdot E_o^2 \Big\{ & 2(E_{AM}E_{PM} + E_{PM}^2) \Big[J_0(m)J_5(m) \sin\left(\frac{25}{2}\beta_2\omega_{RF}^2Z\right) \\
 & - J_1(m)J_4(m) \sin\left(\frac{15}{2}\beta_2\omega_{RF}^2Z\right) + J_2(m)J_3(m) \sin\left(\frac{5}{2}\beta_2\omega_{RF}^2Z\right) \Big] \Big\} \\
 & \cdot \cos(5\omega_{RF}t - 5\beta_1\omega_{RF}Z) \quad (35)
 \end{aligned}$$

$$\begin{aligned}
i_{6\omega_{RF}} = & R \cdot E_o^2 \{ 2(E_{AM} + E_{PM})^2 J_1(m) J_5(m) \cos(12\beta_2 \omega_{RF}^2 Z) \\
& - 2E_{PM}^2 J_2(m) J_4(m) \cos(6\beta_2 \omega_{RF}^2 Z) \\
& + (E_{AM} + E_{PM})^2 J_3(m) J_3(m) \} \cdot \cos(6\omega_{RF} t - 6\beta_1 \omega_{RF} Z) \quad (36)
\end{aligned}$$

$$\begin{aligned}
i_{7\omega_{RF}} = & R \cdot E_o^2 \left\{ 2(E_{AM} E_{PM} + E_{PM}^2) \left[-J_2(m) J_5(m) \sin\left(\frac{21}{2} \beta_2 \omega_{RF}^2 Z\right) \right. \right. \\
& \left. \left. + J_3(m) J_4(m) \sin\left(\frac{7}{2} \beta_2 \omega_{RF}^2 Z\right) \right] \right\} \cdot \cos(7\omega_{RF} t - 7\beta_1 \omega_{RF} Z) \quad (37)
\end{aligned}$$

$$\begin{aligned}
i_{8\omega_{RF}} = & R \cdot E_o^2 \{ E_{PM}^2 J_4(m) J_4(m) \\
& - 2(E_{AM} + E_{PM})^2 J_3(m) J_5(m) \cos(8\beta_2 \omega_{RF}^2 Z) \} \\
& \cdot \cos(8\omega_{RF} t - 8\beta_1 \omega_{RF} Z) \quad (38)
\end{aligned}$$

$$\begin{aligned}
i_{9\omega_{RF}} = & R \cdot E_o^2 \left\{ 2(E_{AM} E_{PM} + E_{PM}^2) J_4(m) J_5(m) \sin\left(\frac{9}{2} \beta_2 \omega_{RF}^2 Z\right) \right\} \\
& \cdot \cos(9\omega_{RF} t - 9\beta_1 \omega_{RF} Z) \quad (39)
\end{aligned}$$

$$\begin{aligned}
i_{10\omega_{RF}} = & R \cdot E_o^2 \{ (E_{AM} + E_{PM})^2 J_5(m) J_5(m) \} \\
& \cdot \cos(10\omega_{RF} t - 10\beta_1 \omega_{RF} Z) \quad (40)
\end{aligned}$$

The phase modulation, caused by imperfect MZMs, not only contributes to the desired mm-wave signals and even-term distortion signals but also generates odd-term distortion signals. For the back-to-back (BTB) mm-wave signals, only the even-term signals are observed as shown in Fig. 2.6a. However, after transmission over dispersive fiber, the odd-term signals are also observed as shown in Fig. 2.6b. Although the undesired electrical distortion signals can be easily removed by electrical filter, the optical even-order sidebands, caused by phase modulation due to imperfect MZMs, can affect the desired electrical mm-wave signal ($i_{2\omega_{RF}}$).

2.3 Carrier-to-Distortion Ratio of MM-Wave Signal Using Perfect and Imperfect MZMs

A RoF lightwave system mainly consists of transmitters, fiber link, and receivers. The system performance is determined by the performance of those active and passive components. Due to the inherent nonlinearity of MZM, the optical undesired sidebands of the mm-wave signals based on DSBCS modulation scheme cannot be avoided even if perfect MZMs are utilized, as shown in Figs. 2.2 and 2.5. These undesired optical sidebands can degrade the performance of the desired electrical mm-wave signals, and the amplitudes of optical sidebands are related to the corresponding order of the Bessel function, E_{AM} , and E_{PM} . The Bessel function is related to the electrical modulation index ($MI = \frac{V_m}{V_\pi} = \frac{2}{\pi}m$) for driving MZM as shown in Fig. 2.7. As MI decreases from 1 to 0, the 0th-order Bessel function increases and the Bessel function with the order of more than 1 decrease. Thus, the MZM nonlinearity can be reduced by decreasing MI but the OCSR of optical mm-wave signals will increase. The reductions of the MZM nonlinearity and OCSR can improve and degrade the performance of the optical mm-wave signals, respectively.

E_{AM} and E_{PM} are determined by r_1 and r_2 . For simplicity, we assume an ideal second Y-splitter ($r_2 = 0.5$). Figure 2.8 shows E_{AM} and E_{PM} varied with r_1 . As r_1 decreases from 0.5 to 0, E_{AM} and E_{PM} will decrease and increases, respectively. Hence, the phase modulations play more and more important roles in optical mm-wave generations using imperfect MZMs as r_1 decreases. This will degrade the performance of optical mm-wave signals. In addition, r_1 and r_2 determine the MZM ER as shown in Fig. 2.9. The MZM ER decreases when r_1 ranges from 0.5 to 1. For a commercial MZM, the ER of more than 25dB, corresponding to $r_1=0.444$, is available.

The optimal operating condition for RoF systems constrained by nonlinearity is a balance between signal distortion and noise [4] as the MI for driving MZM decreases. However, for mm-wave signals using DSBCS modulation, the OCSR needs to be considered. The main noise sources of the optical link are relative intensity noise (RIN), thermal noise (TN), and shot noise (SN). The OSDR depends on the inherent nonlinearity of the MZM. Increasing the modulation index (MI) can provide more signal power to overcome noise issue, but it also increases the signal distortion. In addition, for the mm-wave signals using MZMs based on DSBCS modulation, decreasing the MI will contribute to less OCSR, resulting in degrading the performance of RoF systems. Hence, optical signal-to-noise ratio (OSNR) and optical signal-to-distortion ratio (OSDR) are used to evaluate the quality of the optical mm-wave signals using imperfect MZMs based on DSBCS modulation. The OSNR and OSDR can be expressed as [4]

$$OSNR = \frac{P_{\omega_c + \omega_{RF}} + P_{\omega_c - \omega_{RF}}}{Noise_{RIN} + Noise_{TN} + Noise_{SN}}$$

$$OSDR = \frac{P_{\omega_c + \omega_{RF}} + P_{\omega_c - \omega_{RF}}}{P_{\omega_c} + P_{\omega_c + 2\omega_{RF}} + P_{\omega_c - 2\omega_{RF}} + P_{\omega_c + 3\omega_{RF}} + P_{\omega_c - 3\omega_{RF}} + P_{\omega_c + 4\omega_{RF}} + P_{\omega_c - 4\omega_{RF}} + P_{\omega_c + 5\omega_{RF}} + P_{\omega_c - 5\omega_{RF}}}$$

$$OSNDR^{-1} = OSNR^{-1} + OSDR^{-1}$$

where P is the power of each optical sideband, and OSNDR is the combination of OSNR and OSDR. Figure 2.10 shows the OSNDR varied with m and different MZM ERs. The commercial software, VPItransmissionMaker 5.0, is used to evaluate the numeric simulation. The RIN, TN, SN, and MZM nonlinearity are considered in the numeric stimulation, and only MZM nonlinearity is considered in the analytic stimulation. Both analytic and numeric stimulations show that the OSNDR increases first and then decreases as the MI for the MZM with ER of more than 15dB decreases from 1 to 0.1.

The maximum OSNDR originates the reduction the MZM nonlinearity and the OCSR which can improve and degrade the OSNDR, respectively.

Furthermore, the MZM ER can affect the maximum OSNDR. As the MZM ER ranges from 35dB to 15dB, the optimal MI for the maximum OSNDR will increase as shown in Fig. 2.11. However, when MZM ER is less than 15dB, the OCSR dominates the OSNDR. Thus, as the MI for the MZM with ER of less than 15dB decreases from 1 to 0.1, the OSNDR will decrease.

Figure 2.12 shows the desired electrical mm-wave signals ($i_{2\omega_{RF}}$) after PD detection. The power of the optical mm-wave signals before PD is normalized to be 0dBm in the numeric stimulation, and RIN, TN, and SN are also included. The results are similar to the OSNDR. When $0 < MI < 1$, the power of desired electrical mm-wave signals increases first and then decreases, and the optimal MI for the maximum $i_{2\omega_{RF}}$ increases as the MZM ER decreases from 35dB to 10dB as shown in Fig. 2.13.

In summary, the MZM nonlinearity and the imperfect MZM with imperfect power splitting ratio have been demonstrated to have a great influence on the performance of the optical RF signals. With decreasing MI for driving imperfect MZMs, the reduction of nonlinearity and OCSR can improve and degrade the mm-wave signal performance, respectively. Hence, there is an optimal MI for the RF signals using DSBCS modulation. In conventional DSBCS modulation scheme, the DD-MZM is utilized to get full MI (MI=1) and high OCSR. According to simulation results, the optimal MI for imperfect MZMs with ER of more than 20dB is less than 0.7, as shown in Fig. 2.13. Therefore, only SD-MZM is needed to realize DSBCS modulation, which is more compact and cost-effective. Moreover, the performance of the mm-wave signals can be improved.

References

- [1] W. H. Chen, and W. I. Way, "Multichannel Single-Sideband SCM/DWDM Transmission System," *J. Lightwave Technol.*, vol. 22, no. 7, pp. 1697-1693, July 2004.
- [2] C. Wu, and X. Zhang, "Impact of Nonlinear Distortion in Radio Over Fiber Systems with Single-Sideband and Tandem Single-Sideband Subcarrier Modulations," *J. Lightwave Technol.*, vol. 24, no. 5, pp. 2076-2090, May 2006.
- [3] L. Cheng, S. Aditya, Z. Li, and A. Nirmalathas, "Generalized Analysis of Subcarrier Multiplexing in Dispersive Fiber-Optic Links Using Mach-Zehnder External Modulator," *J. Lightwave Technol.*, vol. 24, no. 6, pp. 2296-2304, June 2006.
- [4] T. E. Darcie, "Subcarrier Multiplexing for Lightwave Networks and Video Distribution," *IEEE J. on Selected Area in Communication*, vol. 8, no.7, pp. 1240-1248, 1990.

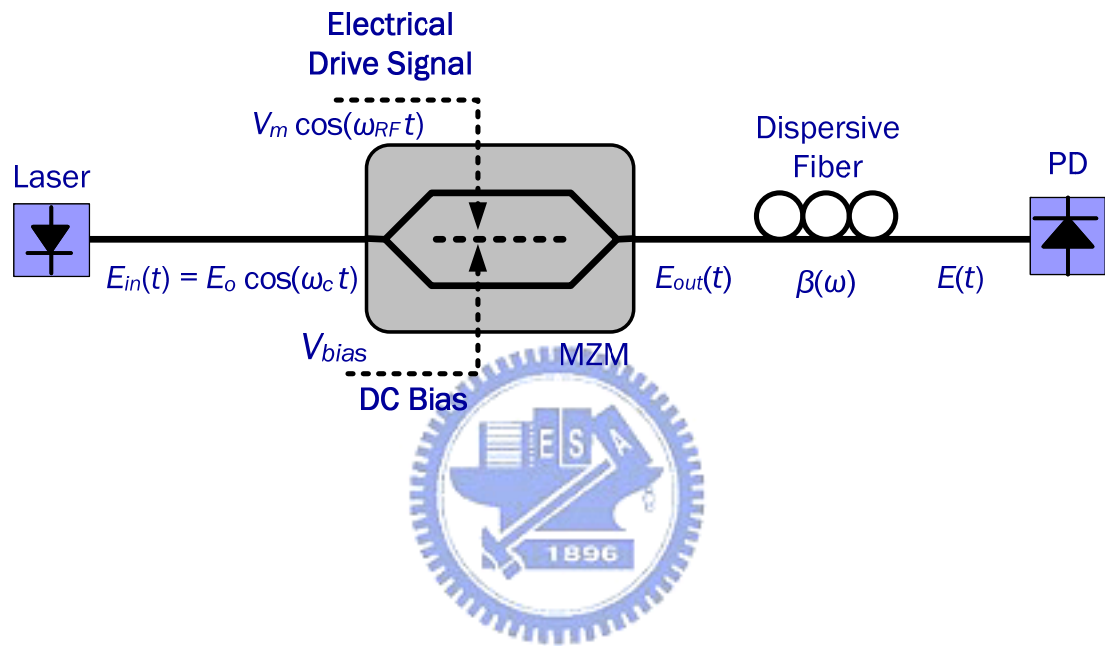


Fig. 2.1 The principle diagram of the optical mm-wave generation using perfect MZM based on DSBCS modulation.

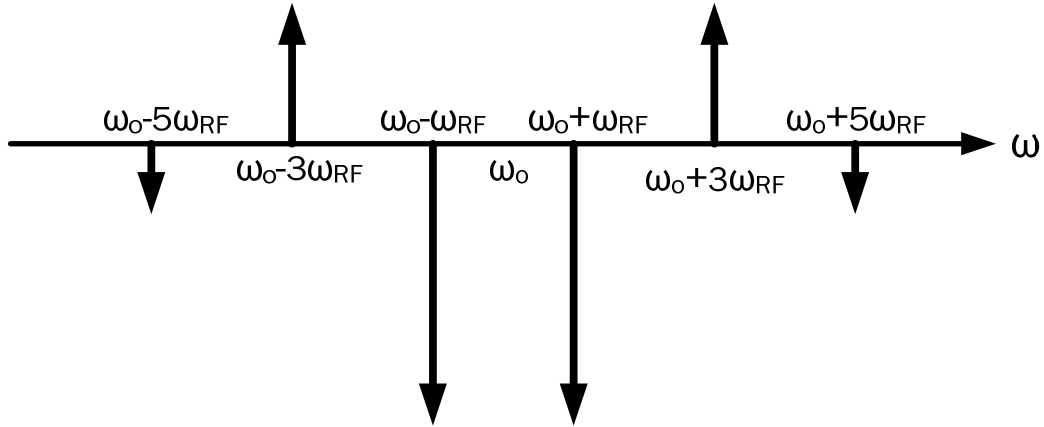


Fig. 2.2 Illustration of the optical spectrum at the output of the perfect MZM.

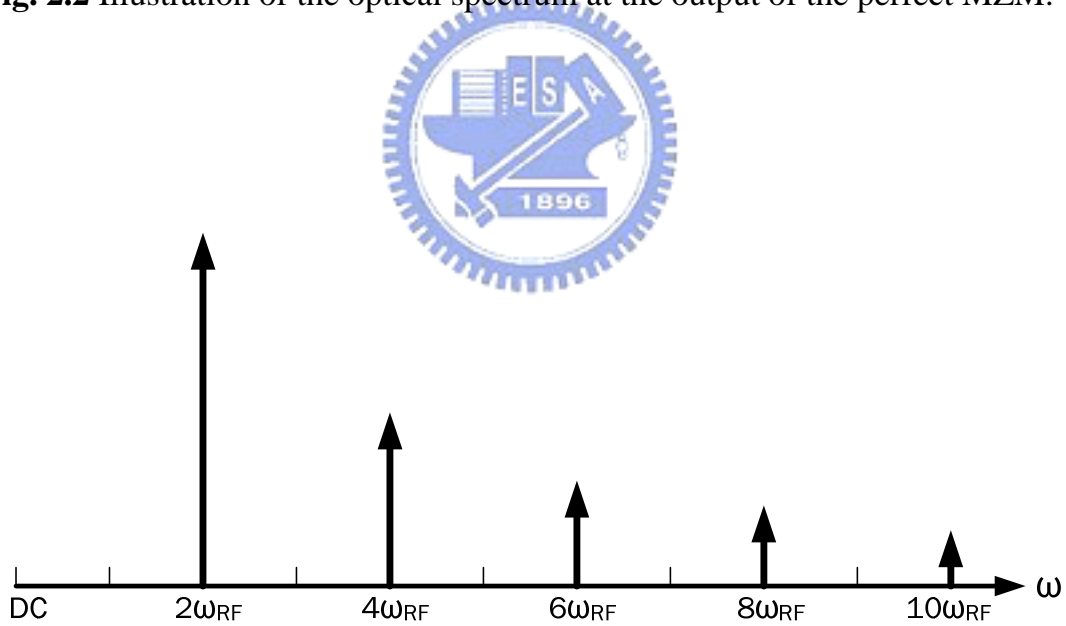


Fig. 2.3 Illustration of the electrical spectrum of mm-wave signals using perfect MZM after square-law PD detection.

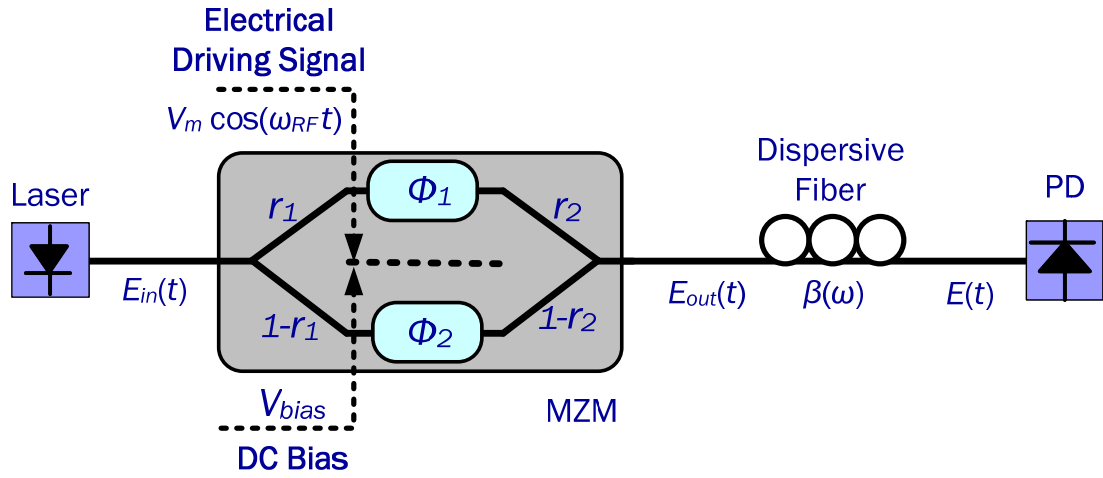


Fig. 2.4 The principle diagram of the optical mm-wave generation using imperfect MZM based on DSBCS modulation.

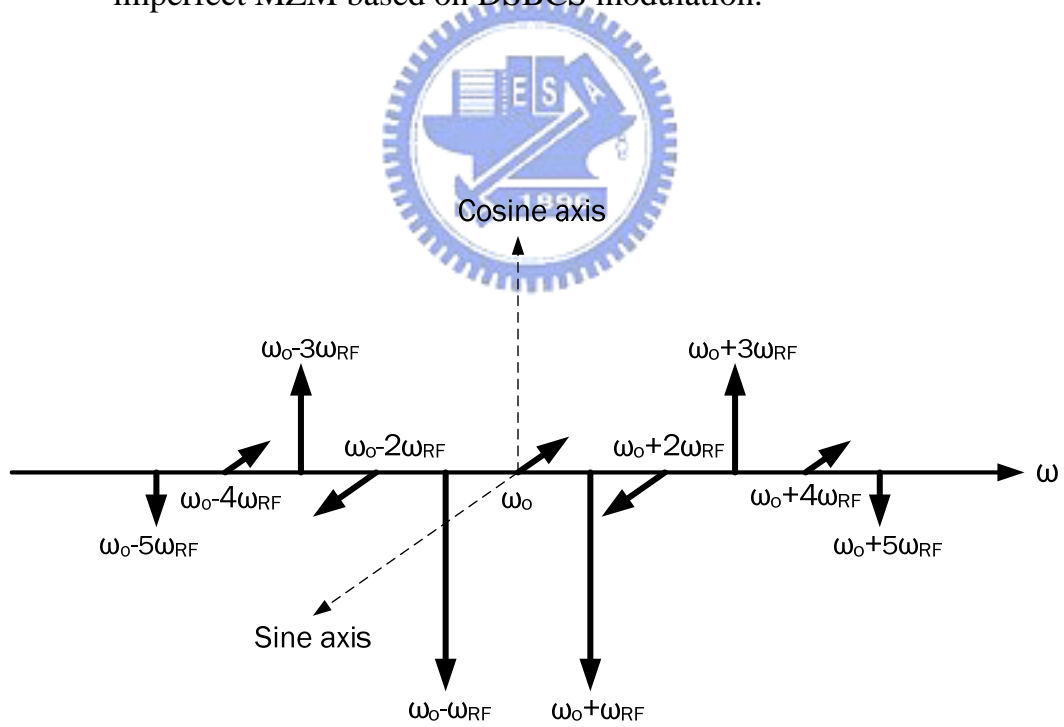
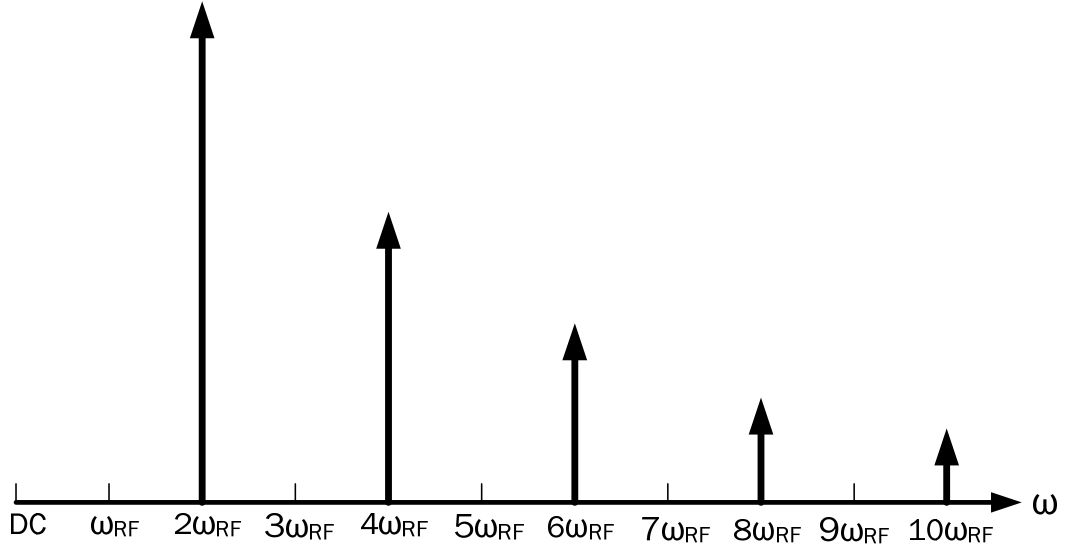
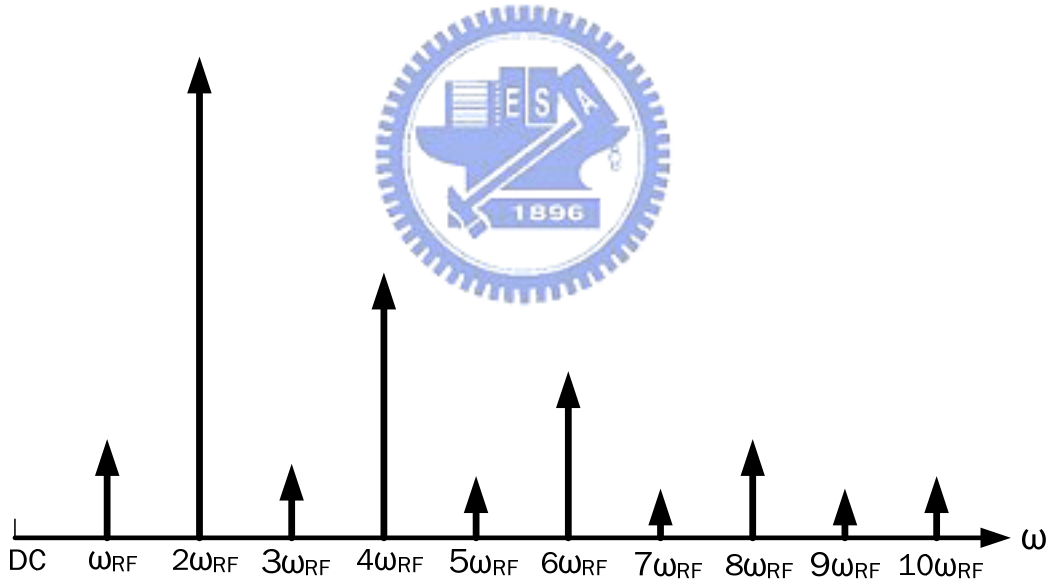


Fig. 2.5 Illustration of the optical spectrum at the output of the imperfect MZM.



(a)



(b)

Fig. 2.6 Illustration of the electrical spectrum of generated mm-wave signals using imperfect MZM after square-law PD detection. (A) BTB mm-wave signals. (b) Mm-wave signals after transmission over dispersion fiber.

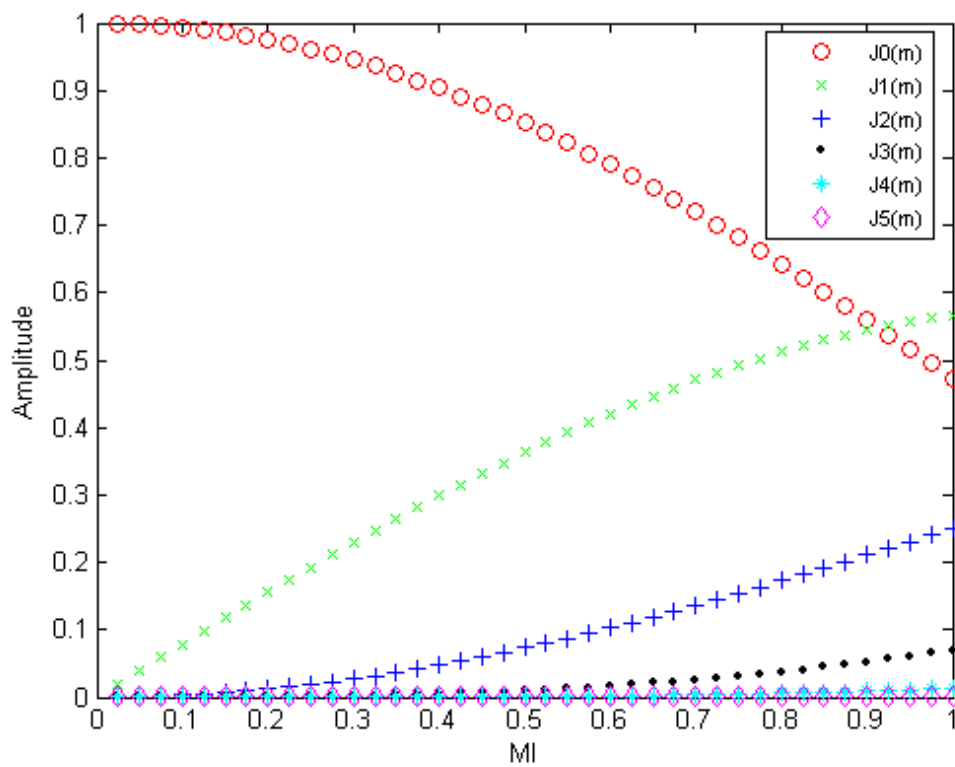


Fig. 2.7 Amplitude of the Bessel function varied with MI.

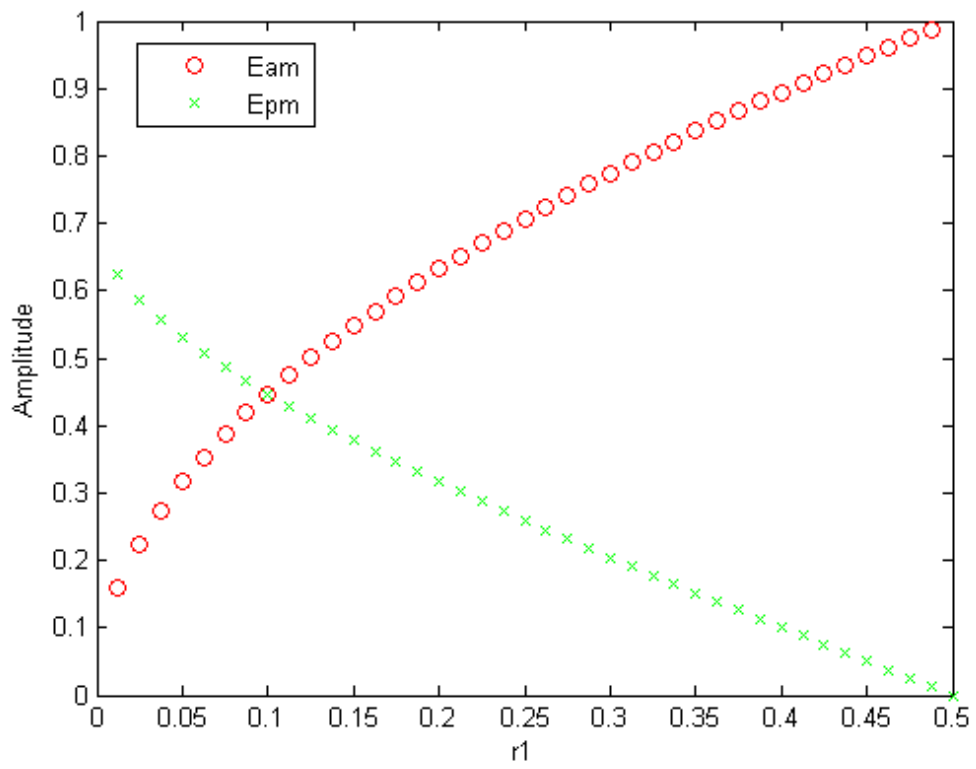


Fig. 2.8 E_{AM} and E_{PM} varied with r_1 .

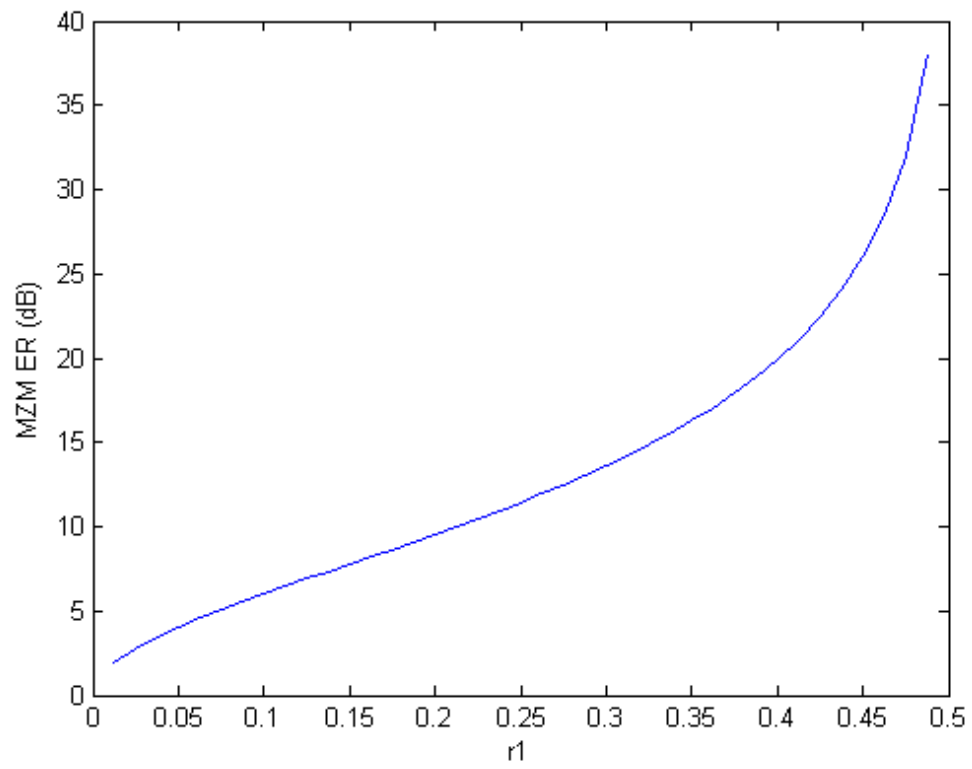


Fig. 2.9 MZM ER varied with r_1 .

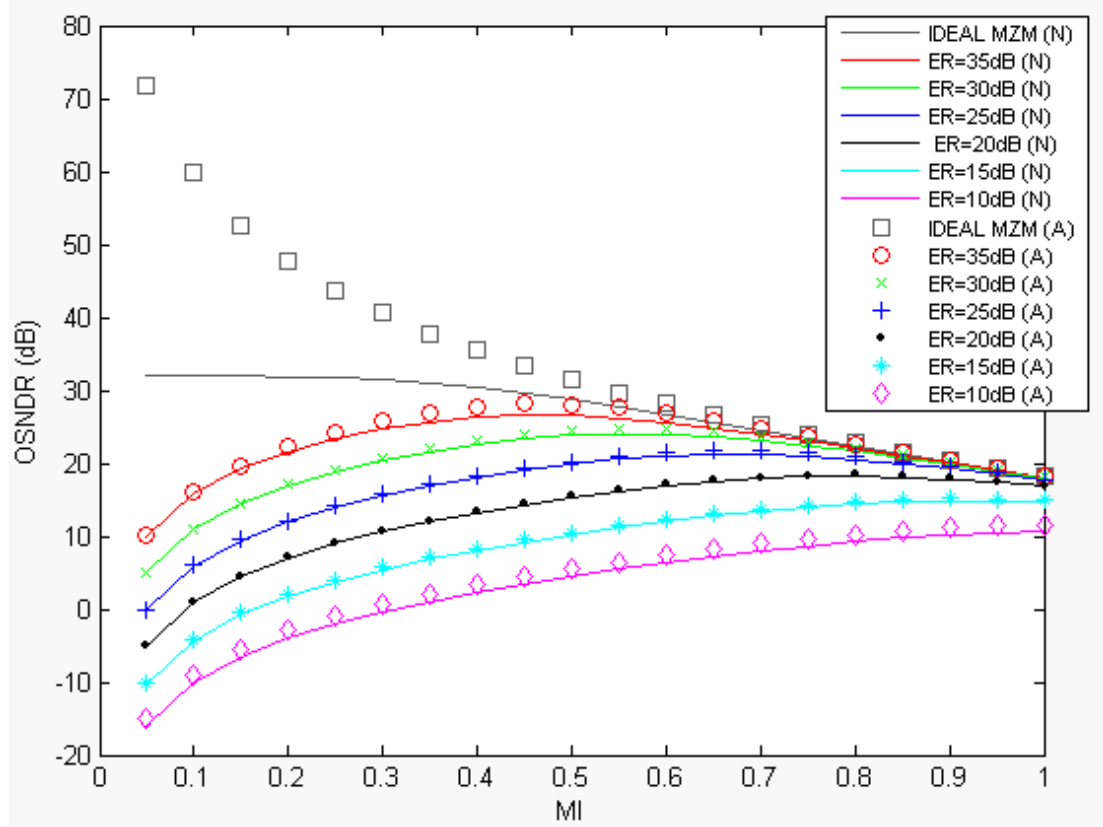


Fig. 2.10 OSNDR of the optical mm-wave signals varied with MI. A: Analytic stimulation, N: Numeric stimulation.

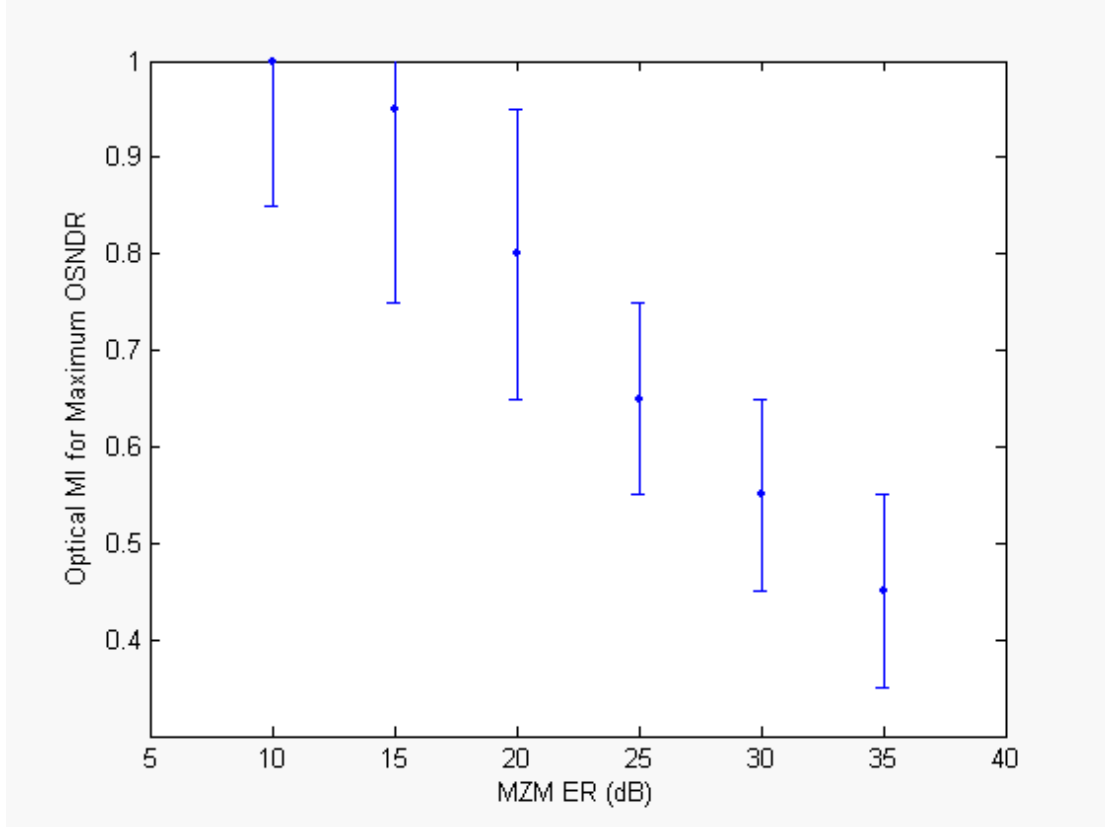


Fig. 2.11 Optimal MI for maximum OSNDR of the optical mm-wave signals.

The solid spot indicates the optimal MI for each MZM ER. The range of optimal MI comes from 1-dB tolerance of the maximum OSNDR.

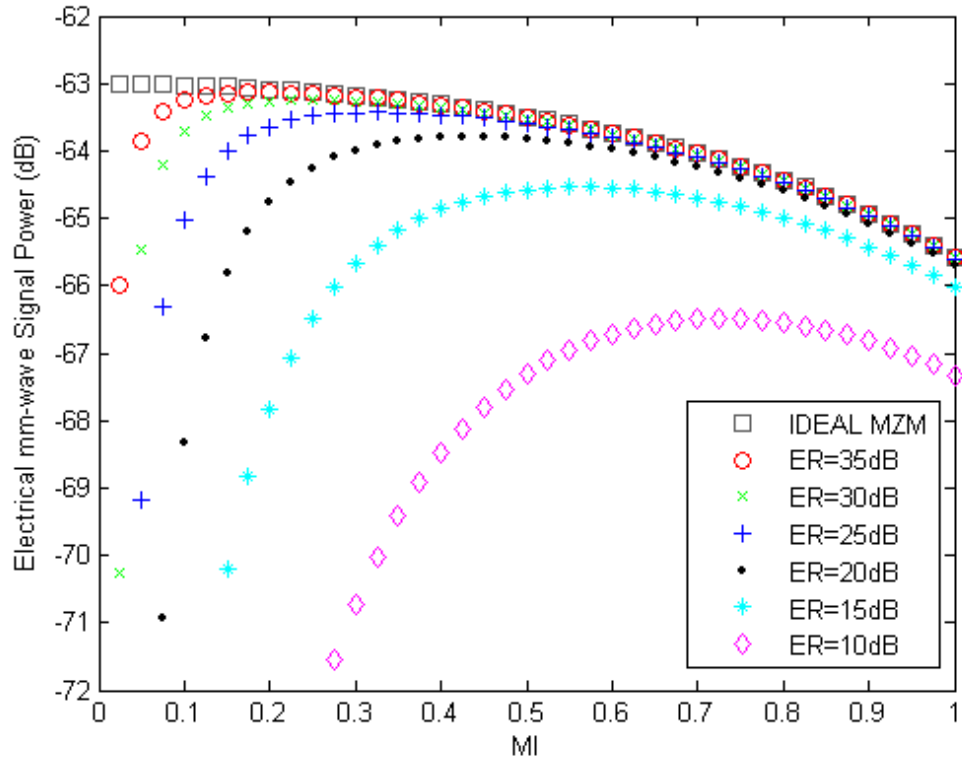


Fig. 2.12 Desired electrical mm-wave signals varied with MI after PD detection.

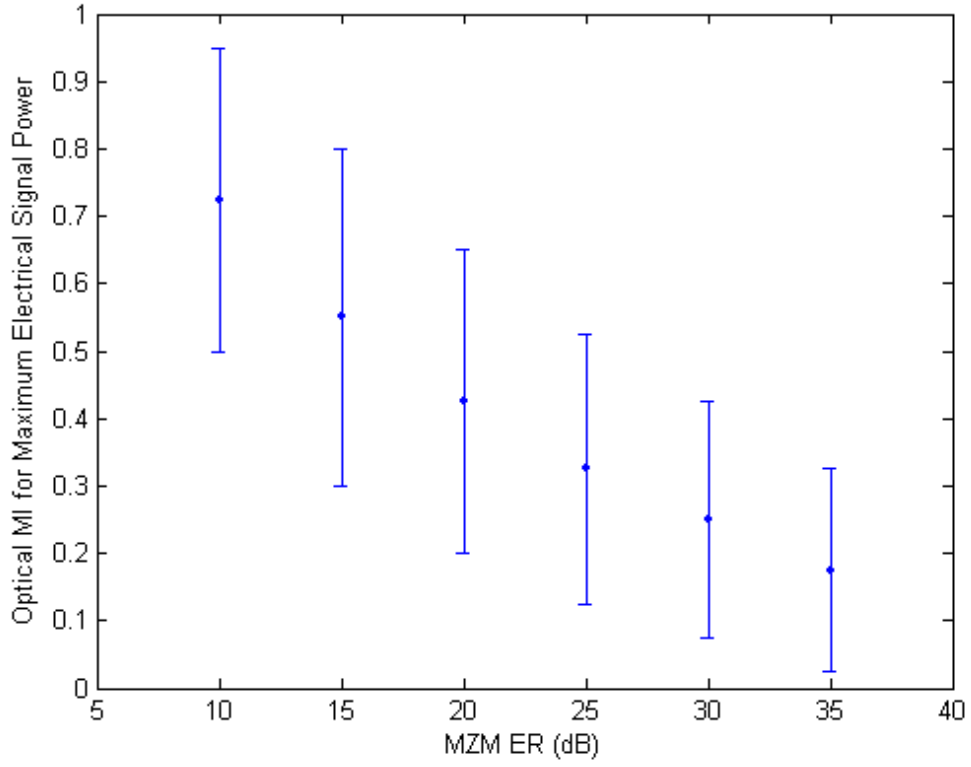


Fig. 2.13 Optimal MI for the electrical mm-wave signal generation. The solid spot indicates the optimal MI for each MZM ER. The range of optimal MI comes from 1-dB tolerance of the maximum power of the electrical mm-wave signal.

Chapter 3

Optical Convergence Access Network Providing Wired-Line and Wireless Signals

Recently, the optical-wireless networks offering both broadband wireless and wired services have attracted a lot of attention [1-5]. This architecture can provide both advantages from both sides: mobility and point-to-multi-points access technology from ultra wideband wireless network, and high bandwidth and highly reliable connection from optical access network. The key issue is to generate and transmit wireless and wired-line signals simultaneously. In this chapter, we propose and experimentally demonstrate dual-service optical-wireless access network providing wireless and wired-line signals and hybrid access network integrating RoF and FTTH systems. Moreover, optimum conditions for the mm-wave generation using DSBCS modulation will be experimentally investigated.

3.1 Dual-Service Optical-Wireless Access Network

In this section, we propose a novel optical-wireless network offering a simple method to simultaneously generate the RF and BB signals using only one MZM. The DSBCS modulation scheme using external MZM is utilized to generate the RF signals. Since the MZM is operated at the nonlinear region, we

study the relationship between the RF modulation index ($MI_{RF}=V_{p-p}/2V_{\pi}$) for driving DD-MZM and the receiver sensitivity to investigate the impact of the MZM nonlinearity on the performance of BB and RF signals. When MI is set to 0.43, there is 1dB improvement for the receiver sensitivity of the RF signal based on DSBCS modulation scheme and on power penalty for BB signals is observed. Based on this result, only one SD-MZM is needed to generate the mm-wave based on DSBCS modulation scheme, which is more compact and cost-effective. We also prove that BB signals are more robust to the fiber nonlinearity than the RF signals.

3.1.1 Experimental Setup

Figure 3.1 shows the experimental setup used for the simultaneous generation and transmission of optical RF and BB signals based on DSBCS modulation scheme. The continuous wave (CW) laser is generated by a distributed feedback laser, and the emission wavelength is 1540 nm. The BB signal is 622 Mb/s pseudo random bit sequence (PRBS) signal with a word length of $2^{31}-1$ and up-converted with the 5 GHz clock as shown in inset (i) of Fig. 3.1. The up-converted signal is amplified to maximum peak-to-peak voltage (V_{p-p}) of 7 volt, limited by the commercial RF amplifier (Picosecond 5865). The CW laser is modulated via external SD-MZM or DD-MZM with half-wave voltage (V_{π}) of 5 volt. In order to realize DSBCS modulation, the MZM is biased at the minimum transmission point. The repetition frequency of the generated optical microwave is 10 GHz. The optical microwave and spectrum of RF signals are shown in insets (ii) and (iii) of Fig. 3.1, respectively. The generated RF signal is amplified by erbium-doped fiber amplifier (EDFA) and then filtered by a tunable optical filter with a bandwidth of 0.4 nm. After

transmitted over SSMF, the transmitted optical microwave signal is converted into an electrical microwave signal by a PD with a 3 dB bandwidth of 38 GHz, and the converted electrical signal is amplified by an electrical amplifier. In the BB path, a low-pass filter with a 3 dB bandwidth of 622 MHz is inserted to reject the undesired RF components. In the other path, the microwave signal is down-converted (DC) by a mixer with a 10 GHz clock, and then passes through a low-pass filter with a 3 dB bandwidth of 622 MHz. The eye diagrams of the DC and BB signals are shown in insets (iv) and (v) of Fig. 3.1, respectively. Both the DC and BB signals are tested by a bit-error-ratio (BER) tester. We set the fiber lengths to be 25, 50, 75 and 100 km.

3.1.2 Experimental Results and Discussion

Figure 3.2 and 3.3 show the variations of the receiver sensitivities and power penalties of the BB and DC signals with MI-RF, respectively. For the DC signal, the receiver sensitivity increases first and then decreases when MI-RF ranges from 1 to 0.13, and the best sensitivity is at MI-RF equal to 0.43. For the BB signal, no receiver sensitivity penalty is observed when MI-RF decrease from 1 to 0.43. As MI-RF changes from 0.43 to 0.28, the sensitivity degradation is only 0.3 dB at BER of 10^{-9} .

The MZM nonlinearity and OCSR are closely related to MI-RF. As MI-RF for MZM decreases, the MZM nonlinearity and OCSR decrease. The reduction of the MZM nonlinearity makes the duty cycle of optical microwaves closer to 0.5 as shown in Fig. 3.4. At the same optical power, optical microwaves smaller duty cycle have higher peak power, resulting in better receiver sensitivity of the DC signal. However, low OCSR means that the RF component of optical power is relative low and the dc component of optical

power at the center wavelength is relative high as shown in Fig. 3.5. This incurs worse receiver sensitivity of the DC signal. Therefore, there is a trade-off for the receiver sensitivity of the DC signal between the MZM nonlinearity and OCSR when we decrease MI-RF. The result is in accordance with the theoretical simulation in previous chapter.

When the optimal MI-RF is 0.43, the receiver sensitivities of the BB and DC signals at BER of 10^{-9} are -22.6 dBm and -22.7 dBm, respectively. The receiver sensitivity of the DC signal has 1 dB improvement when MI-RF changes from 1 to 0.43. After optical microwaves with optical power of 0 dBm, using the optimal MI-RF equal to 0.43, are transmitted over 25 km, 50 km, and 75 km SSMF, the power penalty for the receiver sensitivities of the BB and DC signals at BER of 10^{-9} is less than 0.2dB as shown in Fig. 3.6.

Based on the result of DSBCS modulation using one DD-MZM, we can generate DSBCS microwaves using only one SD-MZM with MI-RF equal to 0.43. The V_{π} of the SD-MZM at 5GHz is 5 volt, and the V_{p-p} for the MI-RF of 0.43 is 4.3 volt. Figure 3.7 shows the receiver sensitivities and power penalties of the BB and DC signals with optical power of 0dBm after they are transmitted over 25 km, 50 km and 75 km SSMF. The power penalties for both the BB and DC signals at BER of 10^{-9} are less than 0.3 dB.

We also study the impact of fiber nonlinearity on optical microwave signals. Figure 3.7 shows the power penalty of the receiver sensitivity at BER of 10^{-9} under various optical microwave powers. The BB signal shows better robustness to the impairments of fiber nonlinearity effects, and only 0.3 dB sensitivity penalty is observed when the optical microwave power increases from 0 to 10 dBm. However, the sensitivity of the DC signal degrades more severely when the optical microwave power increases to 10 dBm. The reason is

that the effect of both fiber nonlinearity and dispersion changes the duty cycle of optical microwaves as shown in insets (i)-(v) of Fig. 3.8. That is why the DC signal transmitted over 75 km SSMF has the worst receiver sensitivity. Therefore, we can conclude that the power penalty for both the receiver sensitivities of the BB and DC signals using only one SD-MZM based DSBCS scheme is less than 1.4 dB after transmitted over 100 km SSMF when the optical power ranges from 0 to 10 dBm.

In summary, this section presents a simultaneous generation of BB and RF signals based on DCBCS modulation scheme using only one MZM. The optimal MI-RF level for driving DD-MZM is 0.43 with 1 dB sensitivity improvement for DC signals, and there is no receiver sensitivity penalty after transmission over 75 km SSMF. Based on the optimal MI of 0.43, we can generate DSBCS microwaves using only one single-electrode MZM, which is more compact and cost-effective. The receiver sensitivity penalty is less than 0.3 dB after transmitted over 75 km SSMF. We also confirm that BB signals have better robustness to the impairment of fiber nonlinearity than RF signals.

3.2 Hybrid Optical Access Network

In this section, we propose a hybrid optical access network integrating RoF and FTTH systems. This proposed system provides the simultaneous modulation and transmission of a BB signal and a RF signal on a single wavelength over a single fiber. The BB and RF signals are independently modulated and transmitted at the optical carrier and subcarrier, respectively. In the proposed system, unlike [4-5], the RF signal does not suffer periodic

performance fading when it is transmitted over a SSF. The power penalties of both BB and RF signals are less than 0.2dB after transmission over 50km SSF, revealing the feasibility of the system.

3.2.1 Hybrid Optical Access Network Architecture

Figure 3.9 schematically depicts the hybrid optical access network system. An external integrated modulator using x-cut LiNbO₃ [6-7], consisting of three SD-MZM, is the key to generating RF and BB signals simultaneously. Two sub-MZMs (MZ-a and MZ-b) are embedded in each arm of the main modulator (MZ-c). Both DSB and DSBCS modulation schemes are used to generate the RF signals at MZ-a. The optical spectrums of RF signals are shown in inset (i) of Fig.3.9. The BB signal is generated at MZ-b and modulated at the optical carrier, as shown in the inset (ii) of Fig.3.9. The optical RF signal and BB signal are combined at MZ-c biased at the maximum transmission point. The inset (iii) of Fig.3.9 shows the optical spectrum of the hybrid signal. At a remote node, an optical filter is utilized to separate these two signals, as shown in inset (iv) and (v) of Fig.3.9, and each signal is transmitted to the corresponding application.

3.2.2 Experimental Setup

Figure 3.10 shows the experimental setup for hybrid signal generation and transmission using one external integrated modulator. The continuous wave (CW) laser is generated by a tunable laser, and the lasing wavelength is 1554.94nm. The RF signal is a 622Mb/s PRBS signal with a word length of $2^{31}-1$ and up-converted with the 10 GHz clock as shown in inset (i) of Fig.3.10. The up-converted RF signal is amplified to maximum V_{p-p} of 7V, limited by the

RF amplifier. The optical RF signal is generated via MZ-a with V_{π} of 5.8V. The MZ-a is biased at the minimum and quadrature transmission point to realize DSBCS and DSB modulation, respectively. The repetition frequencies of the generated optical microwave using DSBCS and DSB modulations are 20GHz and 10GHz, respectively. The generated optical microwave is shown in inset (ii) of Fig. 3.10. The BB signal is a 1.25Gb/s PRBS signal with a word length of $2^{31}-1$; it is sent into MZ-b with V_{π} of 5.6V. The eye diagram of the generated optical BB signal is shown in inset (iii) of Fig. 3.10. The optical RF and BB signals are combined at MZ-c with V_{π} of 6.9V biased at the maximum transmission point. The hybrid optical signals are amplified by an EDFA to compensate for the loss of the external modulator, yielding a power of 0dBm before transmission over 50km SSF. Following transmission over 50km SSF, the hybrid signals are preamplified by EDFA and then filtered by a tunable optical filter with a bandwidth of 0.4nm. At the remote node, the fiber grating with a 3dB bandwidth of 4GHz is used to separate these two signals, as shown in inset (iv) and (v) of Fig. 3.10, and each signal is sent to the corresponding application. Both optical signals are individually detected by a PIN PD. For FTTH applications, the electrical BB signal is filtered by a electrical filter with a 3dB bandwidth of 1.25GHz. For wireless applications, the electrical RF signal is down-converted by a mixer with a 20GHz clock before passing through a low-pass filter with a 3dB bandwidth of 622MHz. The eye diagrams of BB and RF signals are shown in inset (vi) and (vii) of Fig. 3.10, respectively. Both RF and BB signals are tested by a BER tester and the receiver sensitivities are measured before EDFA pre-amplification. The fiber lengths are set at 25 and 50km.

3.2.3 Experimental Results and Discussion

Since the BB and RF signals are generated at different sub-MZs, these two signals can be optimized individually. Especially, the RF signal performance is strongly related to MZM nonlinearity. To optimize the RF signal performance, the RF modulation index $MI_{RF} = V_{p-p}/2V_{\pi}$ and $MI_{RF} = V_{p-p}/V_{\pi}$ for driving MZ-a based on DSBCS and DSB modulation schemes decreases to reduce the MZM nonlinearity, respectively, and no BB signals are sent to MZ-b biased at the minimum transmission point. Figure 3.11 shows the variation of the receiver sensitivity of the RF signal using DSBCS modulation with different MI_{RF} . The RF receiver sensitivity initially improves and then declines as the MI_{RF} decreases from 0.6 to 0.1. When MI_{RF} is 0.48, the RF signals exhibit the best sensitivity. The optimal MI_{RF} for RF signals using DSBCS modulation originates from the trade-off between the MZM nonlinearity and the OCSR for the RF receiver sensitivity when MI_{RF} is decreased. This has been theoretically and experimentally in chapter 2 and section 3.1.

For RF signals using DSB modulation, the result is different as shown in Fig.3.12. As MI_{RF} decreases, not only MZM nonlinearity decreases but also optical modulation index (OMI) of the RF signals decreases. Reduction of MZM nonlinearity can improve RF sensitivity, but reduction of OMI will degrade RF sensitivity. However, the OMI dominates the RF performance as shown in Fig. 3.13. Therefore, As MI_{RF} decreases, the RF sensitivity degrades. The optimal MI_{RF} for RF signals using DSB modulation is 1.

After finding the optimal driving condition for MZ-a, there are two ways

to control the optical power ratios of the RF and BB signals to the hybrid signals. One is to control the splitting ratio before MA-a and MZ-b. However, the optical power ratios of the RF and BB signals to the hybrid signals is not adjustable after the integrated MZM is fabricated. Therefore, we propose the other method. The optimal MI-RF for driving MZ-a is fixed at 0.48, and then the BB signal is sent to MZ-b. The BB modulation index (MI-BB) for driving MZ-b decreases from 1 to 0.18. The bias point of MZ-b is adjusted to maximize the ER of the BB signal as MI-BB varies from 1 to 0.18. As MI-BB decreases, the optical power ratios of the RF and BB signals to the hybrid signals increase and decrease, respectively. Hence, the BB sensitivity increases and the RF sensitivity decreases as MI-BB ranges from 1 to 0.18, as shown in Fig. 3.14. For RF signals using DSBCS modulation, the same sensitivities of the RF and BB signals can be achieved as the MI-BB is 0.27. However, for RF signals using DSB modulation, the same sensitivities of the RF and BB signals cannot be achieved, and even error floor is observed when MI-BB is 0.27. Therefore, the DSBCS modulation is the best choice for the RF signal generation in the proposed system.

In this study, we did not consider the RF signals transmitted over air. For the real situation, the requirements of the RF and BB signals are different. The optical power ratios of the RF and BB signals to the hybrid signals should be controlled to meet the different requirements. Therefore, the interference between BB and RF signals is needed to concern when we control the optical power ratios of the RF and BB signals to the hybrid signals [4-5]. The RF sensitivity is measured after the fiber grating as shown in Fig.3.15. Figure 3.16 shows that the RF sensitivity deviation is less than 0.3dB as optimal MI-RF is fixed at 0.48 and MI-BB ranges from 1 to 0.18. Hence, unlike in other works

[4-5], various MI-BBs for driving MZ-b cannot influence the RF signal performance when optimal MI-RFs for driving MZ-a are maintained. Therefore, our proposed system can meet different RF and BB signal performance requirements without fading RF and BB signals.

Under optimal conditions using DSBCS modulation for RF signals to drive MZ-a and MZ-b, the receiver sensitivities of the RF and BB signals are -37.2dBm and -36.8dBm at BER of 10^{-9} , respectively. Then the optical hybrid signals at an optical power of 0dBm are transmitted over 25km and 50km SSMF. Figure 3.17a plots the BER curves of the RF and BB signals. The power penalties of both signals at a BER of 10^{-9} are less than 0.2dB, as shown in Fig.3.17b.

In conclusion, this section experimentally demonstrates the simultaneous modulation and transmission of FTTH BB and RoF RF signals using one external integrated modulator. The generated hybrid signals do not suffer from periodic performance fading problem caused by fiber dispersion. The receiver sensitivity penalties of both RF and BB signals are less than 0.2dB after transmission over 50km SSMF. The results reveal that the proposed system has great potential for use in future multi-service access networks.

References

- [1] G. K. Chang, J. Yu, Z. Jia and J. Yu, "Novel optical-wireless access network architecture for simultaneously providing broadband wireless and wired services," 2006 Optical Fiber Communication Conference (OFC 2006), OFM1, Anaheim, California, March 05-10, 2006.
- [2] J. Yu, Z. Jia, L. Yi, G. K. Chang, and T. Wang, "Optical millimeter-wave

generation or up-conversion using external modulator,” IEEE Photon. Technol. Lett., vol. 18, pp. 265-267, 2006.

- [3] A. Martinez, V. Polo, and J. Marti, “Simultaneous baseband and RF optical modulation scheme for feeding wireless and wireline heterogeneous access network,” IEEE Trans. Microwave theory and Technol., vol. 49, pp. 2018-2024, 2001.
- [4] T. Kamisaka, T. Kuri, K. Kitayama, “Simultaneous modulation and fiber-optic transmission of 10Gb/s baseband and 60GHz band radio signals on a single wavelength,” IEEE Trans. Microwave theory and Technol., vol. 49, pp. 2013-2017, 2001.
- [5] K. Ikeda, T. Kuri, and K. Kitayama, “Simultaneous three band modulation and fiber-optic transmission of 2.5Gb/s baseband, microwave-, and 60GHz band signals on a single wavelength,” IEEE J. Lightwave Technol., vol. 21, pp. 3194-3202, 2003.
- [6] T. Kawanishi, K. Higuma, T. Fujita, S. Mori, S. Oikawa, J. Ichikawa , T. Sakamoto and M. Izutsu , “40Gbit/s Versatile LiNbO₃ Lightwave Modulator ,” European Conference on Optical Communication (ECOC 2005), Glasgow, Scotland, Paper No.: Th2.2.5, 2005.
- [7] T. Sakamoto, T. Kawanishi, and M. Izutsu, “Continuous-Phase Frequency-Shift Keying With External Modulation,” IEEE Journal OF Selected Topics in Quantum Electronics, Vol. 12, no. 4, pp. 589-595, July/August 2006.

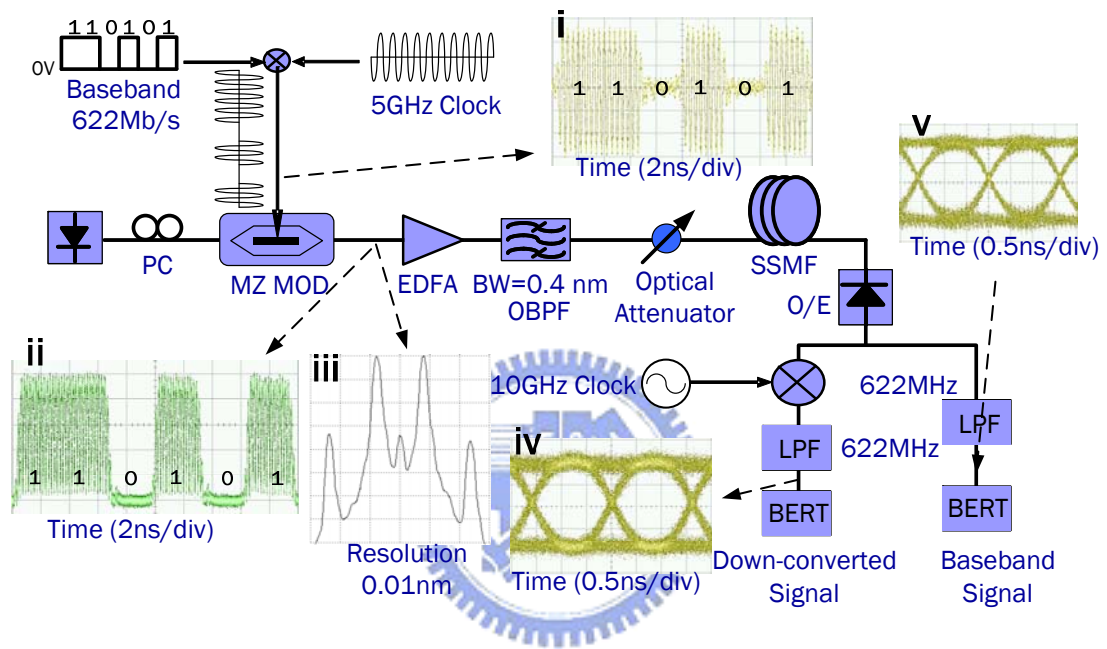
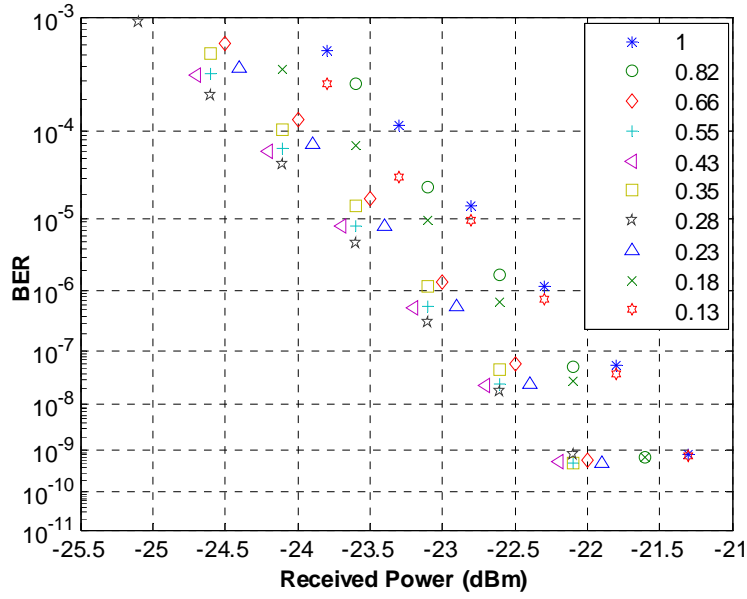
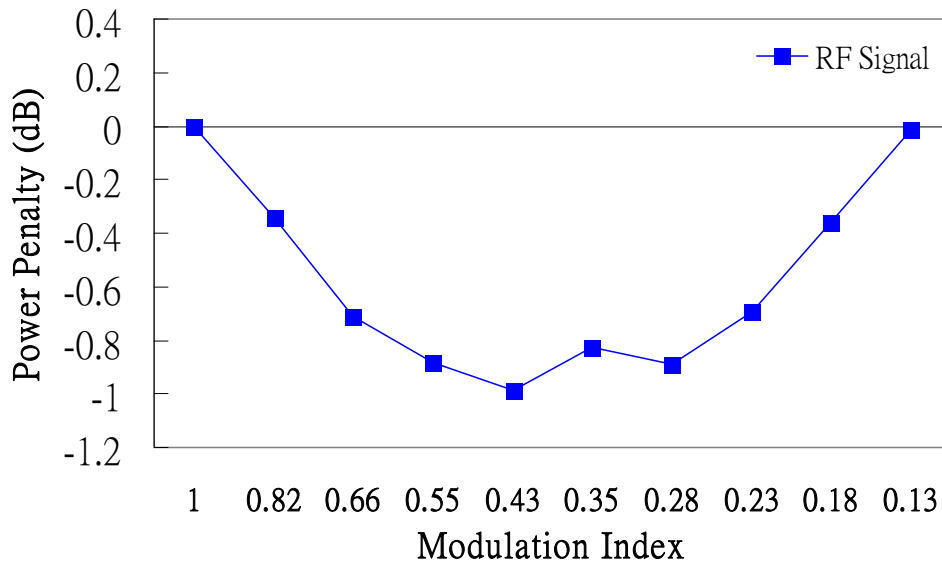


Fig. 3.1 Experimental setup for the generation and transmission of optical RF and BB signals based on DSBSCS modulation scheme using one MZM.

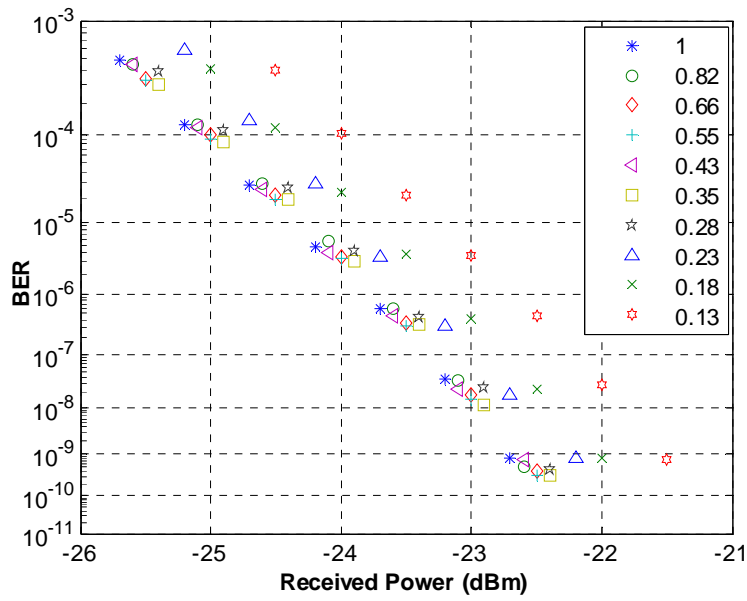


(a)

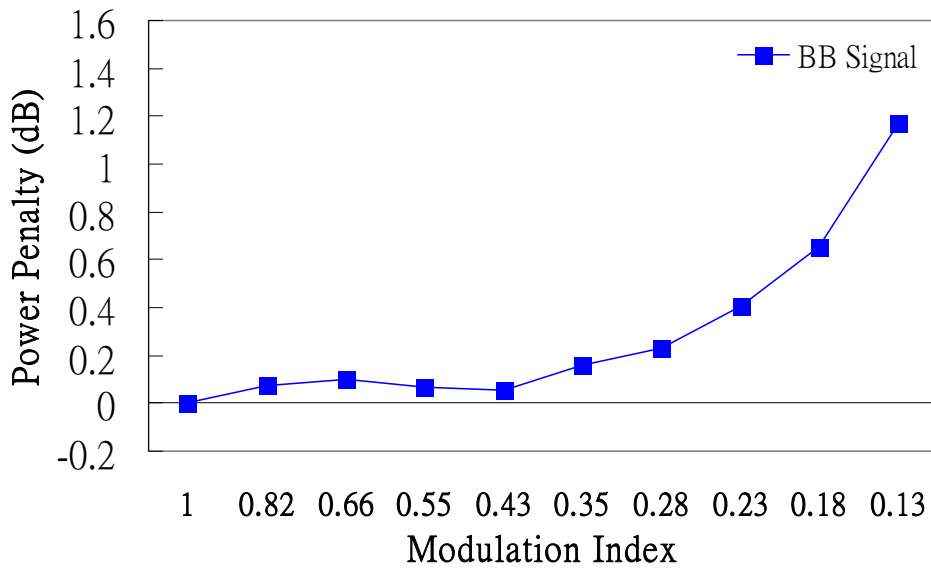


(b)

Fig. 3.2 BER curves (a) and power penalties at BER of 10^{-9} (b) of DC signals for different MI-RF.



(a)



(b)

Fig. 3.3 BER curves (a) and power penalties at BER of 10^{-9} (b) of BB signals for different MI-RF.

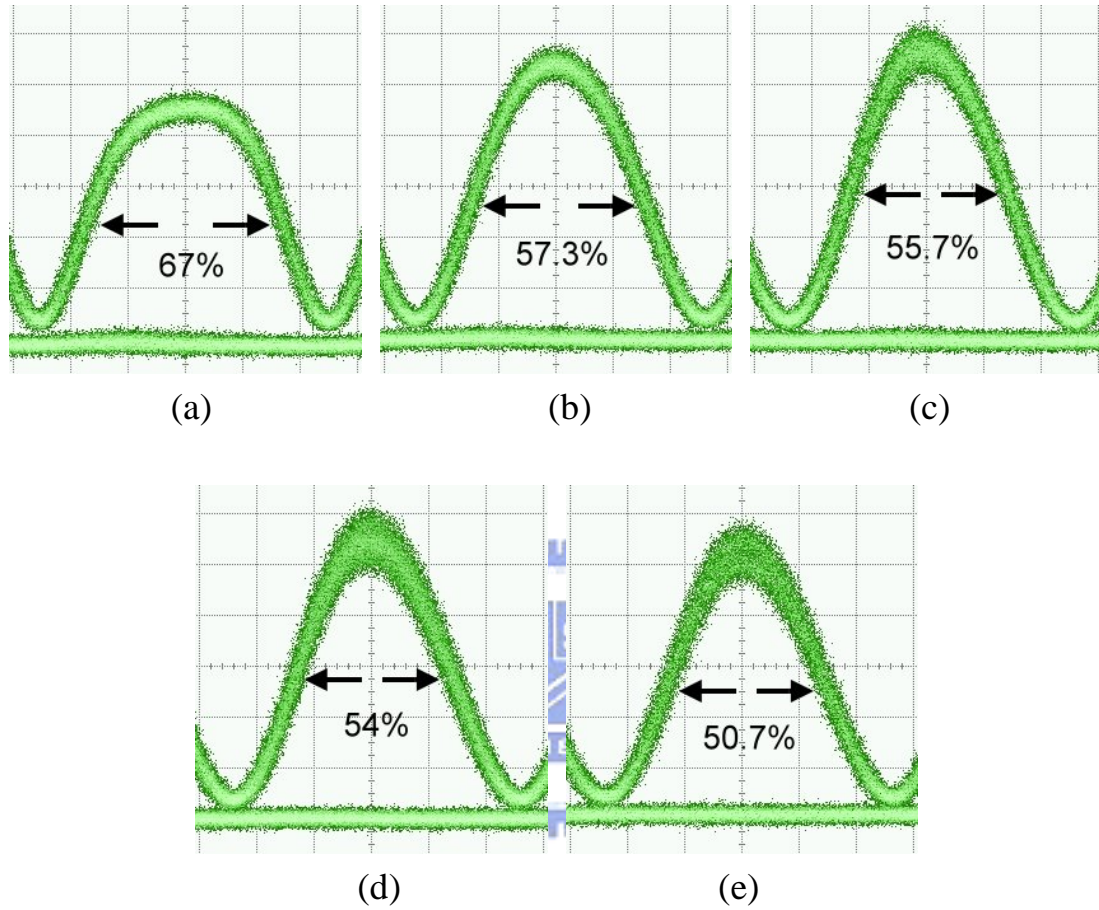


Fig. 3.4 Duty cycles of optical microwaves based on DSBCS modulation. The optical microwave power is 1dBm. The optical power scale is 0.8 mW/div and the time scale is 20 ps/div. The MI-RF is set at (a) 1 (b) 0.66 (c) 0.43 (d) 0.28 (e) 0.18.

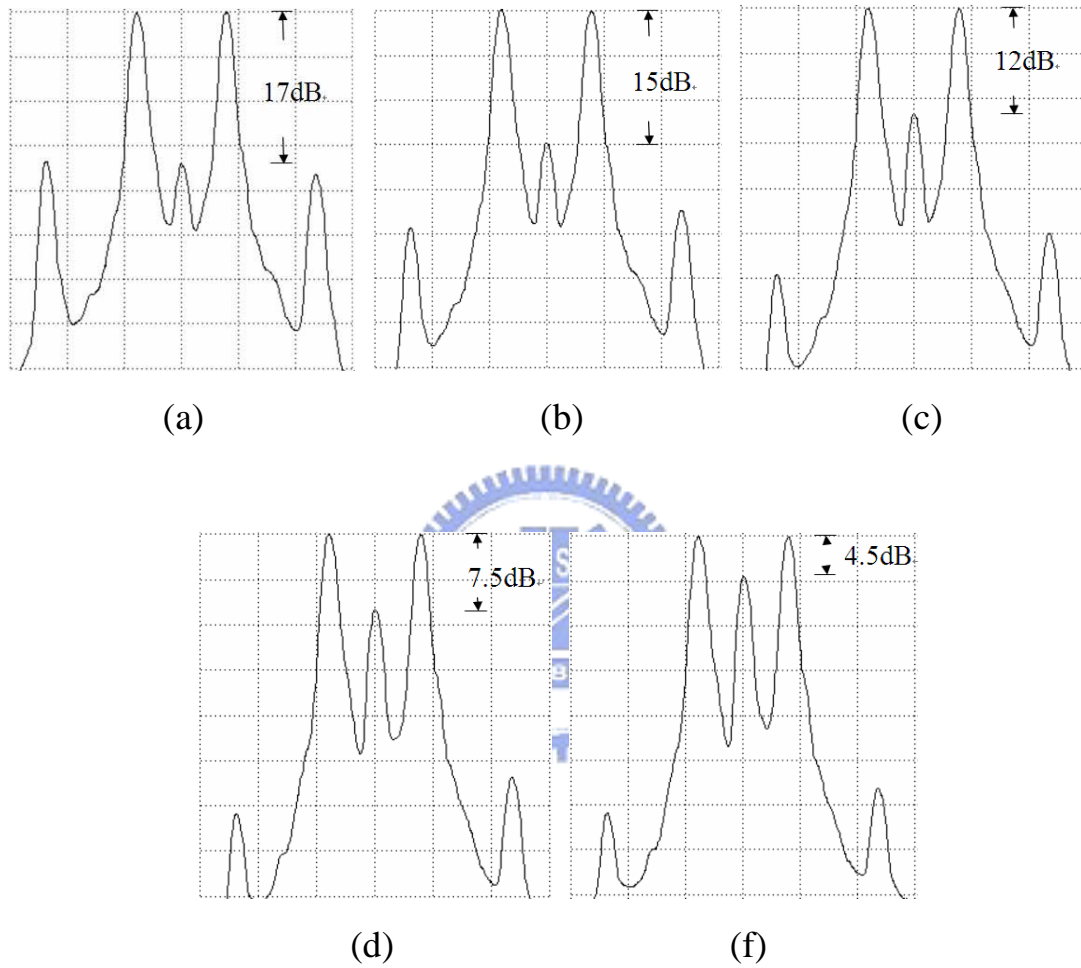
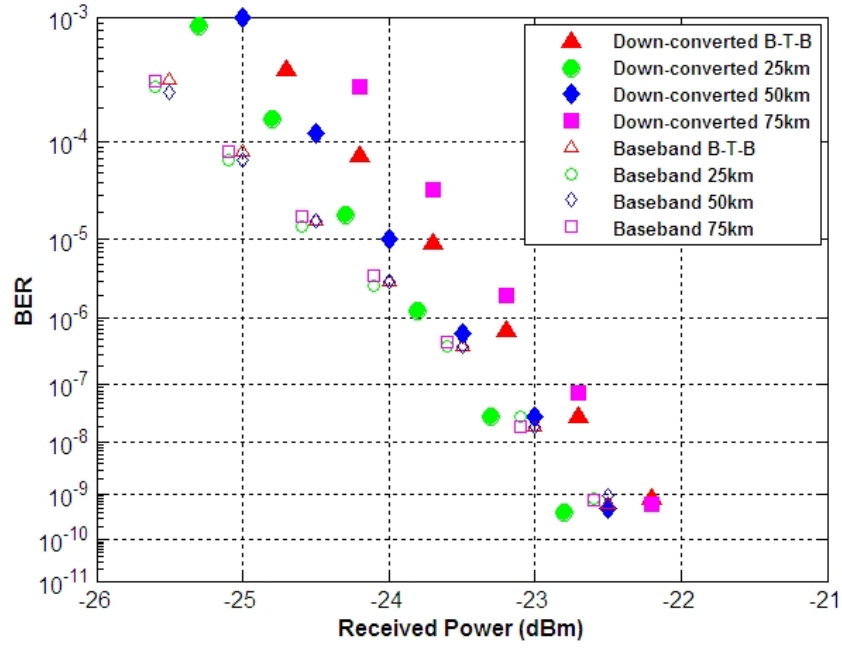
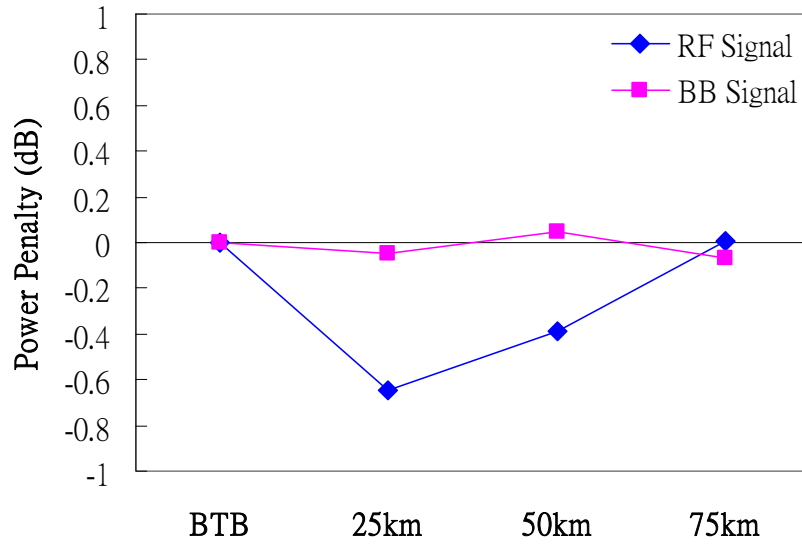


Fig. 3.5 The OCSR of optical microwaves based on DSBCS modulation. The resolution is 0.01nm. The MI-RF is set at (a) 1 (b) 0.66 (c) 0.43 (d) 0.28 (e) 0.18

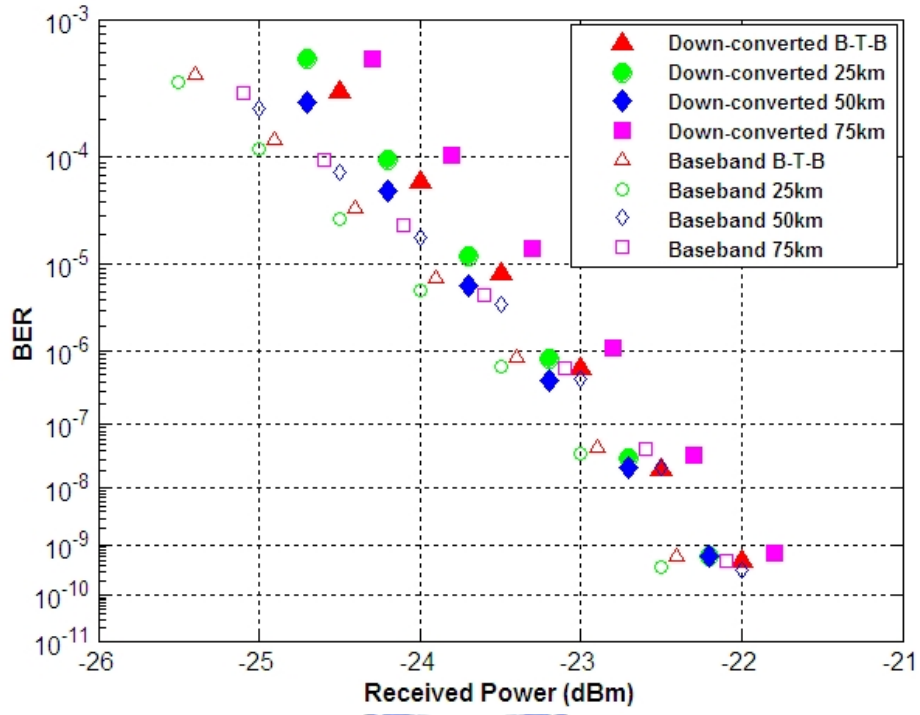


(a)

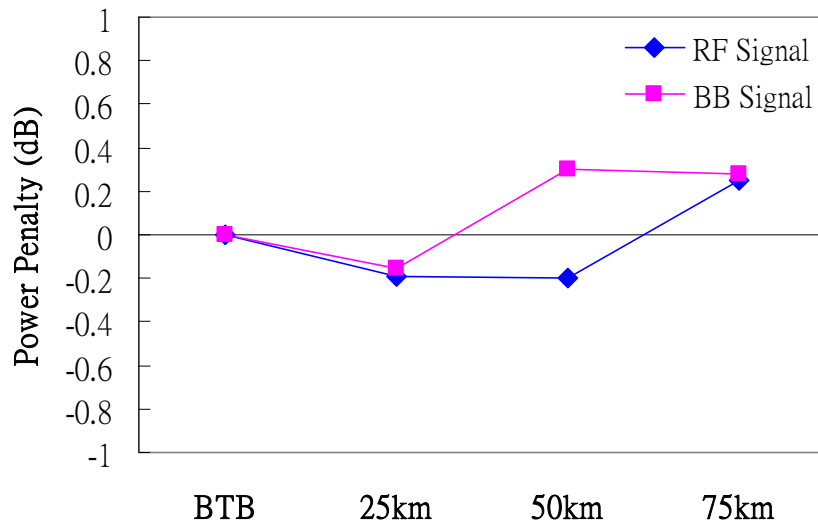


(b)

Fig. 3.6 BER curves (a) and power penalties at BER of 10^{-9} (b) using one DD-MZM with MI-RF of 0.43 after transmission over 25 km, 50 km and 75 km SSMF.



(a)



(b)

Fig. 3.7 BER curves (a) and power penalties at BER of 10^{-9} (b) using one SD-MZM with MI-RF of 0.43 after transmitted over 25 km, 50 km, and 75 km SSMF.

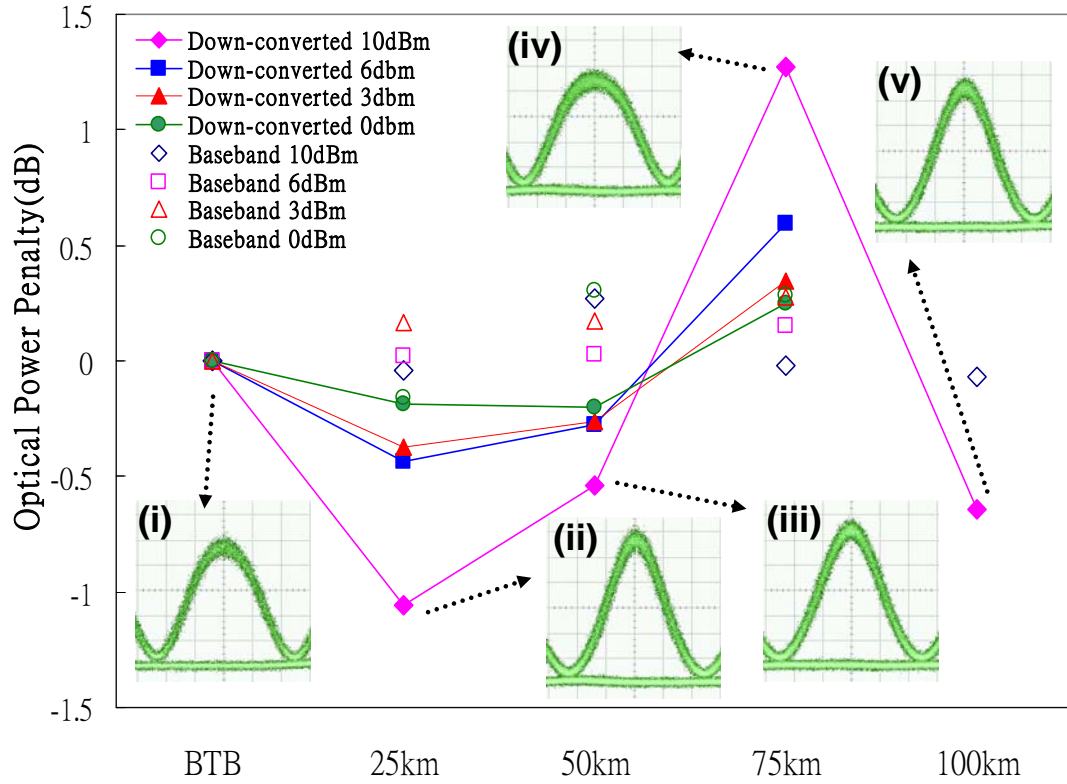


Fig. 3.8 Fiber nonlinearity impairment of the receiver sensitivity. The MI-RF for SD-MZM is 0.43. The optical power scale is 0.8 mW/div and the time scale is 20 ps/div. (i)10 dBm, BTB (ii)10 dBm, 25 km (iii)10 dBm, 50 km (iv)10 dBm, 75 km (v)10 dBm, 100 km

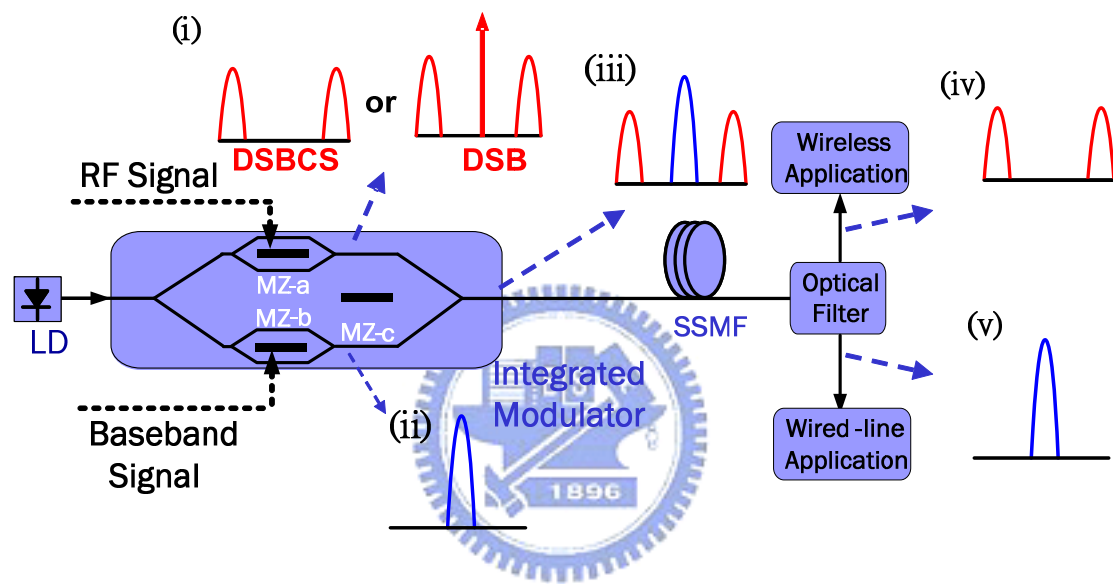


Fig. 3.9 Schematic diagram of the hybrid optical access network.

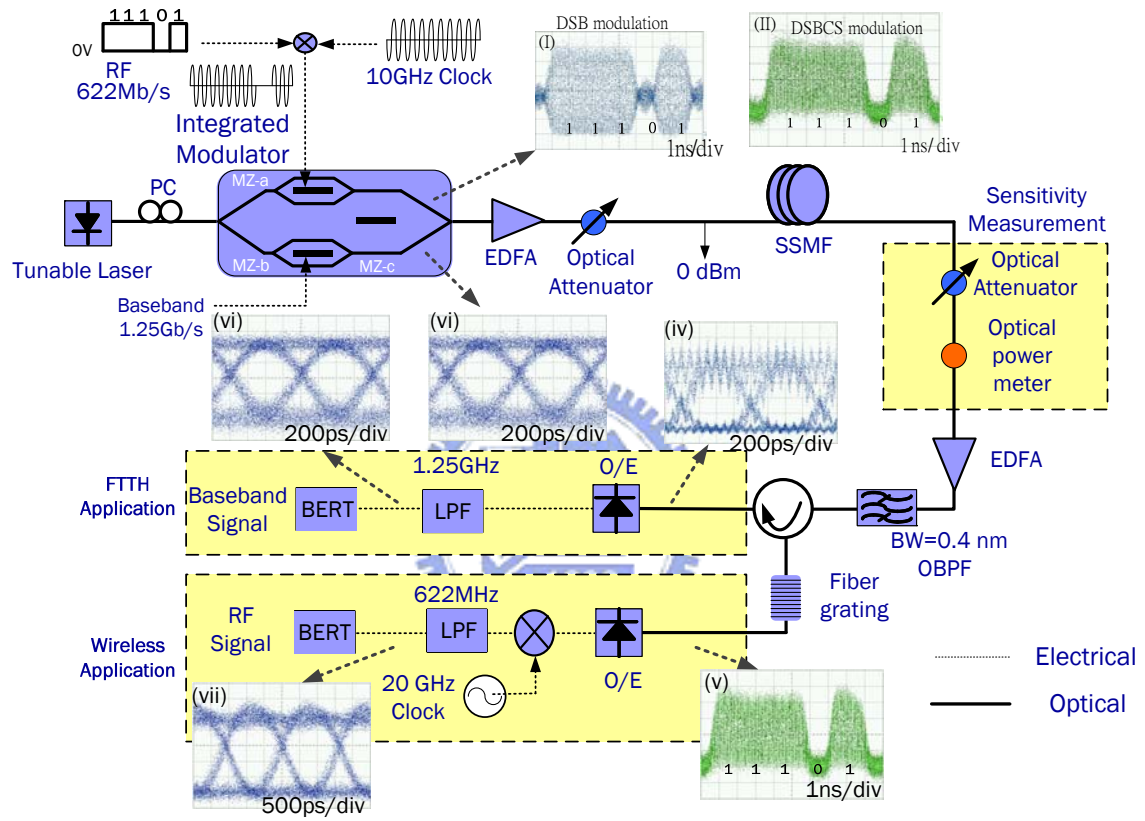
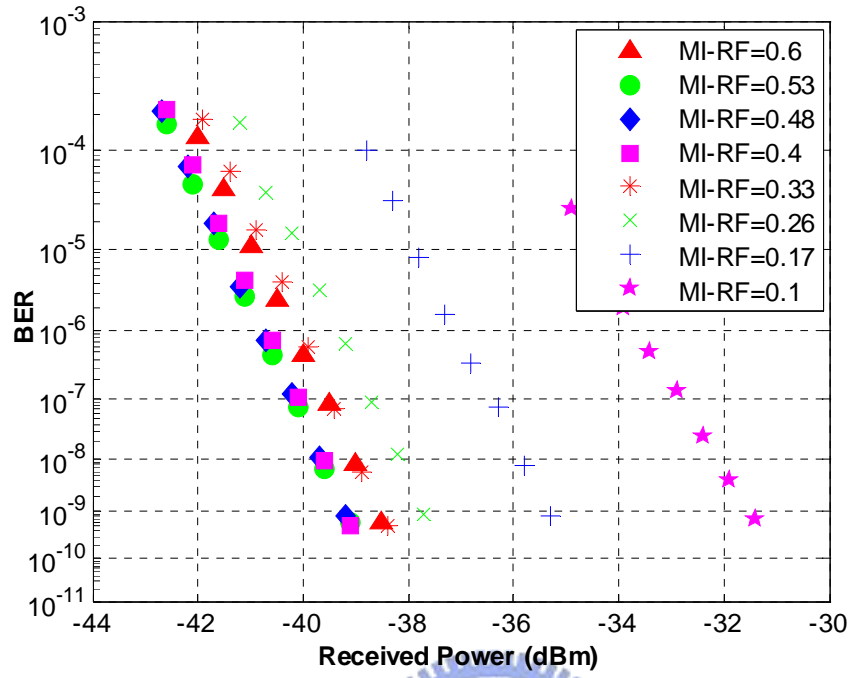
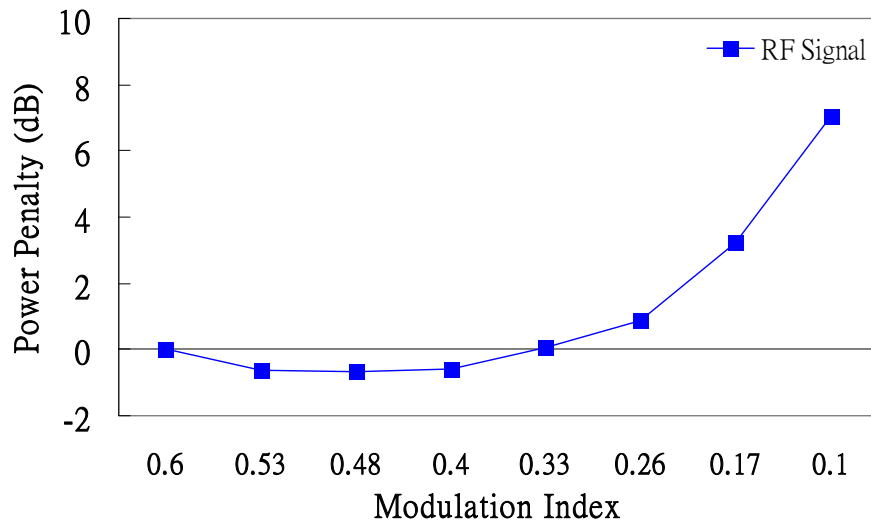


Fig. 3.10 Experimental setup for RF and BB signal generation and transmission using one external integrated modulator.



(a)



(b)

Fig. 3.11 BER curves (a) and power penalties at BER of 10^{-9} (b) of RF signals using DSBCS modulation for MI-RF from 0.6 to 0.1.

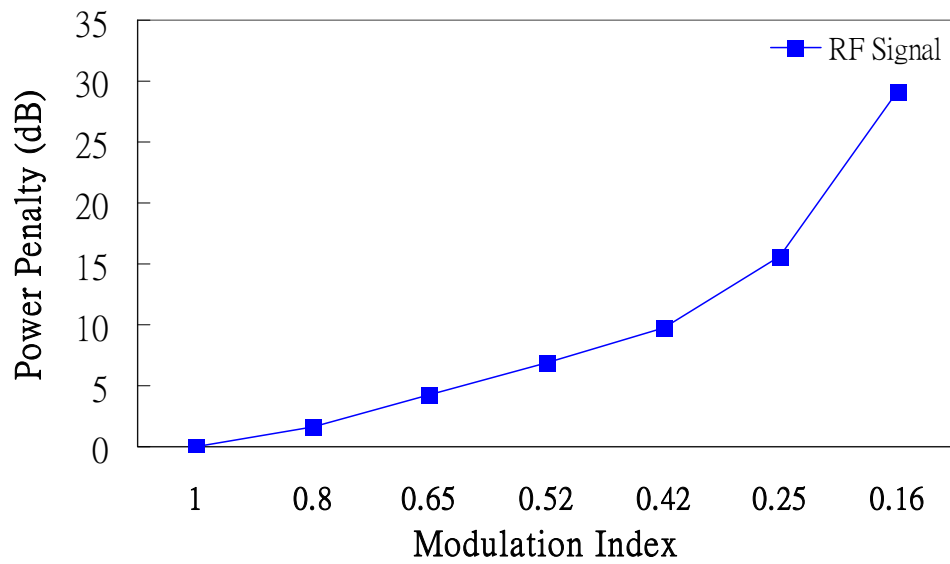
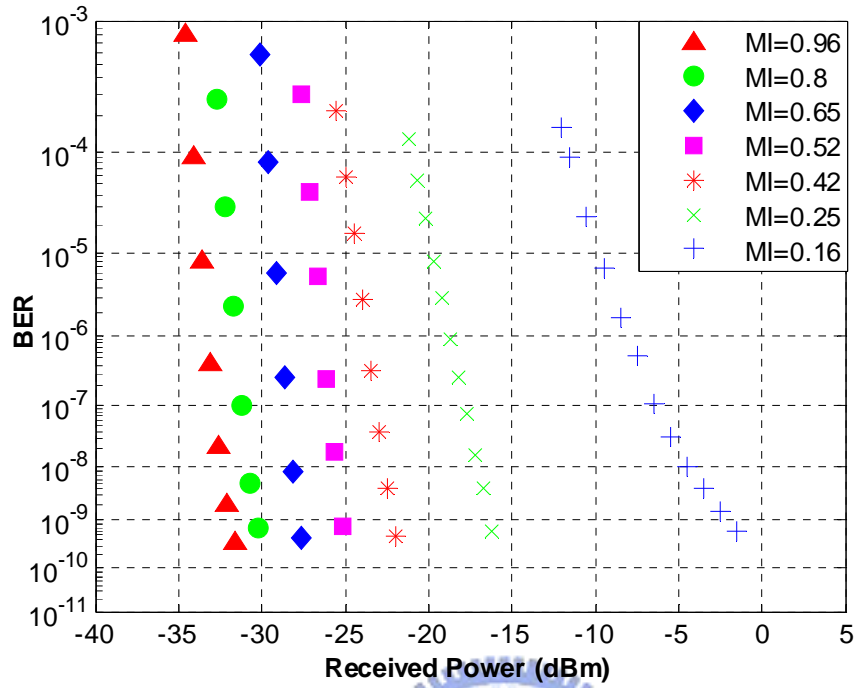


Fig. 3.12 BER curves (a) and power penalties at BER of 10^{-9} (b) of RF signals using DSB modulation for MI-RF from 1 to 0.16.

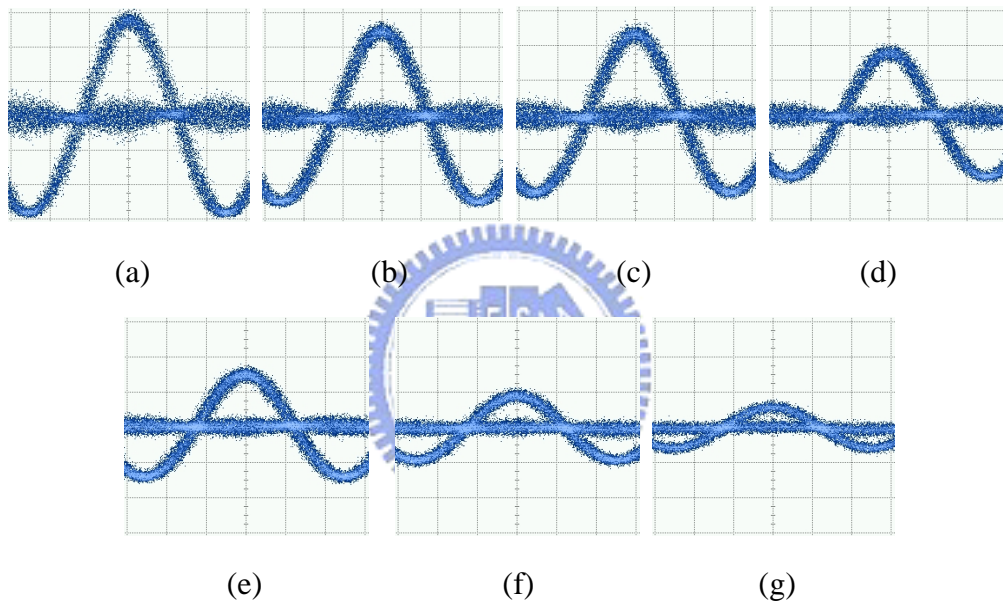
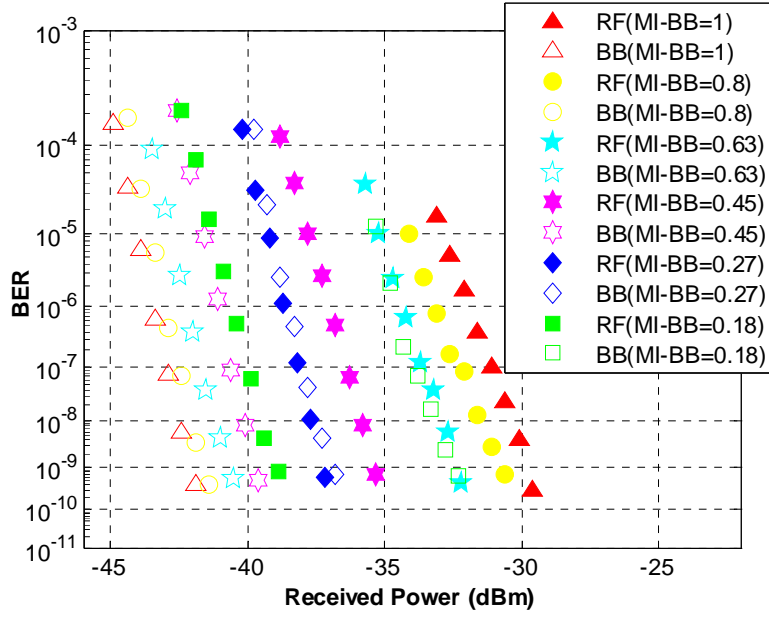
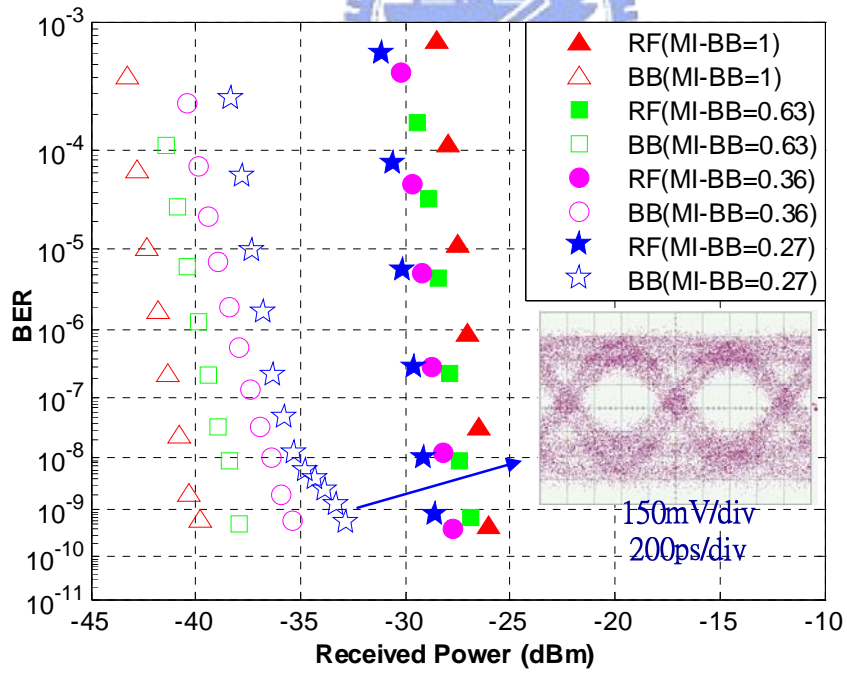


Fig. 3.13 Eye diagrams of RF signals using DSB modulation for MI-RF from 1 to 0.16. (a) MI-RF=1 (b) MI-RF=0.8 (c) MI-RF=0.65 (d) MI-RF=0.52 (e) MI-RF=0.42 (f) MI-RF=0.25 (g) MI-RF=0.16. (Power scale: 270μ W/div, Time scale: 20ps/div)



(a)



(b)

Fig. 3.14 BER curves of BB and RF signals for MI-BB from 1 to 0.18. MI-RF is fixed at 0.48.

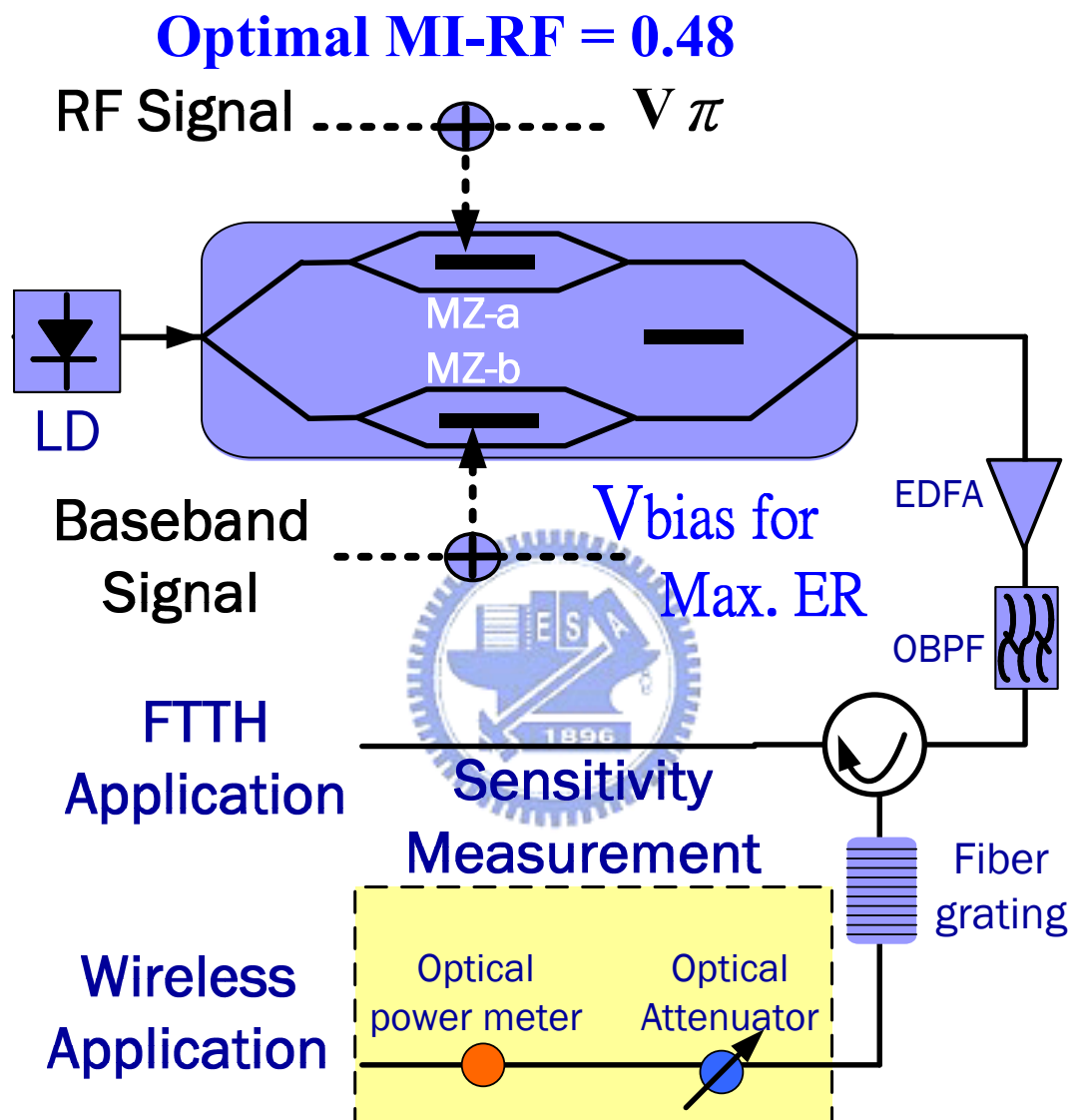
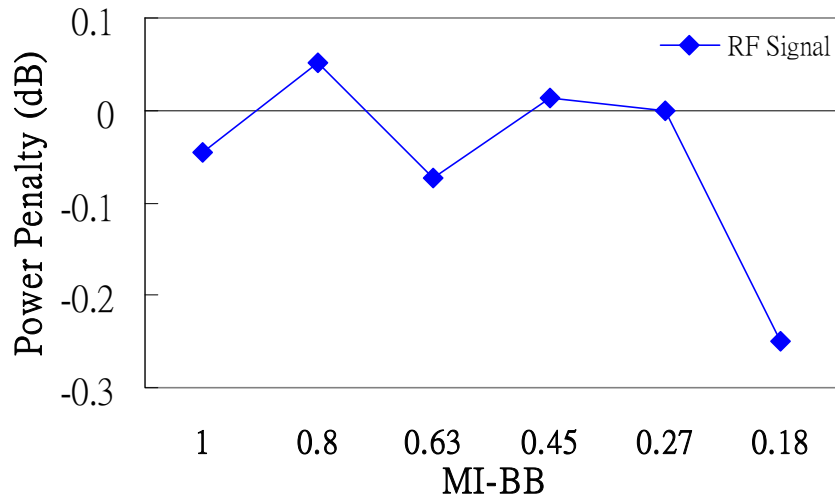
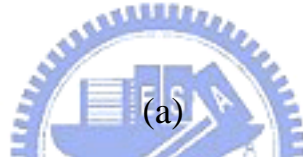
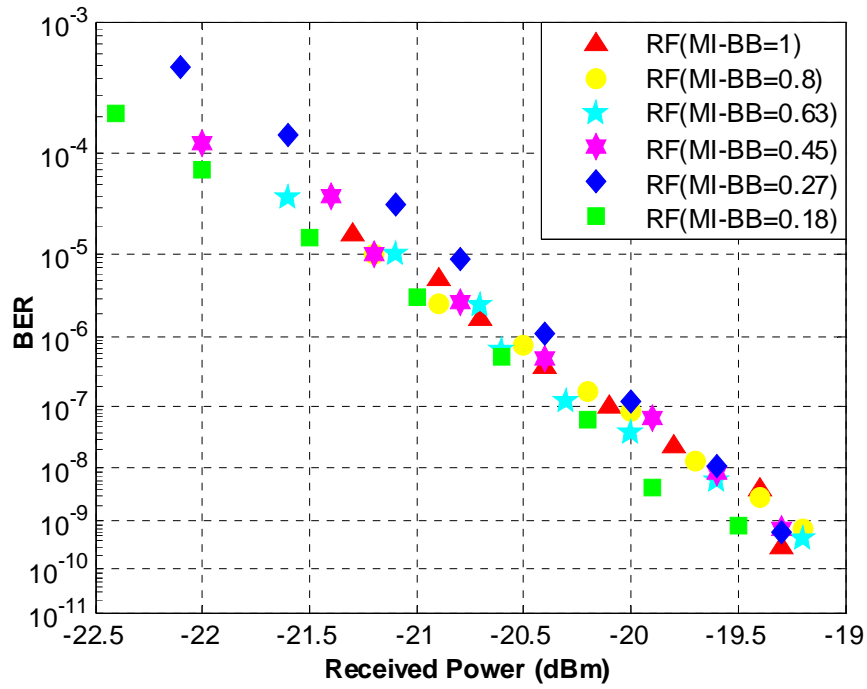
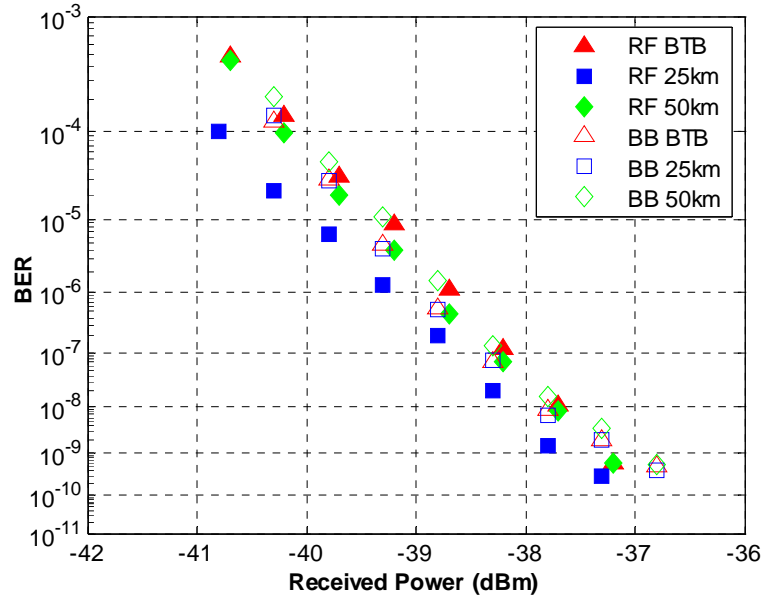


Fig. 3.15 Experimental setup to study the interference between BB and RF signals.

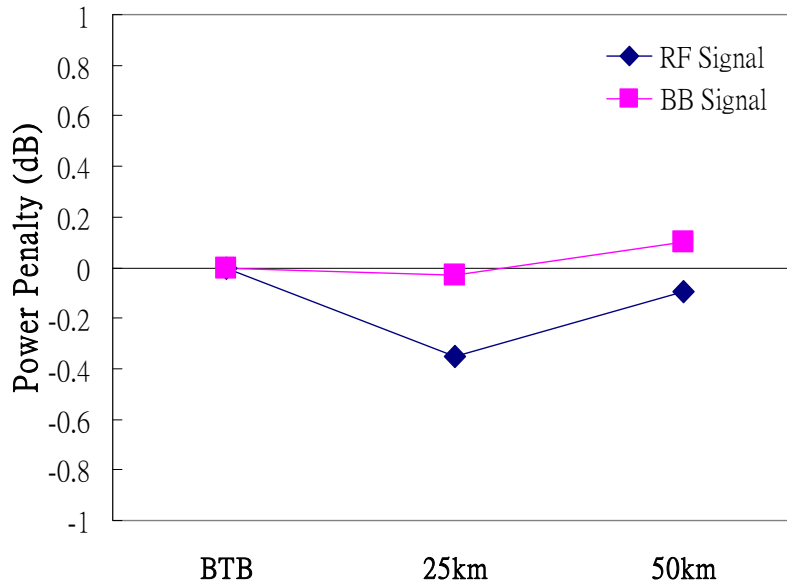


(b)

Fig. 3.16 BER curves (a) and power penalties at BER of 10^{-9} (b) of the RF signals using DSBCS modulation with optimal MI-RF and varied MI-BB.



(a)



(b)

Fig. 3.17 BER curves (a) and power penalties at BER of 10^{-9} (b) of both BB and RF signals using DSBCS modulation following transmission over 25 km and 50 km SSMF. The optimal MI-RF and MI-BB for driving MZ-a and MZ-b are 0.48 and 0.27, respectively.

Chapter 4

Cost-Effective Optoelectronics Package Using Powder Metallurgy for FTTH Systems

As triple-service delivering voice, video, and data to customers is introduced into optical access network, the bidirectional or triple-directional data transmission is required. However, the bidirectional or triple-directional data transmissions of FTTH systems results in the increased cost of optoelectronics modules as shown in Fig. 4.1, which is contradictory to the low-cost market. In this chapter, powder metallurgy is proposed as a cost-effective method of fabricating metal parts in optoelectronic modules. The major advantage of powder metallurgy originates from the ability to shape metal powders into the final desired form. Therefore, employing MIM method not only reduces the number of metal parts but also greatly reduces the cost.

4.1 Introduction to Powder Metallurgy

4.1.1 Shaping Method

The conventional shaping of powder metallurgy is die compaction (DCP) performed by using both upper and lower punches which press metal powders into the die to form the desired form [1]. DCP method involves less production cost and high accuracy, but it also provides less shape complexity and less

mechanical properties. Metal injection molding (MIM) is a relatively new shaping method [2]. Metal powders are mixed with organic binders to form a fluid mass and injected under pressure into a die of the desired shape. The shaping metal powders are then heated to remove the binder and are eventually sintered. Owing to the use of fine metal powders of less than 20 μ m, the sintering shrinkages are large and final densities of more than 95% are attainable. In comparison with other shaping technologies, the MIM method overcomes the final density and shape limitations of the DCP method and the costs of conventional machining. The MIM method offers five features: low production cost, shape complexity, tight tolerance, applicability to several materials, and high mechanical properties. The box-type body and other parts of bidirectional optoelectronic modules can be replaced with one MIM SS316L housing due to shape complexity as shown in Fig. 4.1c. Therefore, employing MIM method not only reduces the number of metal parts but also greatly reduces the cost. However, the inherent porosity of MIM and DCP stainless steel cannot be avoided, and it has a great influence on defect formation of the welding joints such as cracks and hole formation resulting in degradation of stability and additional PWS [3].

4.1.2 Material Selection

The choice of materials has a great influence on the metallurgical compatibility of the metal with laser welding process. Stainless steel 304L (SS304L) and 316L (SS316L) with low carbon contents show good laser weldability. SS304L with Austenite texture offers good mechanical properties, corrosion/oxidation resistance, and relatively low-cost. SS316L, an improved

version of SS304L by the addition of molybdenum and a slightly high nickel content, provides better corrosion/creep resistance and higher mechanical strength, but the machining process of SS316L is more complicated than that of SS304L. One severe issue of material selection for the reliability of optoelectronic packages is the stress caused by thermal expansion, resulting in alignment changes after instant laser welding or long-term stress release. Therefore, metal housing materials with low coefficient of thermal expansion (CTE) are required. Kovar and Invar with very low CTE, $5.1 \times 10^{-6}/^{\circ}\text{C}$ and $1.5 \times 10^{-6}/^{\circ}\text{C}$, respectively, have been frequently used as the metal housing for box-type optoelectronic packages in high performance lightwave communication systems. The metal housings made of Invar and Kovar not only reduce stress and alignment changes after laser welding process but also provide better performance stability at varying ambient temperatures. In addition, Invar and Kovar used as the metal housings can minimize the fatigue stress and strain developed during thermal cycling associated with environment exposure and device operation.

However, only SS304L has been widely used as the metal housing for cylindrical-type optoelectronic packages due to easy machining. High nickel contents of SS316L, Kovar, and Invar increase the difficulty of machining, resulting in raising the machining cost. Thus, the metal housings made of SS316L, Kovar, and Invar, which show better laser welding performance, are only employed in high performance lightwave communication systems based on box-type optoelectronic packages, regardless of the cost issue. The advantages of applicability to several materials and the ability to shape metal powders into the final desired form from MIM method make it possible to employ SS316L, Kovar, and Invar as the metal housing used in low-cost

lightwave communication systems. In this study, DCP SS316L, MIM SS316L, and MIM Invar are selected as housing materials to investigate the laser weldability.

4.2 Laser Welding System and Experimental Setup

4.2.1 Laser Welding System

Figure 4.2 shows the setup of laser welding system used in this study. The system can be divided into three subsystems: alignment system, Nd:YAG laser system, and process controller system. The alignment system comprises four motion stages for four degrees of alignment (x , y , z , θ) between the laser diode and optical fiber. Upper and lower toolings are mounted on the x -/ y -/ θ -stages and z -stage, respectively. The Nd:YAG laser system consists of pulsed Nd:YAG laser, fiber optical beam-delivery system and, the charge-coupled device (CCD) monitor. The main beam from laser cavity is separated into three beams by three partial mirrors with different reflection to achieve beam balance of less than 3%. Three laser beams are delivered by three 600- μm step-index optical fibers and then focused on the workpiece with the focal spot size that is 400 μm in diameter. Each beam is precisely adjusted with an incident angle of $(45^\circ \pm 1^\circ)$ and positioned 120° apart to each other. The simultaneous and equal laser energy delivery is designed to reduce PWS between two welded parts because the solidification shrinkage of three welding spots can compensate each other, resulting in minimizing misalignment shift. To reduce the metal oxidation during laser welding, nitrogen gas is used as the shield on the molten metal. The process controller consists of main computer, alignment motion controller,

laser beam motion controller, LD driver, and optical power meter. Under such a setup, an automatic active alignment to achieve maximum optical coupling efficiency and a semiautomatic triggering of the laser on the accurate position of the metal joint are attained.

The pulsed laser welding parameters, such as laser power, pulse duration, and pulse energy, directly affect the joint quality and need to be carefully controlled to give repeatable joints in the laser welding process. The pulse energy E is approximately calculated by $E=P \times T$, where P and T are laser power and pulse duration, respectively. High laser power and high pulse energy cause hole formation, cracks, and metal injection [3]. In this study, laser power and pulse duration are controlled and selected as 0.6~1.6kWs and 2~6ms, respectively.

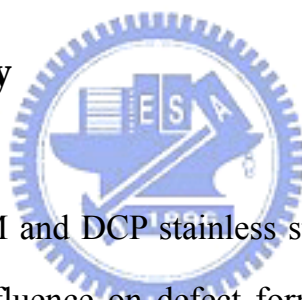


4.2.2 Laser Package Construction

For simplicity, the cylindrical-type laser module based on TO-Can laser diode and pigtail construction as shown in Fig. 4.2c is employed. The laser module can be divided into two main parts: a laser part and a pigtail fiber part, which are assembled by laser welding with a pressure of 5kgs [3] and a total of six welding spots to ensure a strong bonding. The laser part consists of a 1310nm TO-Can laser package with a built-in 1.5mm ball lens and a laser housing made of MIM steel, which is used to replace the box-type body of bidirectional or triple-directional optoelectronic modules as shown in Fig. 4.1c. MIM SS316L and MIM Invar are selected as the laser housing materials to investigate PWS, tracking error, and reliability. The TO-Can laser package is pressed into the laser housing by air-punch and then bonded with thermal epoxy.

The pressure-fix design with assistant thermal epoxy-bonding shows the advantage of the quick, easy and reliable assembly. The pigtail fiber part consists of a SS304L pigtail ferrule, including an angle-polished ceramics and a single mode fiber, and a pigtail housing made of SS304L fabricated by conventional machining. The pigtail ferrule and the pigtail housing are jointed by laser welding with a total of nine welding spots. To provide good contacts between two welded surfaces to ensure good joints without cracks caused by mismatch of two components, the accuracies of perpendicularity, parallelism, roughness, and flatness should be less than 50 μ m, 50 μ m, 0.1Ra (arithmetical mean roughness), and 10 μ m, respectively.

4.3 Laser Weldability



Inherent porosity of MIM and DCP stainless steels can not be avoided, and the porosity has a great influence on defect formation of the welding joints, such as cracks and hole formation resulting in degradation of stability and additional PWS. In this section, the laser weldability of MIM and DCP stainless steels, including welding defects, optimal welding conditions, PWS, and tracking error, is investigated

4.3.1 Microstructures of DCP and MIM Steel

The DCP and MIM processes include powder mixing, molding, debinding, sintering, and surface treatment. Figure 4.3 shows the microstructures of the final MIM SS316L, MIM Invar, and DCP SS316L with 97%, 96%, and 85% of the full density, respectively. The diameter of pores in MIM SS316L and MIM

Invar ranges from 2 to 5 μm , and the pores are discontinuous and isolated by the matrix. However, the sizes of the pores in DCP SS316L have wider distribution up to 10 μm , and the pores are continuous and cross-linked. These distinguishing types of pores have their respective effects on the defect mechanisms of laser welding joints, and this phenomenon will be discussed later.

4.3.2 Defect Formation of Laser Welding Spots in MIM SS316L and DCP SS316L

The laser welding process involves the pulsed laser energy focused on the small area, which absorbed by the jointed materials. Highly focused energy causes a welding pool on an extremely localized area and subsequently rapid cooling of the welding pool, and the associated material shrinkage may give rise to welding defects. To ensure long-term stability of welding joints, metallurgical analysis has been extensively used to investigate inner defects of the laser welding spots and joints, such as porosity and cracks. Metallurgical analysis also provides penetration depth and welding width of the laser welding spot. The procedures of metallurgical analysis include specimen sectioning, mounting, grinding, polishing, chemical etching, and microstructural examination.

The pulsed laser welding spots with an incident angle of 45° in MIM SS316L are shown in Fig. 4.4. Most of inherent pores in the melting pool of welding spots disappear, but another defects, holes, arise when laser power is more than 1.2kW with optical spot size of 400 μm . Among pulsed laser welding parameters, the laser power dominates hole formation. When the laser power P is 1.0kW and the pulse duration T ranges from 2 to 6ms, no hole formation is

observed. While the energy of the welding spot shown in Fig. 4.4(f) is more than that of the welding spot shown in Fig. 4.4(c) and Fig. 4.4(d), no hole is formed in Fig. 4.4(f). The welding spots with two pulses of laser give full support to above results. The power of the first pulsed laser is 1.0kW, when the defect-free welding spot is achieved, and that of the second pulsed laser is more than 1.2kW. The time between two pulses of laser is 5 s. Figure 4.5 indicates that the holes are observed and always occupy the tip of the welding pool where the first pulsed laser can not reach. This observation confirms that the laser power is one of the most important parameter to dominate the defect mechanism of the pulsed laser welding process. The possible cause of hole formation is that gas trapped in the inherent pores of MIM SS316L absorbs heat from molten steel to expand and subsequently nucleates and grows to form a hole in the welding spot. Because the laser beams have smooth Gaussian-like spatial extent in the cross section, the laser power is the maximum in the center of optical axis with an incident angle of 45° . Thus the holes always occupy in the optical axis and are symmetrically aligned along the optical axis.

Figure 4.6 shows the pulsed laser welding spots of DCP SS316L with continuous and cross-linked type of porosity. The hole formation can not be avoided even when the laser power is less than 1kW. More than one hole are observed and are found to be randomly situated in the welding pool. Besides, another defect, crack, is generated and is usually situated along the optical axis with an incident angle of 45° . The reason why the cracks occupy along optical axis is that the molten metal pool solidifies from the periphery toward the optical axis, and finally the crack is formed along the optical axis due to material shrinkage and high contents of inherent pores.

The penetration depth is measured in the direction of laser beam with

focused spot size 400 μ m as shown in Fig. 4.4(b). Figure 4.7(a) indicates the penetration depths of the welding spots in MIM SS316L as a function of the laser power and pulse duration. The penetration depth increases linearly with an increase in pulse duration at the fixed laser power and increases as the laser power increases at the fixed pulse duration. Figure 4.7(b) shows the penetration depth of the welding spots with different relative densities of SS316L, i.e., 100%, 97%, and 85%. The penetration depth increases as the relative density of specimen decreases.

4.3.3 Defect Formation of MIM SS316L and DCP SS316L Jointed with SS304

The cross sections of the welding joints, MIM SS316L jointed with full-density SS304L (MIM316L/304L), are shown in Fig. 4.8. Similar to what was observed in the welding spots of MIM SS316L, most of inherent pores disappear in the areas of welding joints, and the formation of holes is not observed as the laser power is below 1.0 kW. Thus, the defect-free welding joints of MIM steel can be achieved by using the laser power of less than 1.0kW. However, for DCP316L/SS304L joints, gas expanding of a serious nature gives rise to metal injection resulting in weak and unstable joints as shown in Fig. 4.9. In the welding spots of DCP SS316L, most of expanding gas can escape from the welding spot along the continuous porosity. As for DCP316L/304L joints, fully dense SS304L blocks the expanding gas out of the welding region and the gas pressure raises to inject the melting steel out of the welding joints, resulting in weak and unstable welding joints. Therefore, DCP steel with 85% relative density and continuous porosity can not be adopted as

the metal housing for the laser welding process.

4.3.4 Selection of Optimum Welding Conditions

The laser power is one of the most important parameters that dominate the defect mechanism of the laser welding process for optoelectronic packages. Besides, the welding geometries, such as lap joint, fillet joint and lap-fillet joint, greatly affect the joint strength and the stability of the welding spot. To ensure long-term reliability of welding joints, the strengths of lap, fillet, and lap-fillet joints are measured by a push test. MIM SS316L, MIM Invar, and 100% density SS316L are welded to SS304L as shown in Fig. 4.10. The strengths of MIM316L/304L joints with three joint geometries are summarized in Table I. Lap joints need additional laser power and energy to penetrate the upper metal part to joint with the lower metal part as shown in Fig. 4.10(b). In order to accomplish strong lap joint strength of more than 15kg, a laser power of 1.2kW at least is necessary. However, this creates the hole formation and results in more PWS. For fillet joints, less energy is required to achieve proper joint strength, but metal injection from upper metal parts reduces the welding strength and makes the joint unstable when the laser power exceeds 1.2kW. In addition, the fillet joints are prone to welding cracks along the interface between two welded parts. The lap-fillet joint, extracting advantages from lap joints and fillet joints, is the best choice for the welding joint. It provides high joint strength to laser power ratio without metal injection and welding cracks.

Figure 4.11 shows the strengths of MIM316L/304L, MIMInvar/304L, and 316L/304L joints by using lap-fillet joints as a function of the laser power and pulse duration. The joint strength increases linearly with laser power in

accordance with the penetration depth and decreases as density decreases. Although the penetration depth of MIM SS316L is larger than that of 100% density SS316L as shown in Fig. 4.7, the strength of MIM316L/304L joint is smaller than that of 316L/304L joint. The reason is that mechanical strength of 100% density SS316L is larger than that of MIM SS316L. The same reason explains why the strength of MIM316L/304L joint is larger than that of MIMInvar/304L joint. By optimizing welding parameters, the lap-fillet joint with laser power and pulse duration of 0.8kw and 3ms, respectively, is selected for the laser welding process. The lap-fillet joints without any defects are achieved, and the strengths of both MIM316L/304L and MIMInvar/304L joints are more than 15kgs, which ensures long-term reliability.

4.3.5 Post-Welding-Shift



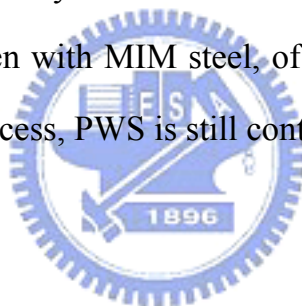
PWS is the misalignment between two welded parts after welding, and a few micrometers of the alignment shift can induce up to 50% coupling power loss. Therefore, a detailed understanding of PWS mechanism is the key to eliminating or minimizing the PWS-induced misalignment. The PWS mechanisms may be intrinsic and/or extrinsic. The intrinsic PWS is generated by rapid solidification of the welded region and the associated material shrinkage. In addition, the inherent porosity of MIM steel contributes additional PWS. Under optimal welding condition, elimination of inherent pores results in more shrinkage of the welded region, which gives rise to more coupling power loss. The shrinkage force is so great that no mechanical structure, such as the device gripper, can counteract the shrinkage shift [5]. The extrinsic PWS is resulted from laser parameters including laser power, laser

energy, and pulse duration, energy balance of laser beams, the incident angle of laser beams, joint geometry, welding positions, welding process, machining tolerance of components, roughness of two welded surfaces, and device gripper design of laser welding systems.

The misalignment due to the extrinsic PWS can be minimized or eliminated by optimizing welding condition, but the intrinsic PWS can not be avoided. Laser hammering (LH) is a well-known method to correct the intrinsic PWS by using additional laser welding spots to push the fiber back to maximum coupling position [5-6]. The LH process has already been proven to be effective to reduce PWS. However, the LH method increases the cycle time of laser welding process and create asymmetrical laser welding spots resulting in long-term reliability issue. Thus, how inherent porosity of MIM steel affects the intrinsic PWS is the key to determining the yield of the laser module manufacturing.

The magnitude of PWS is at the micrometer level. Hence, the direct measurement is very difficult. The PWS in this study is estimated with coupling power loss. Before welding, the laser and single mode fiber are precisely aligned to reach the maximum coupling power. After welding, solidification shrinkage of the welding pool gives rise to the transverse movement that results in coupling power loss. The coupling power loss and the associated transverse movement are used to determine PWS. Figure 4.12 shows the optical coupling profile of TO-Can laser packages with built-in 1.5mm ball lens. In order to investigate the intrinsic PWS, the laser welding conditions are optimized to minimize/eliminate the extrinsic PWS as mentioned in Section 4.2.1, 4.2.2, and 4.3.4. The lap-fillet joint with welding parameters of laser power and pulse duration of 0.8kw and 3ms, respectively, is chosen as the

welding geometry for the assembly of the laser part and the pigtail part. The SS304L ferrule and the pigtail housing made of SS304L are welded with the laser power and the pulse duration of 1.4kw and 2.5ms, respectively. Figure 4.13 shows the distribution of the coupling loss due to the PWS from 60 pieces of the welded laser modules with the laser housing made of MIM SS316L and MIM Invar. The MIM Invar material with low CTE can reduce the material shrinkage of the welded region and the associated intrinsic PWS. However, the results do not present this advantage clearly. The reason is that the PWS is small and influenced by various factors. Therefore, it is extremely difficult to identify the respective contribution of each factor. The coupling loss of over 95% of specimens in this study is less than 15%, which corresponds to the PWS of less than 2 μ m. Even with MIM steel, of which more PWS is induced during the laser welding process, PWS is still controlled to less than 2 μ m.



4.3.6 Tracking Error

The box-type optoelectronic packages, which are used in high performance lightwave communication systems, incorporate thermoelectric coolers and thermistors to maintain the laser diode operated at the optimum temperature so that laser operation can be obtained under extremes of ambient temperature. The optoelectronic packages for low-cost market, including the cylindrical-type packages, bidirectional packages, and triple-directional packages, are operated without temperature controller due to the cost-effective issue. The laser diode is mounted in the hermetic TO-Can package. The TO-Can package also contains a photodiode for monitoring and controlling the laser diode at the constant output power and extinction ratio as shown in Fig. 4.2(c). Using monitor photodiode

can compensate for the optical power deviation of the laser diode operated at different ambient temperatures, but it can not compensate the coupling power loss caused by the alignment change due to the CTE mismatch of individual parts in laser packages at various operating temperatures.

The front-to-rear tracking error is related to the alignment change due to laser packages operated at various ambient temperatures [7]. The rear-facet monitor photodiode is set to a constant which is corresponding to the associated output power at nominal operating temperature from the front facet of laser diode at the pigtail of the laser package. The front-to-rear tracking error is calculated by the equation below when varying the temperature:

$$\text{Tracking Error (dB)} = 10 \cdot \log \frac{Po(T)}{Po(25^{\circ}C)}$$

where $Po(25^{\circ}C)$ is the optical output power at $25^{\circ}C$, and $Po(T)$ is the optical output power at T . Tables II and III show the tracking error of the welded laser modules with the laser housing made of MIM SS316L and MIM Invar, respectively. Laser modules with low CTE MIM Invar materials present better performance of tracking error. This better performance of tracking error by using low CTE material is helpful to bidirectional and triple-directional optoelectronic packages. The bodies of bidirectional and triple-directional optoelectronic packages possess asymmetric shapes and are assembled with WDM filters, laser diode and photodiode with TO-Can packages, and other metal parts as shown in Fig.4.1(c). For cylindrical-type packages, symmetric thermal expansion and contraction can counteract the misalignment due to the CTE mismatch. However, the asymmetric shapes of bidirectional and triple-directional optoelectronic packages give rise to asymmetric thermal expansion and contraction, resulting in more tracking error. Using MIM Invar

with low CTE as construction material of asymmetric optoelectronic packages can minimize the tracking error which is an important issue for bidirectional and triple-directional optoelectronic packages.

4.4 Reliability Test

The reliable performance of the optoelectronic packages depends on the ability to maintain the optimum alignment position between the laser and the fiber in the operating environment. The reliability tests of the laser modules consist of 13 different tests grouped into mechanical (mechanical shock, vibration, thermal shock, solderability, and fiber pull), endurance (accelerated aging, high temperature storage, low temperature, temperature cycling, damp heat, and cyclic moisture resistance), and special tests (internal moisture, ESD threshold) based on Telcordia GR-468-CORE and MIL-STD-883E specifications [7]. To ensure long-term reliability, the laser modules are subjected to temperature cycling test, low temperature storage test, and high temperature storage test. Mechanical shock and vibration tests are selected to test the stability of the laser modules. Eleven laser modules with MIM SS316L and MIM Invar materials used for the laser housing, which are fabricated for investigating PWS and tracking error, are tested for each of test items.

1) Mechanical shock and vibration: The laser modules tested for mechanical shock are subjected to 5 shock pulses for each of orientations x, y, and z. The peak acceleration of the pulse is 1500g and pulse duration is 0.5ms. For vibration test, the entire frequency ranges from 20 to 2000Hz and returns to 20Hz and the cycle time is not less than 4min. This cycle is performed 4 times

for each of orientations x, y, and z. The pass/fail criterion of mechanical shock and vibration tests is 0.5dB maximum change in optical coupling power. Figures 4.14 and 4.15 indicate that all samples show the optical power variation of less than 0.5dB and are quite stable.

2) Temperature cycling: The temperature changes from -40°C to 85°C . The ramp rate is more than $10^{\circ}\text{C}/\text{min}$, and the dwell time for 85°C and -40°C is 10 min. The cycle time is within 40min. The pass/fail criterion is that the variations of optical coupling power are less than 0.5dB after 500 cycles. Figure 4.16 shows the variations of optical coupling power measured after 168, 500, 1000, and 1500 cycles. The results indicate the optical power deviations are still less than 0.5dB even after 1500 cycles. There are enough budgets for manufacturing tolerance.

3) High temperature and low temperature storage: The laser modules are tested at the maximum and minimum storage temperatures which are -40°C and 85°C , respectively. The pass/fail criterion is 0.5dB maximum change in optical coupling power after 2000hrs. Figures 4.17 and 4.18 show the variations of optical coupling power are less than 0.5dB after 2000hrs.

Under these tests, no laser module failures are observed. The reliability test data demonstrate that the laser modules using MIM steel as construction housing without any defects in the welding joints are stable and reliable.

References

- [1] Randall M. German, *Powder Metallurgy Science*, Princeton, N.J., U.S.A.: Metal Powder Industries Federation, 1984.
- [2] Randall M. German, and A. Bose, *Injection molding of metals and ceramics*,

- Princeton, N.J., U.S.A.: Metal Powder Industries Federation, 1997.
- [3] W. H. Cheng, W. H. Wang, and J. C. Chen, "Defect Formation Mechanisms in Laser Welding Techniques for Semiconductor Laser Packaging," *IEEE Tran. Comp., Hybrids, Manufact. Technol. B*, vol. 20, no. 4, pp. 396-402, Nov. 1997.
- [4] M. K. Song, S. G. Kang, N. Hwang, H. T. Lee, S. S. Park, and K. E. Pyun, "Laser Weldability Analysis of High-speed Optical Transmission Device Packaging," *IEEE Tran. Comp., Packag., Manufact. Technol. A*, vol. 19, no. 4, pp. 758-763, Nov. 1996.
- [5] B. Valk, R. Battig, and O. Anthamatten, "Laser Welding for Fiber Pigtailling with Long-term Stability and Submicron Accuracy," *Opt. Eng.*, vol. 34, no. 9, pp. 2675-2682, 1995.
- [6] Y. C. Hsu, Y. C. Tsai, Y. L. Ho, M. T. Sheen, J. H. Kuang, and W. H. Cheng, "A Novel Alignment Shift Measurement and Correction Technique in Laser-Welded Laser Module Packaging," *J. Lightwave Technol.*, vol. 23, no. 2, pp. 486-494, Feb. 2005.
- [7] "Generic reliability assurance requirements for optoelectronic device used in telecommunications system," Bellcore, GR-468-CORE, Dec. 1998.

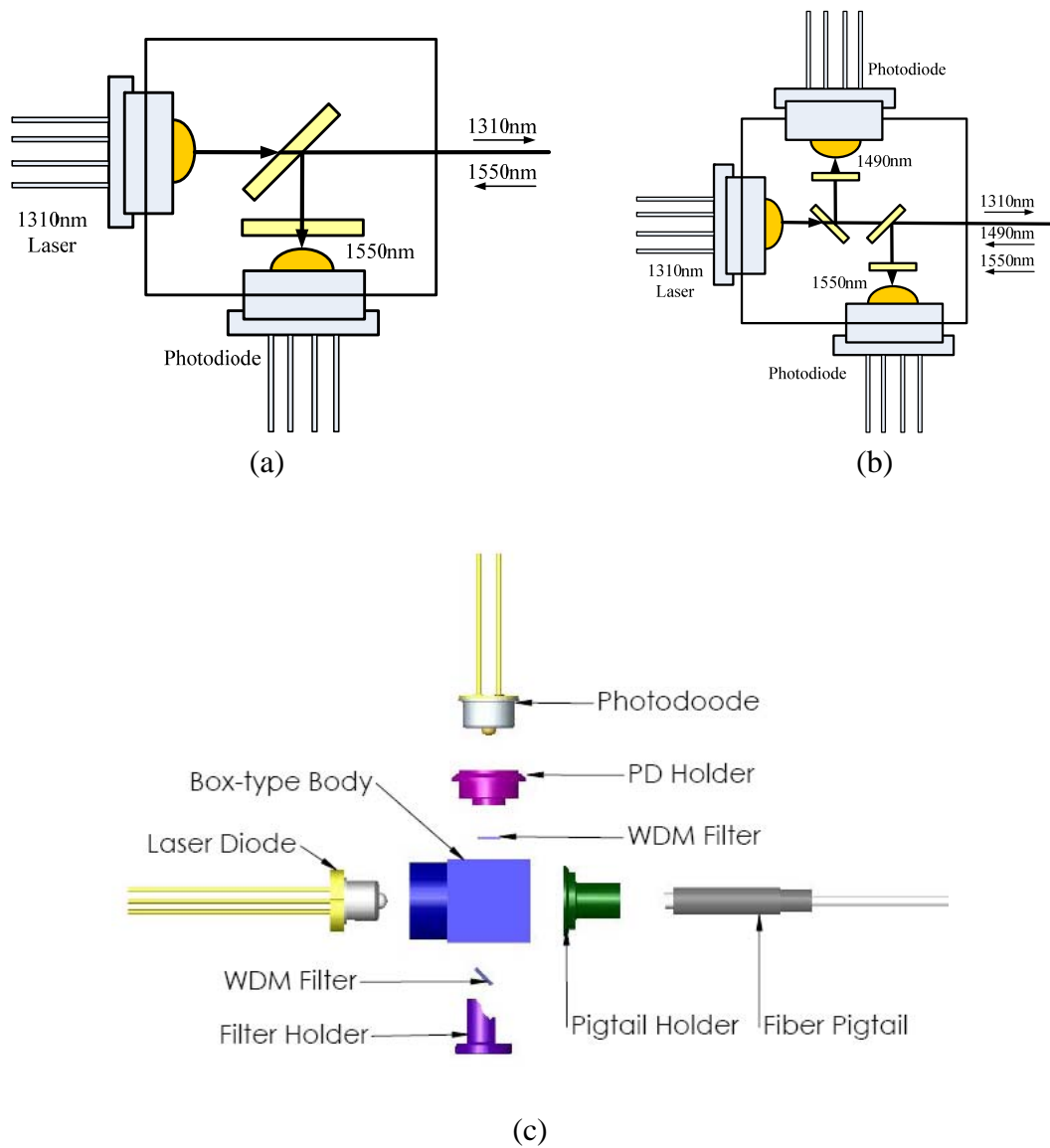


Fig. 4.1 (a) Illustration of bidirectional optoelectronic package. (b) Illustration of triple-directional optoelectronic package. (c) The components of bidirectional optoelectronic package.

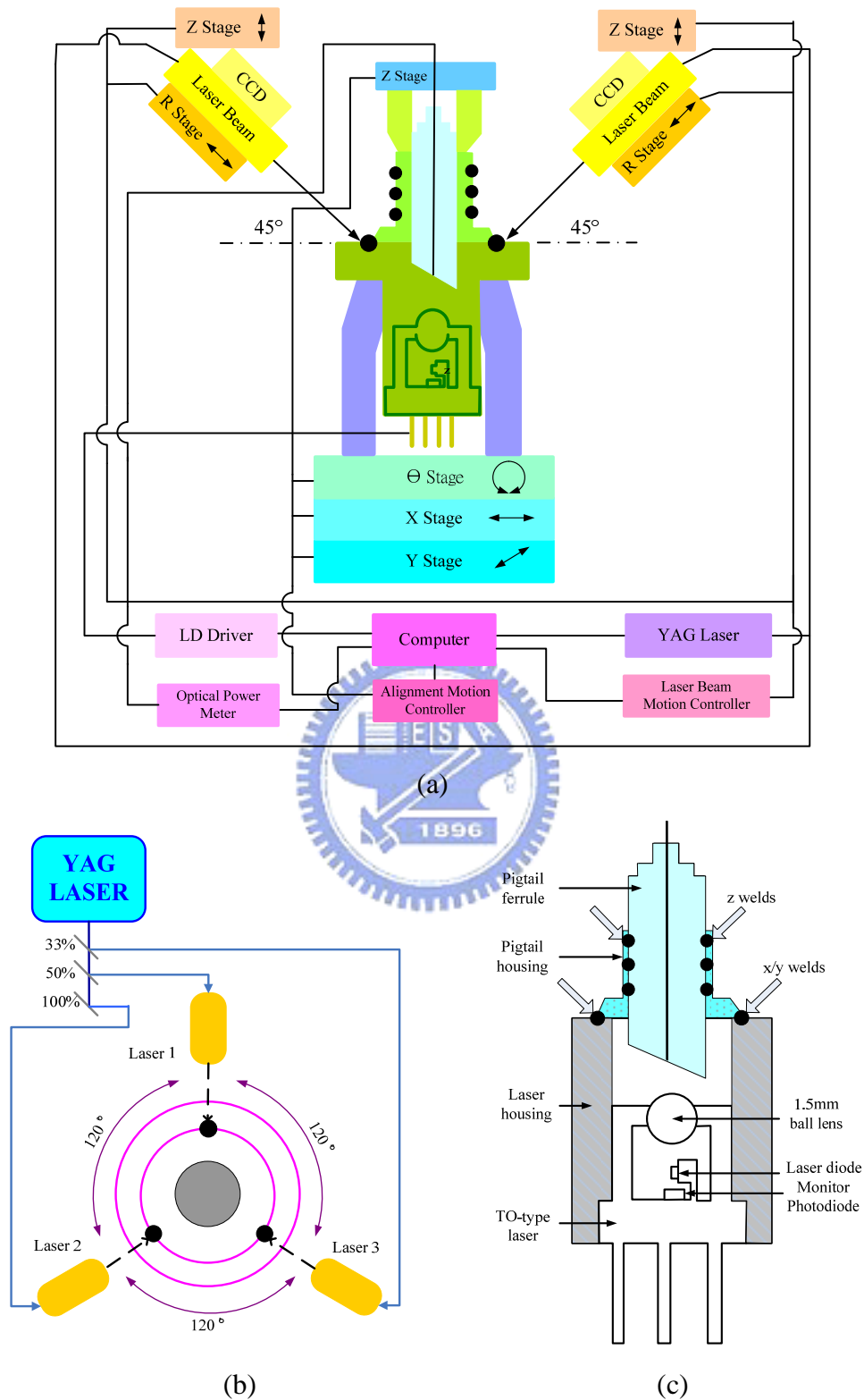


Fig. 4.2 (a),(b) Schematic diagram of the laser welding system. (c) Configuration of the cylindrical-type laser module. Arrows indicate the welding spots.

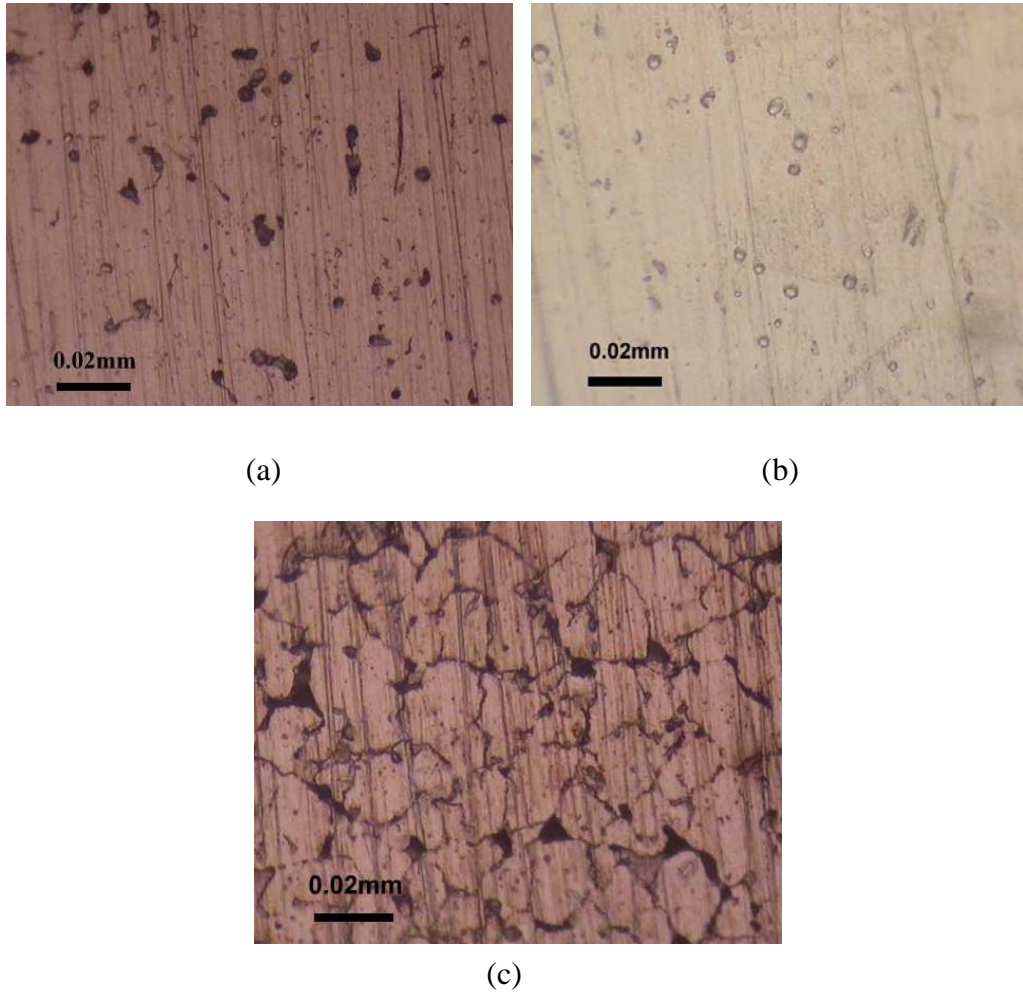


Fig. 4.3 Microstructures of MIM 316L, DCP SS316L, and MIM Invar. (a) MIM SS316L with 97% of full density (b) MIM Invar with 96% of full density (c) DCP SS316L with 85% of full density

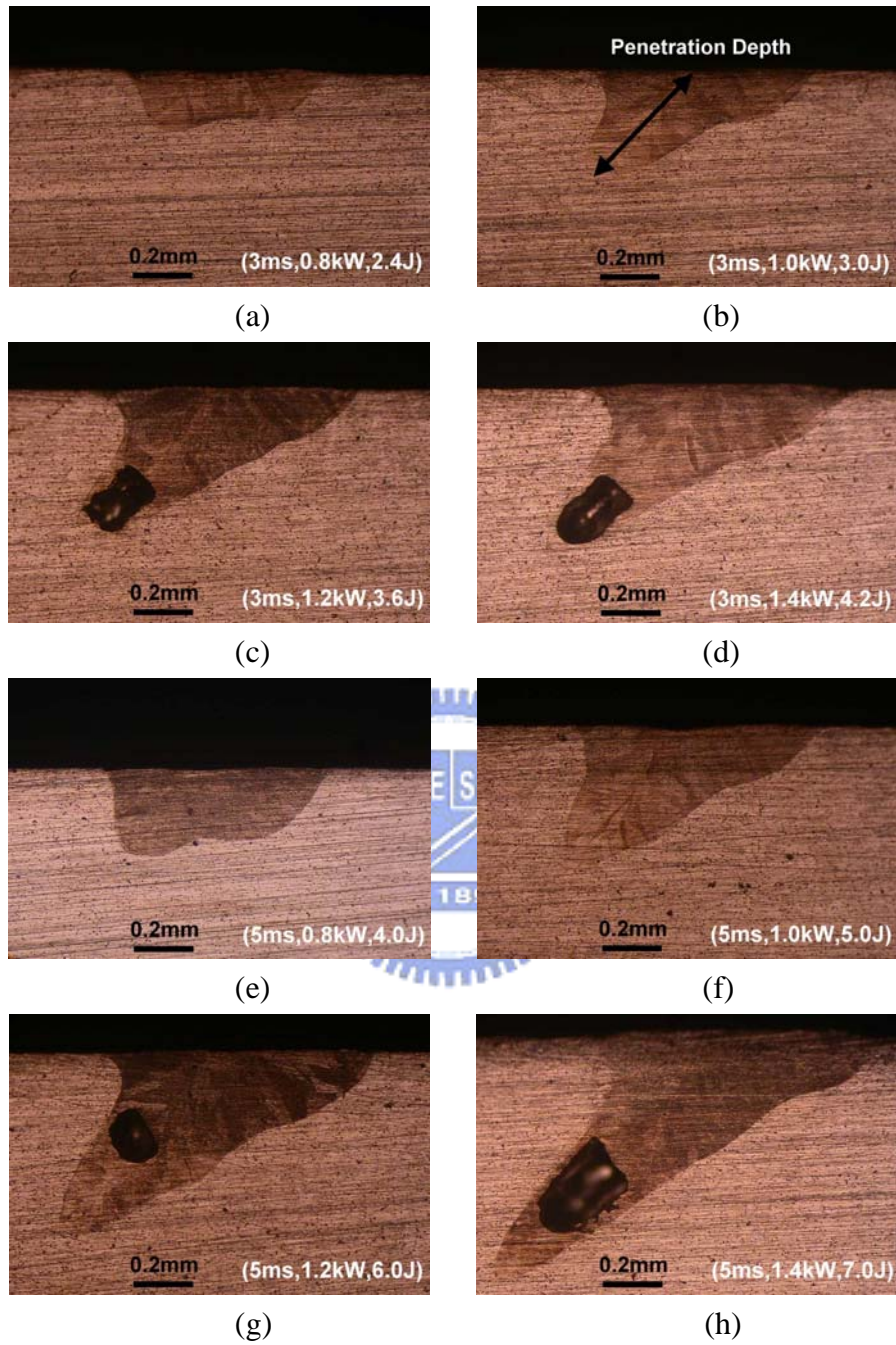


Fig. 4.4 Cross sections of the welding spots in the MIM SS316L with various welding conditions. Data in parentheses are pulse duration (millisecond), power (kilowatt), and laser energy (joule).

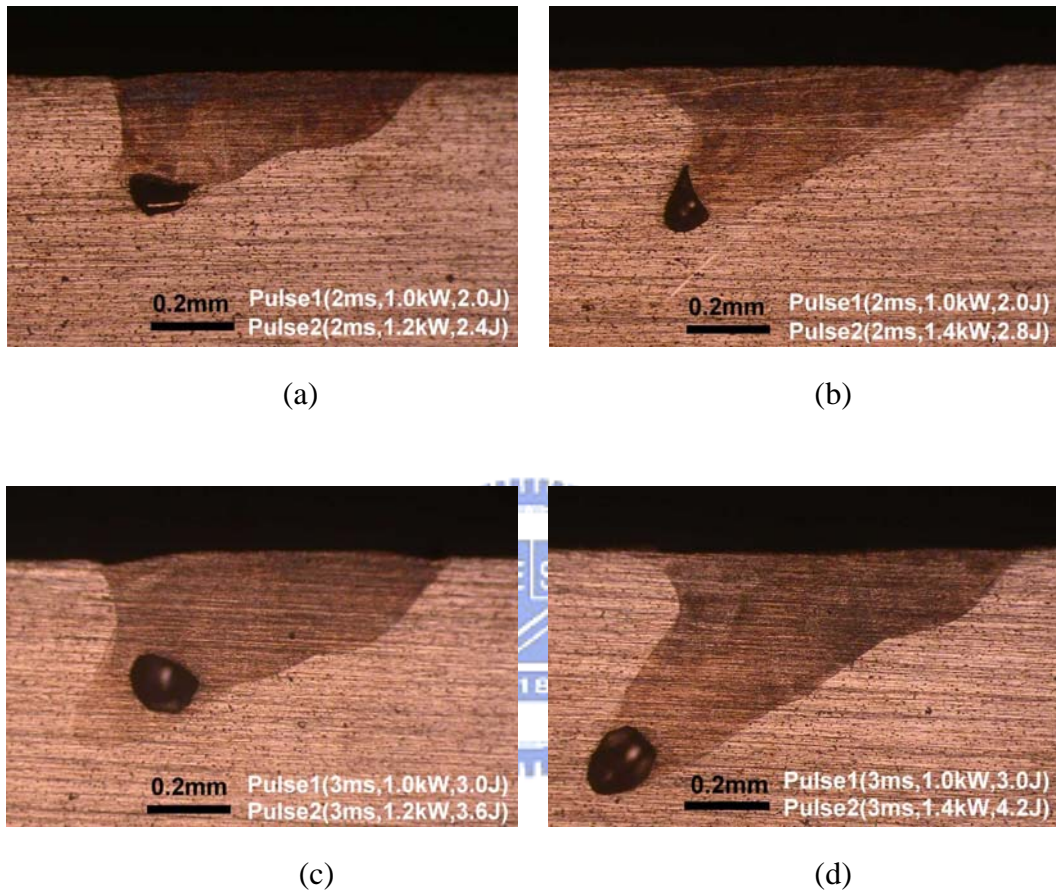


Fig. 4.5 Cross sections of the welding spots with two pulses of laser in the MIM SS316L. Data in parentheses are pulse duration (millisecond), power (kilowatt), and laser energy (joule).

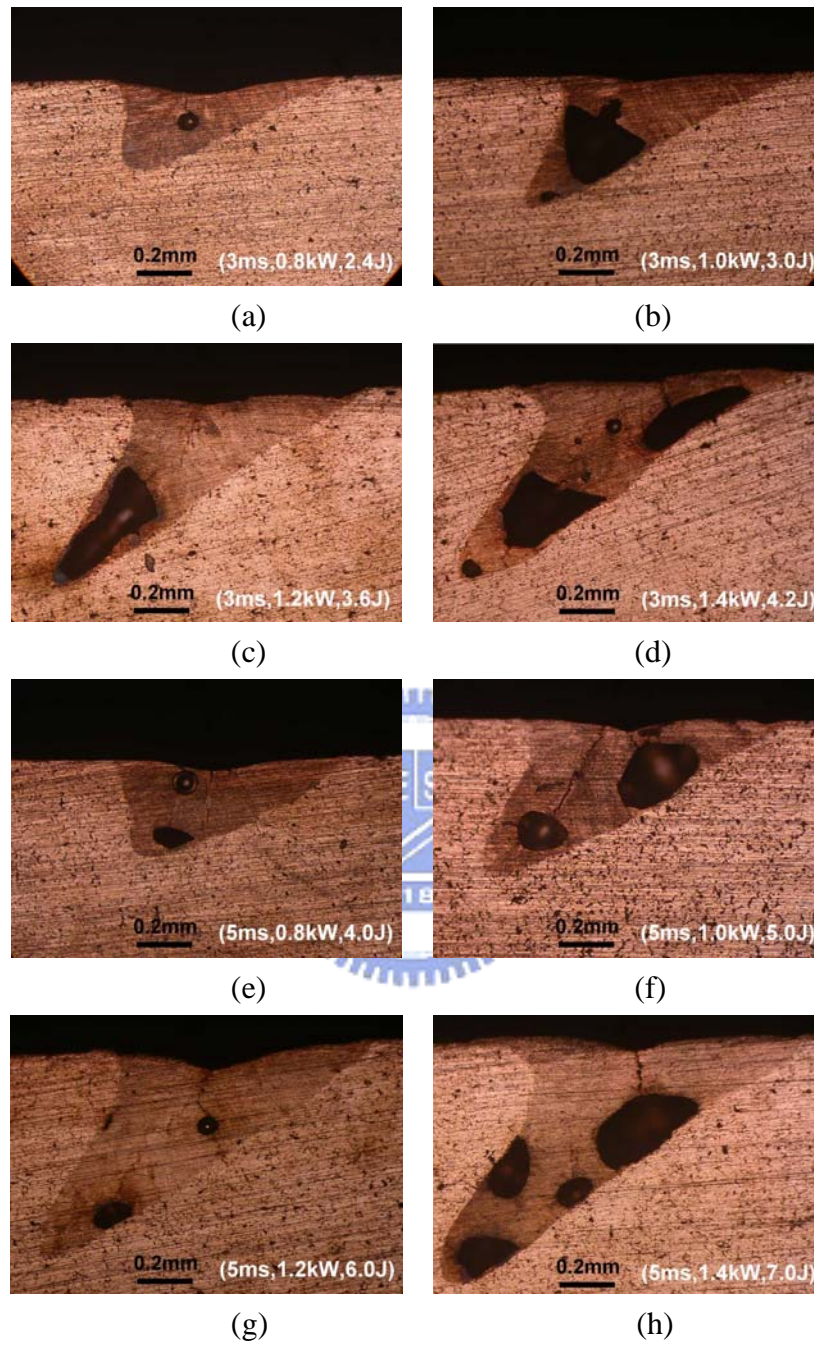
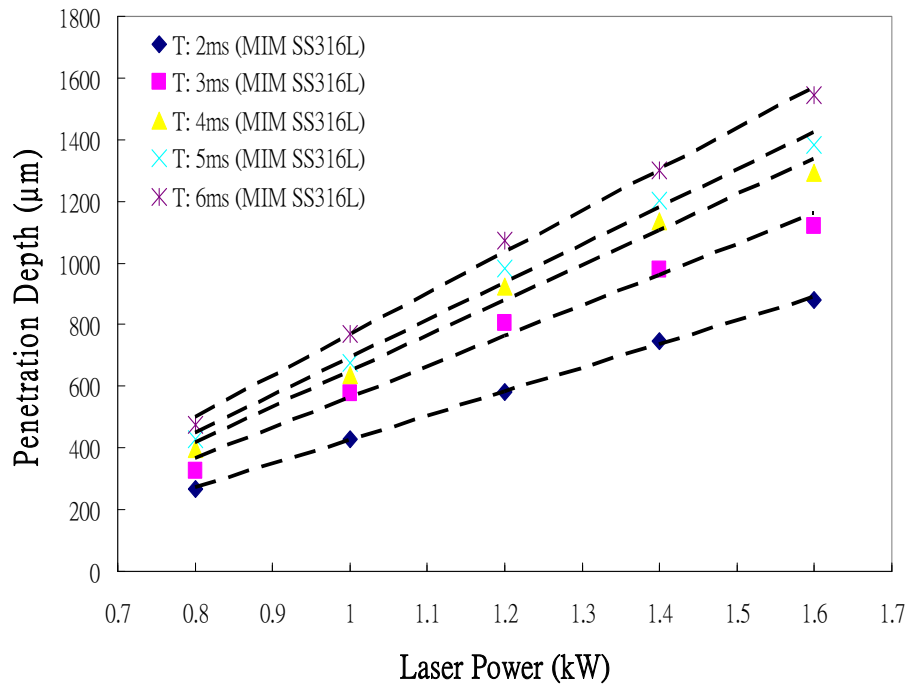
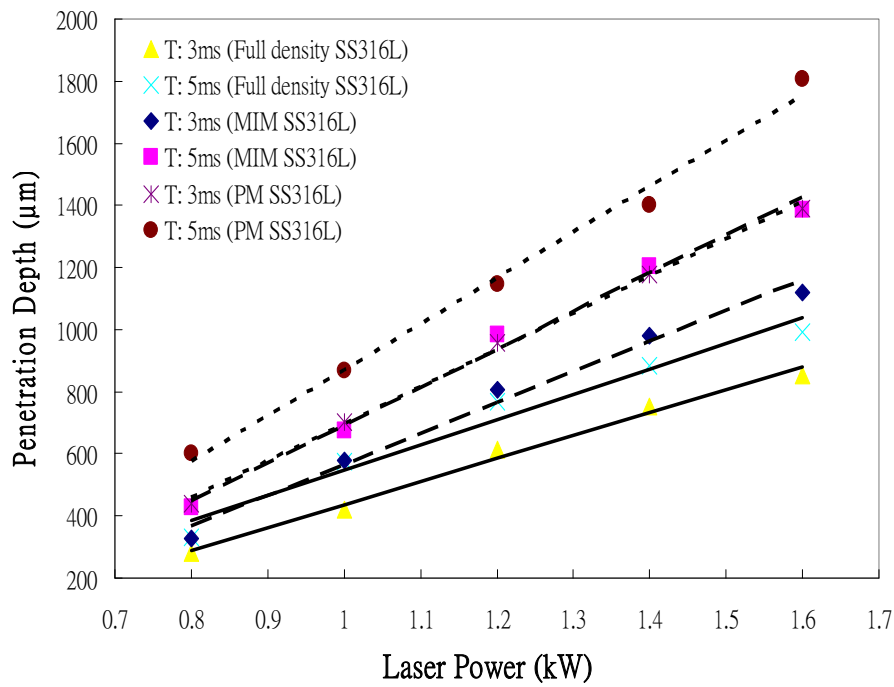


Fig. 4.6 Cross sections of the welding spots in the DCP SS316L with various welding conditions. Data in parentheses are pulse duration (millisecond), power (kilowatt), and laser energy (joule).



(a)



(b)

Fig. 4.7 Penetration depth of welding spots as a function of laser power with various pulse durations T. (a) MIM SS316L (b) Full density SS316L, MIM SS316, and DCP SS316L

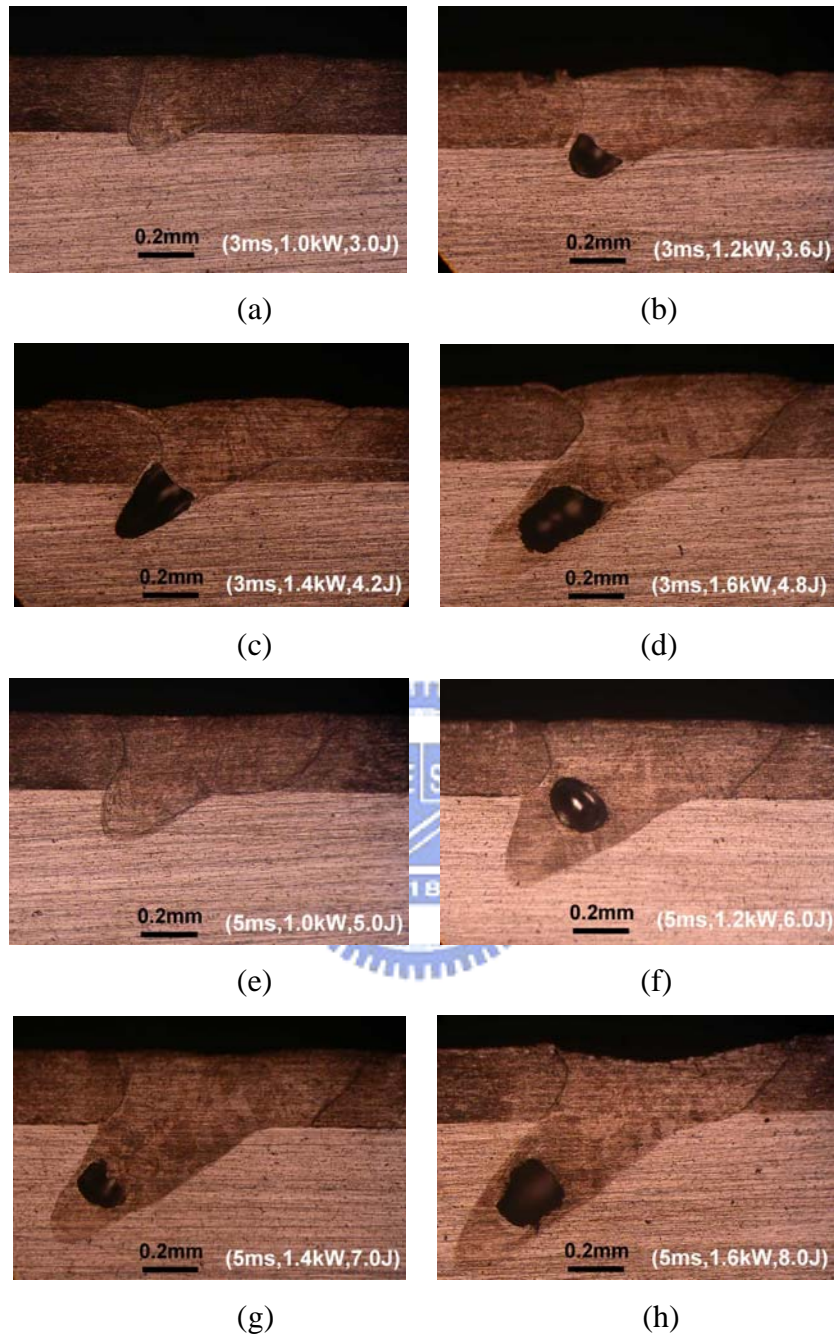


Fig. 4.8 Welding joints of MIM SS316L (bottom) and SS304L (top). Data in parentheses are pulse duration (millisecond), power (kilowatt), and laser energy (joule).

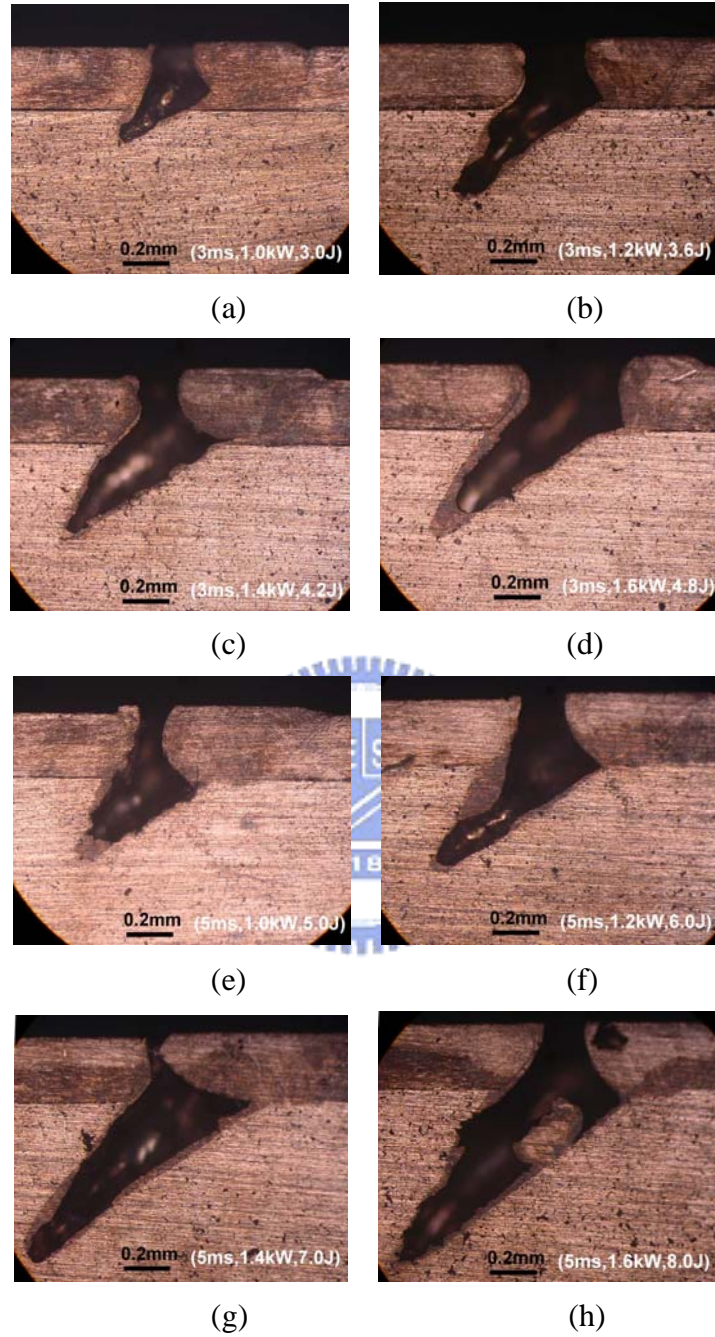


Fig. 4.9 Welding joints of DCP SS316L (bottom) and SS304L (top). Data in the bracket () are pulse duration (ms), power (kW), and laser energy (J).

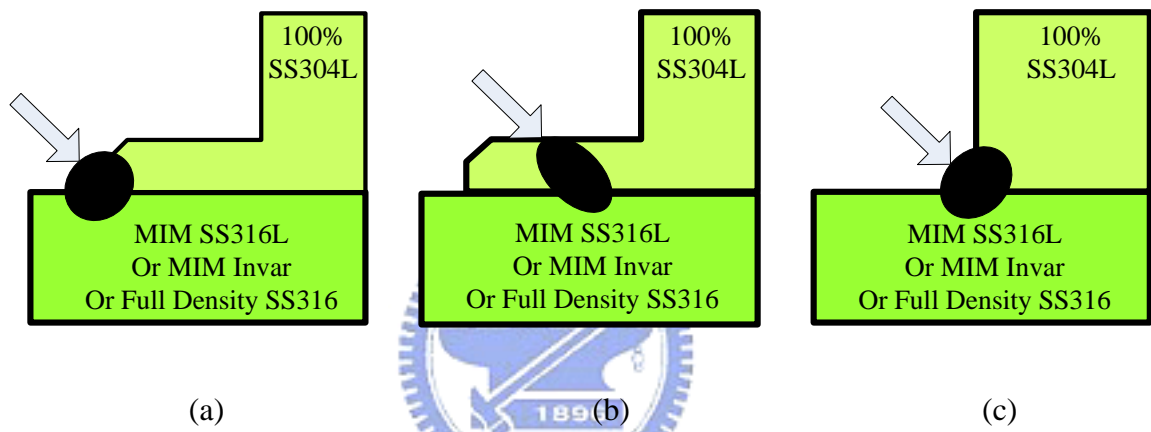


Fig. 4.10 Schematic joint geometries for laser welding (a) Lap-fillet joint, (b) Lap joint, and (c) Fillet joint. Arrow indicates the welding spot.

Table I Joint strengths (kg) of lap joint, fillet joint, and lap-fillet joint with various welding parameters. The deviation of joint strength is less than 10%.

Pulse Duration Laser Power	Lap Joint					Fillet joint					Lap-fillet Joint				
	2ms	3ms	4ms	5ms	6ms	2ms	3ms	4ms	5ms	6ms	2ms	3ms	4ms	5ms	6ms
0.6kw	NJ*	NJ	NJ	NJ	NJ	6.08	11.2	15.1	18.3	22.7	11.3	16.3	20.5	24.5	27.8
0.8kw	NJ	NJ	NJ	NJ	2.1	10.5	15.9	20.3	24.8	27.7	13	21.3	25.5	29.5	32.5
1.0kw	NJ	3.1	7.7	13.7	17.8	13.8	18.8	22.2	27.5	31	16.8	25.4	30.5	36	39.4
1.2kw	0.9	12.3	18.2	23.7	29.7	MI [#]	MI	MI	MI	MI	20.6	28.5	35.6	39.9	43.3
1.4kw	5.9	15.0	23.0	30.3	37.4	MI	MI	MI	MI	MI	23.7	32.9	39.7	45.1	49.3
1.6kw	10.8	21.2	28.6	38.9	47.9	MI	MI	MI	MI	MI	MI	MI	MI	MI	MI

* No joint is formed. # Unstable joint caused by metal injection.

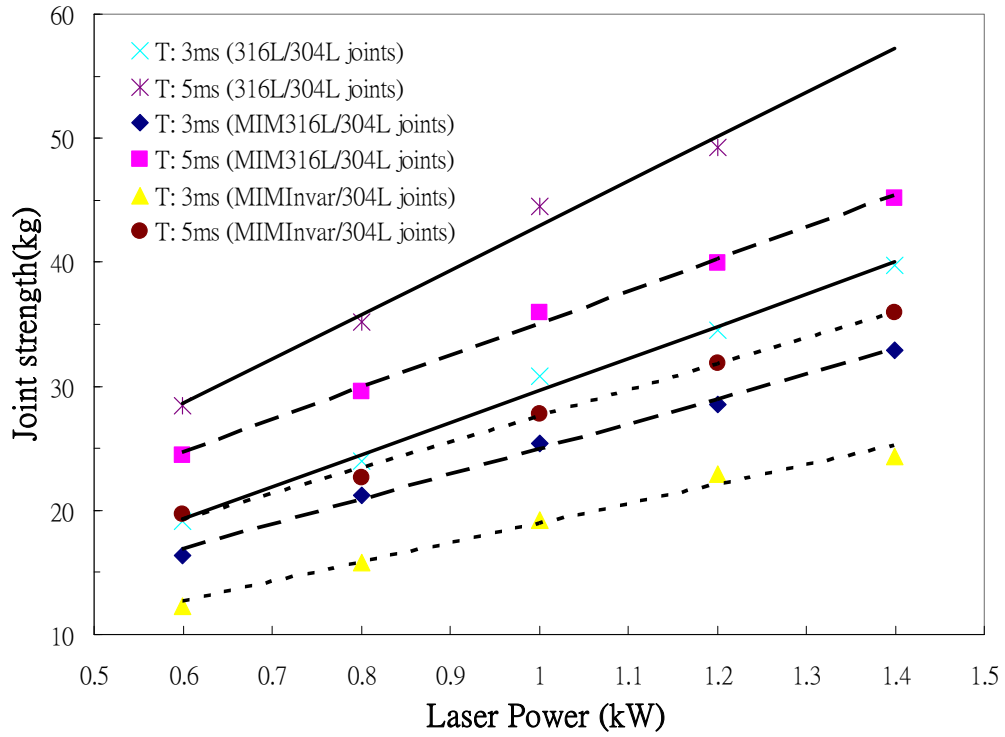


Fig. 4.11 Strengths of 316L/304L, MIM316L/304L, and MIMInvar/304L joints as a function of laser power with various pulse durations T.

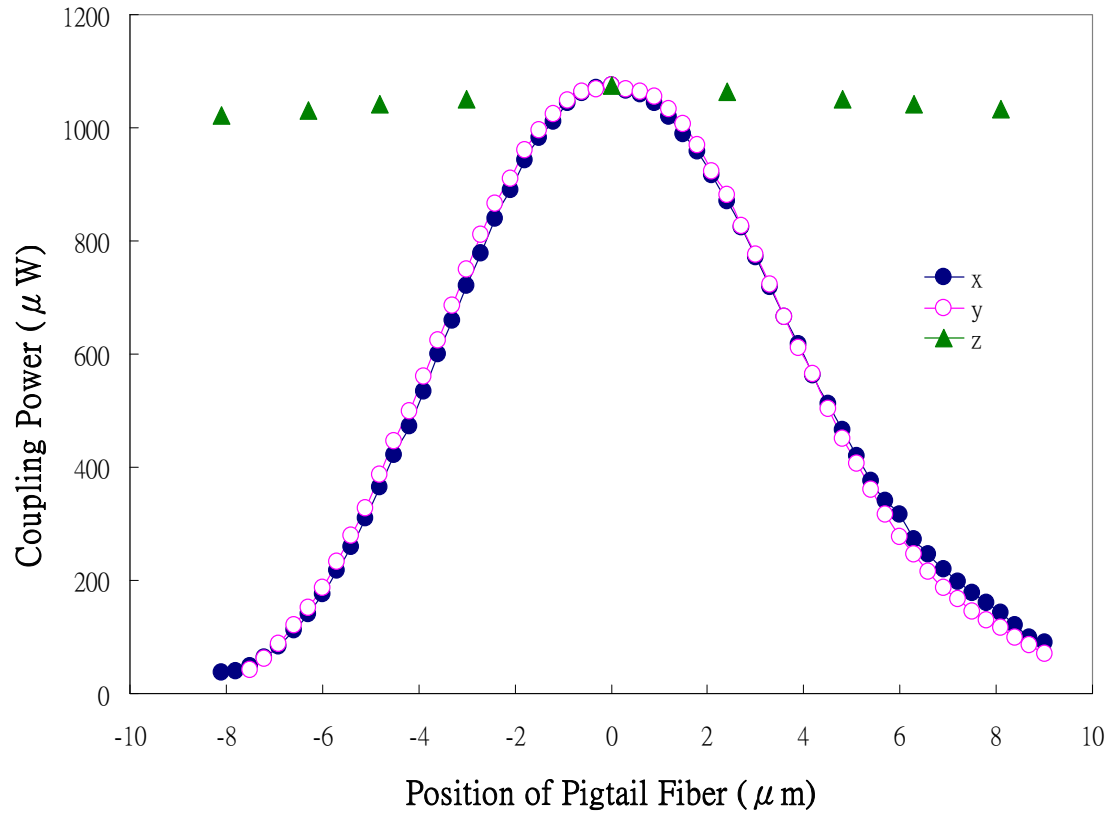
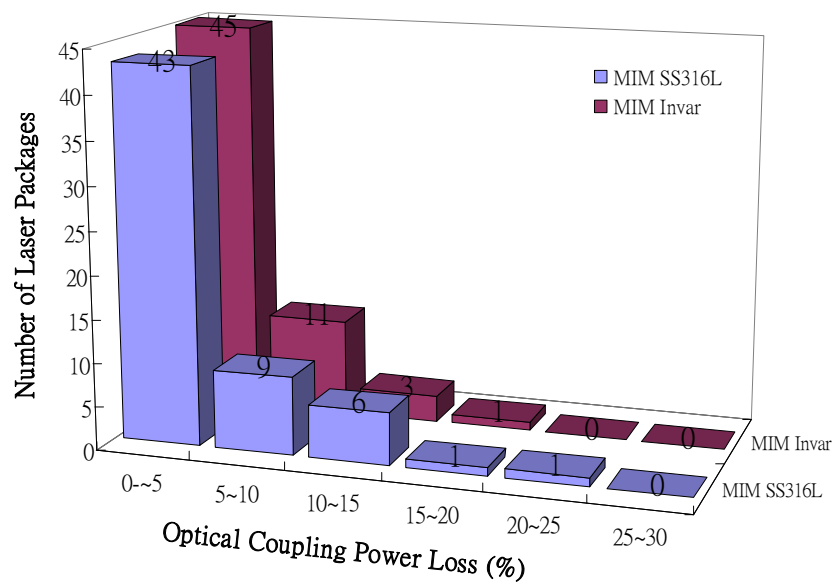
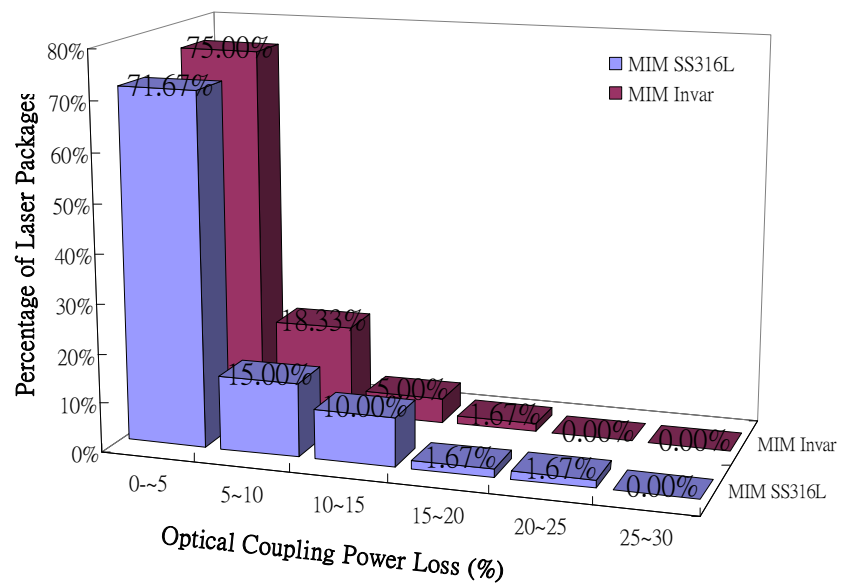


Fig. 4.12 Coupling power as a function of x , y , and z orientations.



(a)



(b)

Fig. 4.13 Distribution of the coupling power loss due to PWS.

Table II Tracking error (dB) of the laser modules with MIM SS316L material
as the laser housing

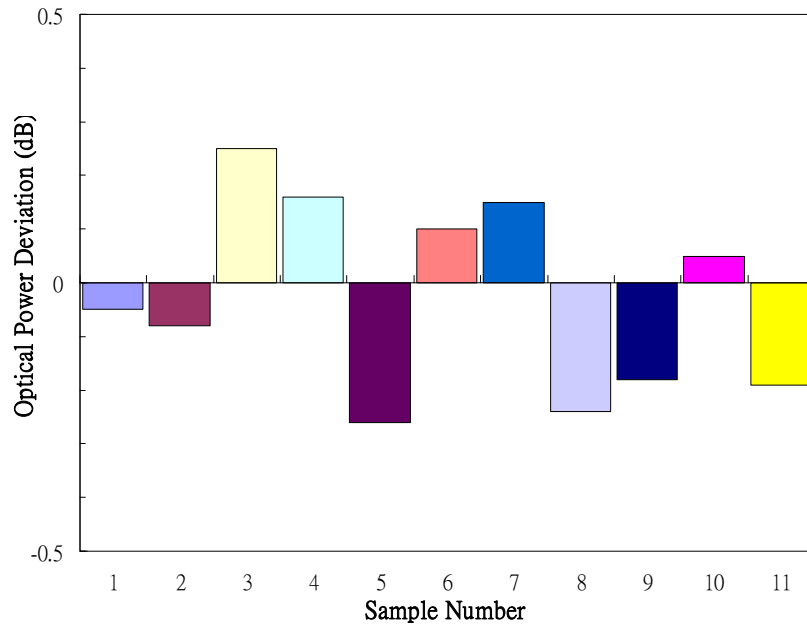
Temperature	Module Number								Average Deviation*
	1	2	3	4	5	6	7	8	
-40°C	-0.415	-0.424	-0.160	-0.427	-0.015	-0.285	-0.349	-0.256	0.292
0°C	-0.230	-0.285	-0.063	-0.236	0.112	-0.225	-0.196	-0.148	0.187
25°C	0.000	0.000	0.000	0.000	0.000	0.000	0.000	0.000	0.000
70°C	0.257	0.224	0.228	0.343	-0.327	-0.116	0.259	-0.268	0.253
85°C	0.306	0.311	0.272	0.366	-0.578	-0.243	0.305	-0.356	0.342
Maximum Deviation#	0.721	0.735	0.433	0.793	0.691	0.285	0.654	0.356	

* Average Deviation = $\frac{\sum | \text{Tracking Error}(T) |}{N(T)}$, N: number of laser module, T:
temperature

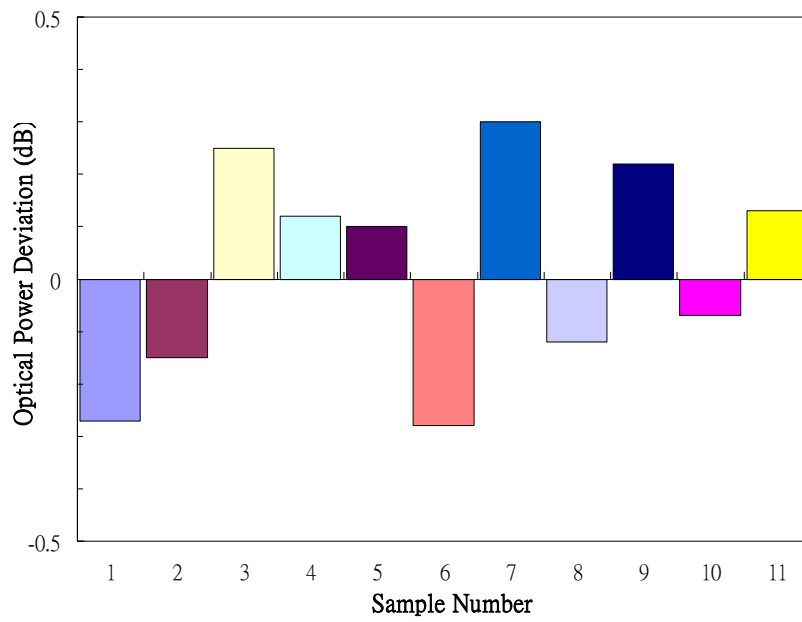
Maximum Deviation= Max(Tracking Error)-Min(Tracking Error)

Table III Tracking error (dB) of the laser modules with MIM Invar material as the laser housing

Temperature	Module Number								Average Deviation
	1	2	3	4	5	6	7	8	
-40°C	-0.222	-0.286	0.035	-0.273	0.236	-0.073	0.121	-0.319	0.196
0°C	0.042	-0.152	0.085	-0.144	0.106	-0.024	0.103	-0.248	0.113
25°C	0.000	0.000	0.000	0.000	0.000	0.000	0.000	0.000	0.000
70°C	0.115	0.084	-0.079	-0.152	0.112	-0.114	0.187	-0.198	0.130
85°C	0.171	0.134	-0.113	-0.181	0.271	-0.179	0.222	-0.257	0.191
Maximum Deviation	0.394	0.419	0.198	0.273	0.271	0.179	0.222	0.319	

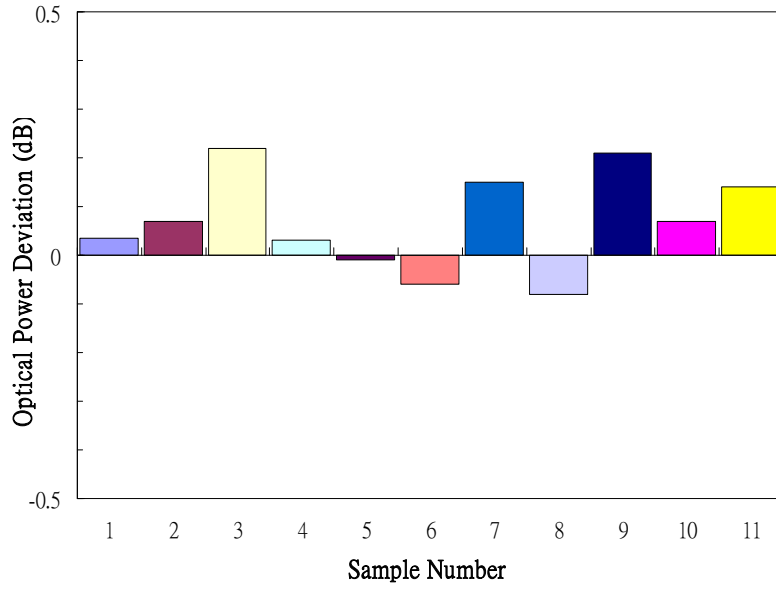


(a)

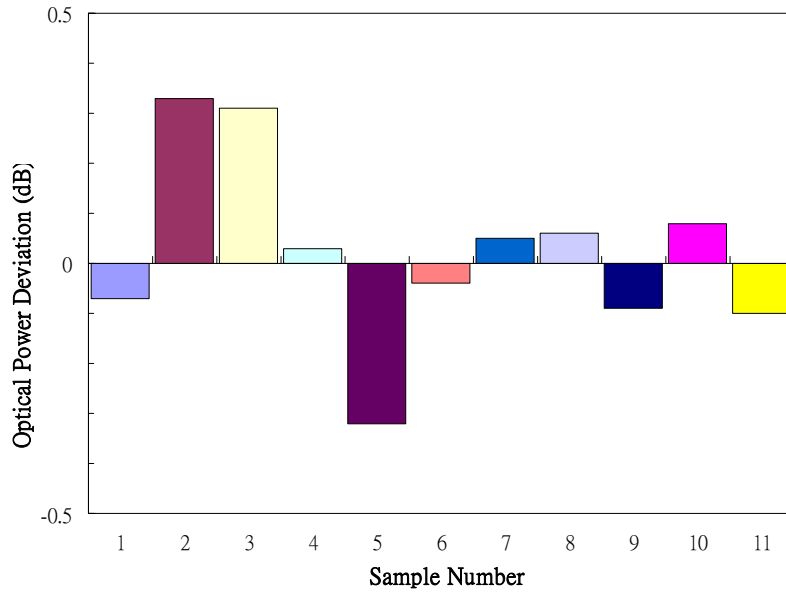


(b)

Fig. 4.14 Optical power deviation after mechanical shock test. The laser modules are subject to 5 shock pulses for each of orientations x, y, and z. The peak acceleration of the pulse is 1500g and pulse duration is 0.5ms. The pass/fail criterion is 0.5dB maximum change in optical coupling power. (a) MIM SS316L. (b) MIM Invar

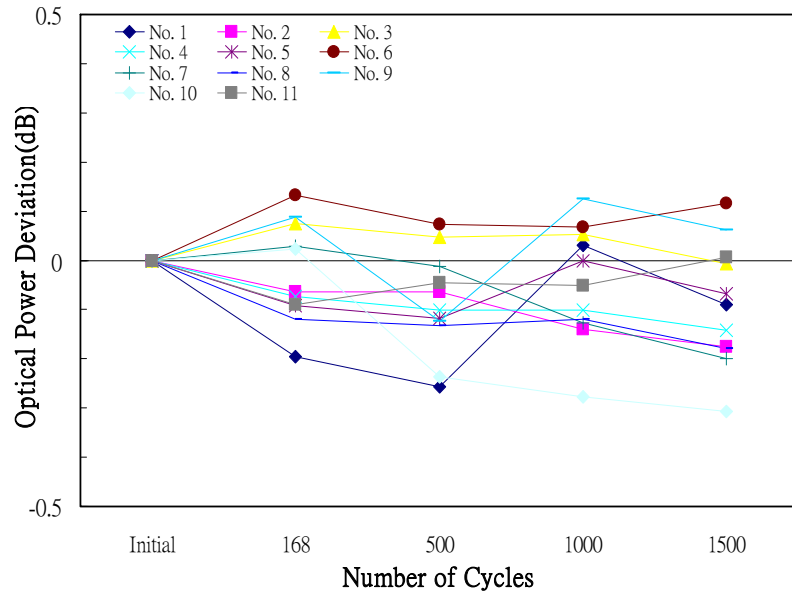


(a)

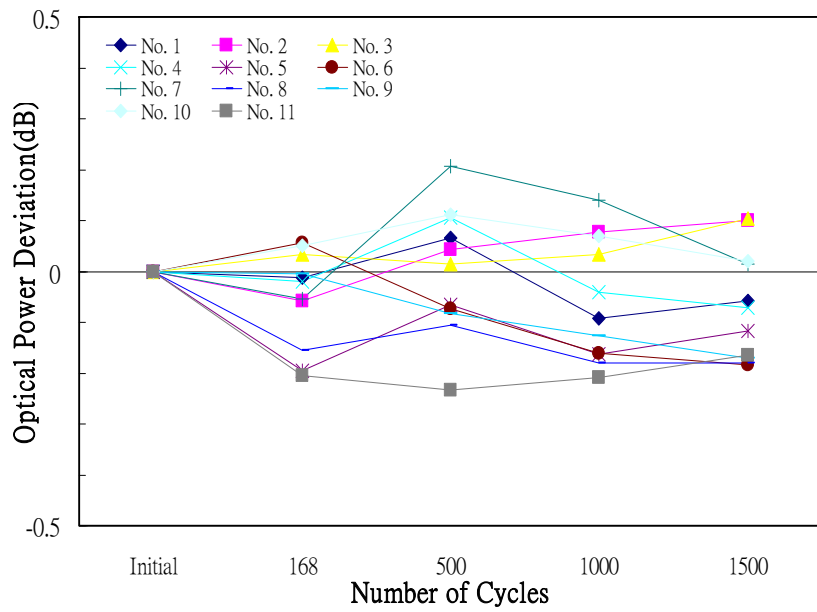


(b)

Fig. 4.15 Optical power deviation after vibration test. The frequency ranges from 20 to 2000Hz and return to 20Hz, and the cycle time is not less than 4min. This cycle is performed 4 times for each of orientations x, y, and z. The pass/fail criterion is 0.5dB maximum change in optical coupling power. (a) MIM SS316L. (b) MIM Invar.



(a)

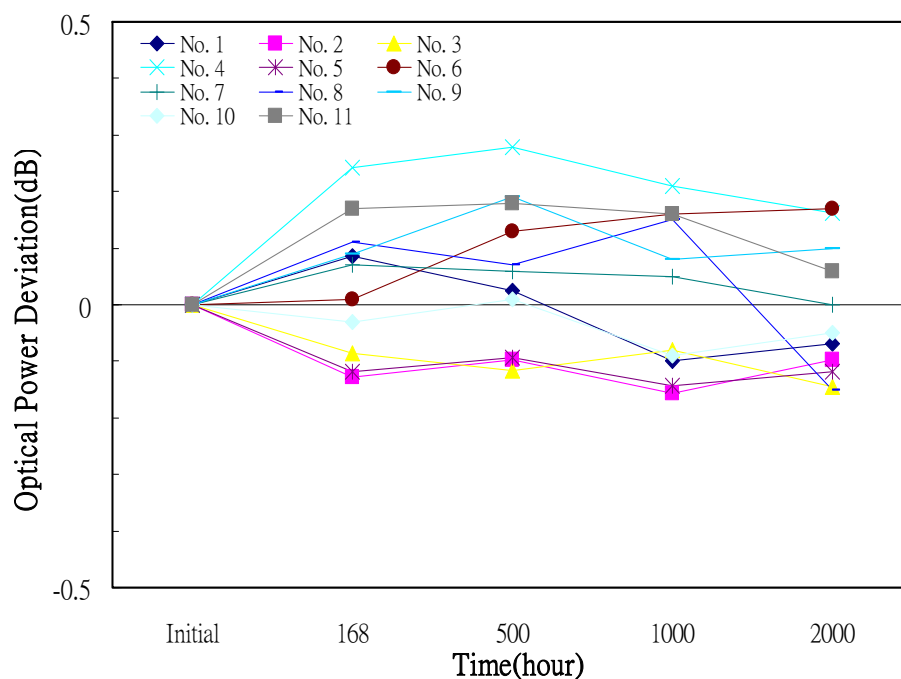


(b)

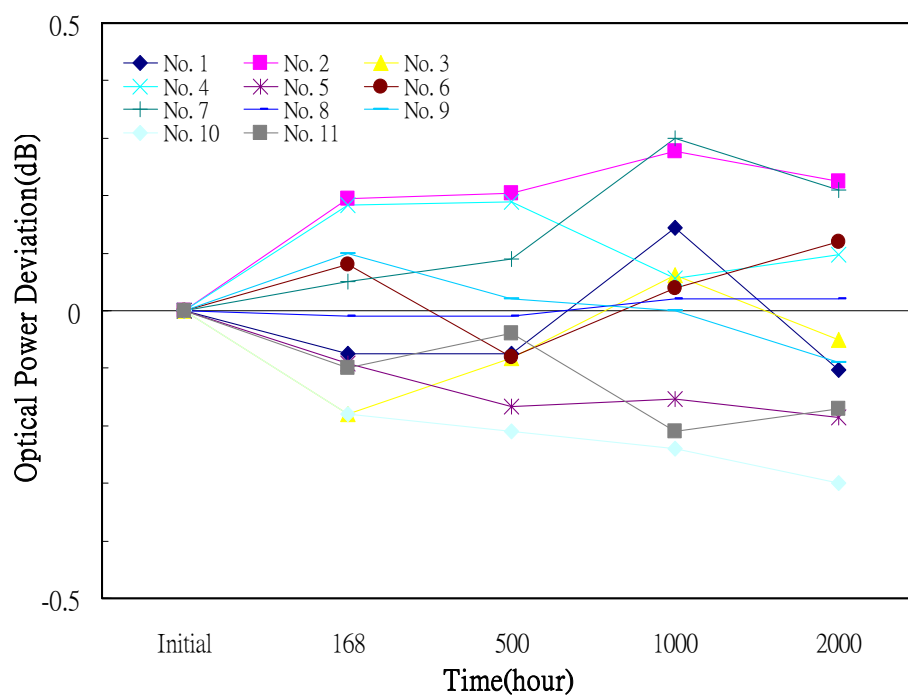
Fig. 4.16 Optical power deviation with numbers of temperature cycling test.

The temperature changes from -40°C to 85°C . The ramp rate is more than $10^{\circ}\text{C}/\text{min}$ and the dwell time is 10 min at 85°C and -40°C . The cycle time is within 40min. The pass/fail criterion is 0.5dB maximum change in optical coupling power after 500 cycles. (a) MIM SS316L.

(b) MIM Invar



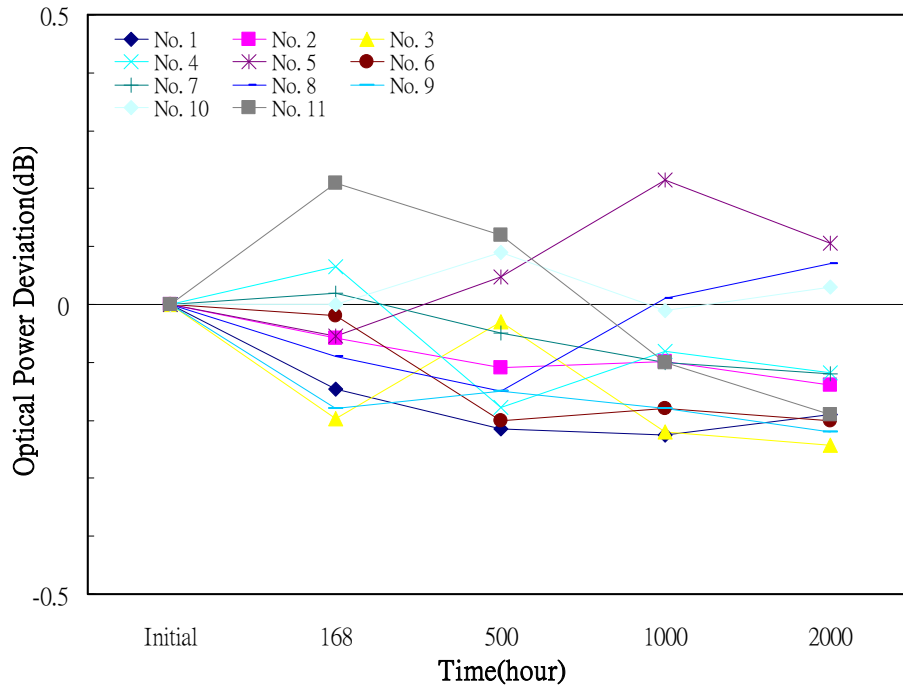
(a)



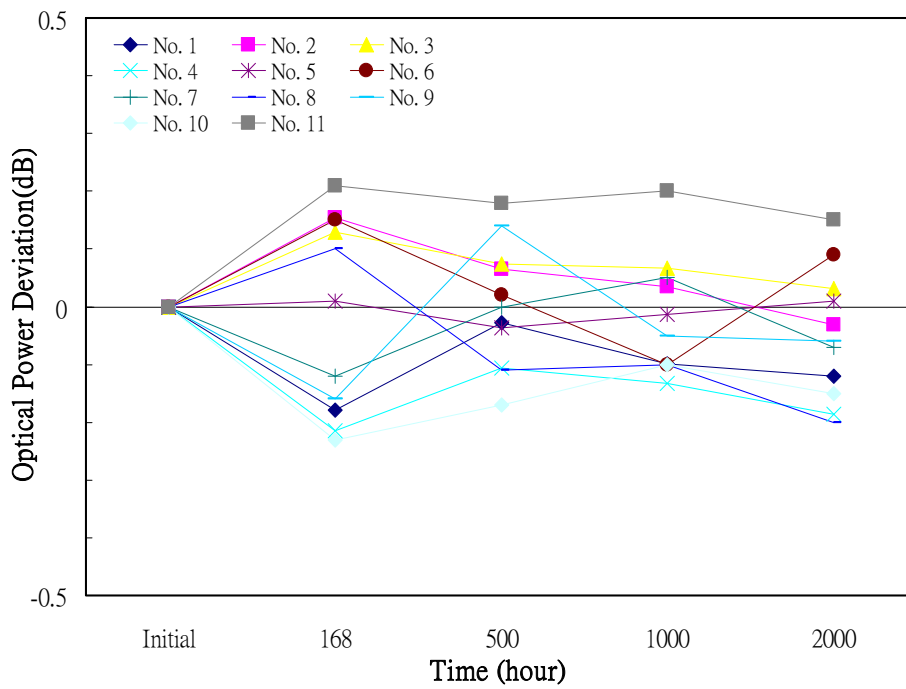
(b)

Fig. 4.17 Optical power deviation with time of high temperature storage test.

The laser modules are tested at 85°C. The pass/fail criterion is 0.5dB maximum change in optical coupling power after 2000hrs. (a) MIM SS316L. (b) MIM Invar.



(a)



(b)

Fig. 4.18 Optical power deviation with time of low temperature storage test.

The laser modules are tested at -40°C . The pass/fail criterion is 0.5dB maximum change in optical coupling power after 2000hrs. (a) MIM SS316L. (b) MIM Invar.

Chapter 5

Conclusions

5.1 Summary for the Dissertation

In previous chapters, the applications of microwave photonics and optoelectronic package in multi-services access networks have been explored. The optical-wireless network offering both broadband wireless and wired services and the hybrid access network integrating RoF and FTTH systems have been investigated and studied. In addition, powder metallurgy has been demonstrated to be a promising candidate as a cost-effective method of fabricating metal parts to reduce the cost of triple-directional optoelectronic modules for FTTH systems which can deliver data, voice, and video to the customers simultaneously. These investigations and demonstrations will be useful in the fields of optical multi-services access networks. The important results and contributions achieved in this dissertation are briefly summarized below.

5.1.1 Theoretically Analysis of Mm-wave Generation Using DSBCS modulation

The impact of the inherent MZM nonlinearity on mm-wave signals has been theoretically investigated. Due to fabrication tolerances, the MZM has unequal

splitting ratio of the Y-splitter, and the imperfect MZM interference on mm-wave generation has been theoretically studied. Moreover, optimum conditions for the mm-wave generation using DSBCS modulation have been also discussed. The contributions and results include:

- 1) The modulation of the imperfect MZM can be modeled as the sum of a perfect MZM modulation and a phase modulation. As the MZM ER decreases, the phase modulation plays a more and more important role in the imperfect MZM modulation.
- 2) The OSNDR of mm-wave signals using DSBCS modulation increases first and then decreases as the MI for the MZM with ER of $>15\text{dB}$ decreases from 1 to 0.1. The maximum OSNDR originates the reduction the MZM nonlinearity and the OCSR which can improve and degrade the OSNDR, respectively.
- 3) The MZM ER can affect the maximum OSNDR. As the MZM ER ranges from 35dB to 15dB , the optimal MI for the maximum OSNDR will increase. When MZM ER is less than 15dB , the OCSR dominates the OSNDR. Hence, as the MI for the MZM with ER of $<15\text{dB}$ decreases from 1 to 0.1, the OSNDR will decrease.
- 4) The optimal MI for imperfect MZMs with ER of $>20\text{dB}$ is less than 0.7. Therefore, only SD-MZM is needed to realize DSBCS modulation, which is more compact and cost-effective. Moreover, the performance of the mm-wave signals can be improved.

5.1.2 Dual-Service Optical-Wireless Access Network

The optical-wireless access network offering wireless and wired-line signals has been proposed. We have experimentally demonstrated a novel and simple

method to simultaneously generate and transmit the BB and RF signals using only one MZM based on DSBCS modulation. The contributions and results include:

- 1) To investigate the impact of the MZM nonlinearity, the relation between MI-RF for DD-MZM and the performance of the generated signal is studied. As MI decreases, the duty cycle of optical microwaves and the OCSR decrease, resulting in improvement and impairment of the receiver sensitivity, respectively.
- 2) With optimal MI-RF equal to 0.43, the receiver sensitivity of the DC signal can have 1 dB improvement. Based on this result, only one SD-MZM is needed to generate optical microwaves using the DSBCS scheme, thus eliminating the requirement of a high cost DD-MZM without degrading the signal performance.
- 3) Following 75 km SSMF transmission, the power penalties of both BB and DC signals using only one SD-MZM are less than 0.3 dB.
- 4) We also confirm that BB signals have better robustness to the impairment of fiber nonlinearity than RF signals.

5.1.3 Hybrid Access Network Integrating RoF and FTTH Systems

Hybrid optical access networks, integrating FTTH and RoF systems sharing a single distributed infrastructure, are proposed for future multi-service access networks. We have demonstrated a novel method to enable RoF and FTTH systems to simultaneously generate and transmit both RF and BB signals on a single wavelength over a single fiber by using an integrated modulator. The BB and RF signals are modulated and transmitted at the optical carrier and subcarrier, respectively. The contributions and results include:

- 1) Since the BB and RF signals are generated at different sub-MZ, these two signals can be optimized individually. For RF signals using DSBCS modulation, the optimal MI-RF is 0.48, and it originates from the trade-off between the MZM nonlinearity and the OCSR for the RF receiver sensitivity when MI-RF is decreased.
- 2) For RF signals using DSB modulation, as MI-RF decreases, not only MZM nonlinearity decreases but also the OMI of the RF signals decreases. However, the OMI dominates the RF performance. Therefore, as MI-RF decreases, the RF sensitivity degrades. The optimal MI-RF for RF signals using DSB modulation is 1.
- 3) We also demonstrate a novel way to control the optical power ratios of the RF and BB signals to the hybrid signals by decreasing MI-BB and controlling the MZM biasing point for BB signals. With RF signals using DSBCS modulation, our proposed system can meet different RF and BB signal performance requirements without fading RF and BB signals.
- 4) The generated hybrid signals using DSBCS modulation for RF signals do not suffer from periodic performance fading problem caused by fiber dispersion. The receiver sensitivity penalties of both RF and BB signals are less than 0.2dB after transmission over 50km SSMF. The results reveal that the proposed system has great potential for use in future multi-service access networks.

5.1.4 Optoelectronics Package Using Powder Metallurgy for Triple-Directional FTTH Systems

We have successfully presented a cost-effective method of fabricating metal parts by using MIM steel. MIM method not only reduces number of

metal parts in laser module but also greatly reduces the cost. In addition, the advantage of applicability to several materials from MIM method can introduce SS316L, Kovar, and Invar material, which have characteristic of better property but difficult machining, into optoelectronic packages used in low-cost lightwave communication systems. Moreover, employment of MIM method can give optoelectronic module designer more design flexibility due to the advantage of shape complexity and make low-cost triple-directional optoelectronic module realizable. The following conclusions can be drawn from this study.

- 1) For the welding joint of DCP steel with high content of continuous porosity, serious gas expansion give rise to metal injection, resulting in weak and unstable joints.
- 2) The laser power is one of the most important parameters to control the defect formation of MIM steel during laser welding. The defect-free welding joints of MIM steel can be attained by using laser power of less than 1.0kW.
- 3) By optimizing welding parameters, the lap-fillet joint with a laser power and a pulse duration of 0.8ms and 3ms, respectively, is selected. The strength of the defect-free joint with MIM steel is larger than 15kg.
- 4) Although elimination of inherent porosity in MIM steel under optimum welding condition can give rise to additional PWS, PWS is still controlled to less than $2\mu\text{m}$, resulting in optical coupling loss of less than 15%.
- 5) Using MIM Invar with low CTE as construction material of asymmetric optoelectronic packages can minimize the tracking error which is an important issue for bidirectional and triple-directional optoelectronic packages.

- 6) The reliability test data demonstrate that the laser modules with using MIM steel as construction housing and without any defects in the welding joints are stable and reliable.

